MAKING CLOUDS LESS CLOUDY: MODELLING ISM WITH SIMULATIONS AND SYNTHETIC OBSERVATIONS

Zipeng Hu

A thesis submitted for the degree of

Doctor of Philosophy

The Australian National University

Research School of Astronomy & Astrophysics

June 2024

Dedicated to the 6-year-old me,
who spent the whole afternoon reading about galaxies,
and all my beloved ones,
for the company through this journey.

Disclaimer

I hereby declare that the work undertaken in this thesis has been conducted by me alone, except where indicated in the text. I conducted this work between July 2021 and June 2024, during which period I was a PhD student at the Australian National University. This thesis, in whole or any part of it, has not been submitted to this or any other university for a degree.

This thesis has been compiled as a Thesis by Compilation in accordance with relevant ANU policies. The first two main chapters in this thesis has been published in peer-reviewed journals, and the third chapter is a paper draft in preparation for submission. I have made significant contributions to each of these journal articles and have written the text of the papers myself, except where indicated otherwise.

Zipeng Hu

Zipeng Hu

15 October 2024

Acknowledgements

This thesis can not be finished with the efforts of only myself. Numerous people have provided their kind help and support during the last three years. Following here are my official thanks to a few of them.

First, I want to thank my primary supervisor, Prof. Mark Krumholz. Whenever I am stranded in data analysis, he can always think of unique statistical tools to extract useful information from my messy simulations. His patience and humor make our collaboration easy and enjoyable. I also want to extend my gratitude to my other two supervisors, Prof. Christoph Federrath and Prof. Naomi McClure-Griffiths. Their advice has been crucial for my study, especially when I was confused by all the strange filters and masks used in observations.

I am also very grateful to Dr. Benjamin Wibking, Dr. Hiep Nguyen, Prof. Robert Gutermuth, and Prof. Huabai Li, who have give me much advice and support in my PhD study and academic career development.

Last but not least, I would like to thank all my family members. Choosing astronomy as a career is never easy, but your love and consideration give me strength. Also thanks to my partner, for making everything in my life much more meaningful, including this thesis.

Abstract

Giant molecular clouds (GMCs) are the birthplaces of stars. Multiple physics mechanisms including gravity, magnetic fields, and radiation interplay within these clouds, and set the initial conditions for star formation. However, the exact role of each mechanism is still unclear, largely due to observational biases arising from projection, chemical, and excitation effects. Simulations and synthetic observations are therefore necessary for realistic interpretation of observations of the GMC formation and evolution processes.

This thesis focuses on building a comprehensive picture of the structure of GMCs using this approach. The first part of the thesis applies a theoretical model that can predict the 3D density structure of GMCs to determine the SFEs of nearby GMCs. The second part of the thesis examines measurements of magnetic field strengths, and points out that due to chemical and excitation biases the role of magnetic fields in GMC formation is less important than suggested by earlier interpretations of observations. The third part of this thesis reveals a significant discrepancy between two main star formation rate measurement methods, young stellar object counting and hydrogen recombination line observation, demonstrates how this discrepancy changes with local GMC conditions, and provides a calibration model for massive GMCs. I conclude this thesis by suggesting avenues for future studies.

Contents

List of Figures

List of Tables

Chapter 1

Introduction

Giant molecular clouds (GMCs) are the host sites of star formation and later stellar feedback. The physical properties of GMCs, like mass, column density, chemical composition, and temperature, are directly regulated by the large-scale galactic environment. Such properties then form the local conditions for star formation within clouds, and set the interstellar medium (ISM) structure in which stellar feedback happens. In return, the stellar feedback injects mass, metals, energy, and momentum into the ISM via photonionization, stellar winds, and supernovae (SNe), thus significantly affect the evolution of the ISM and the larger host galaxy. Therefore, GMCs lie in the center stage of the mass cycle between gas and stars, and play an important role in galaxy evolution. Precise measurements of cloud properties are crucial to understanding the physical mechanisms in this process.

However, such measurements are hard to achieve due to systematic errors from various sources, including resolution limits, projection effects, and non-uniformity in cloud chemical compositions and excitation conditions. To calibrate such errors and realistically model the GMC life cycle, we can perform simulations of GMCs and the star formation within, then produce synthetic observations to reproduce the phenomena in real observations. Such simulations should provide both high resolution and realistic galactic environments, while the synthetic observations should carefully consider the effects of radiative transfer, local chemistry, and excitation. This study achieves these goals, and provides a detailed and composite picture of GMCs.

In this chapter, we first discuss the general properties of ISM in Section 1.1, then provide a summary of the formation of GMCs and clumps in Section 1.2. The star formation process and the effect of stellar feedback is briefly described in Section 1.3. We further introduce the popular techniques of GMC simulation and synthetic observation in Section 1.4, and conclude with the motivations and innovations of this study in Section 1.5.

1.1 Overview of the ISM

The space between stars in a galaxy is filled with a dilute mixture of charged particles, atoms, molecules and dust grains, which is called the interstellar medium, or for short the ISM. By mass, the gas of the ISM consists of about 70% hydrogen (H), 28% helium (He), and 2% heavier elements commonly defined as metals in astrophysics. Percentages of H and He are inherited from the cosmic dawn, while the ratio of metals is related to stars. For our Milky Way, the total gas mass is estimated to be around 10^{10} $M_\odot$ (Kalberla & Kerp 2009). Interstellar dust consists of small, solid particles composed of silicates, carbon compounds, ice, and other materials. Although only making up about 1% of the mass of the ISM, dust plays a key role in absorbing and scattering light, influencing the thermal balance of the ISM, and catalyzing chemical reactions on its surface. Besides the materials, there also exists an interstellar radiation field (ISRF) in the ISM. Its interaction with gas and dust regulates the chemical and thermal states of the ISM: first, the gas chemical states depends on the molecule photon-dissociation rate and atom photo-ionization rate; second, the gas temperature is determined in large part by the photo-ionization effect and photon-electric heating effect.

The ISM gas has several distinct phases characterized by different chemical and thermal states. Here we provide a summary of these phases, in order of decreasing temperature T and increasing hydrogen nuclei number density $n_{\rm H}$, and tabulate their typical physical parameters in Table 1.1. We refer the reader to Draine (2011) and Klessen & Glover (2014) for further details.

Hot ionized medium. McKee & Ostriker (1977) point out that the blast waves from supernovae can create large, ionized bubbles filled with very hot gas, whose temperature reaches $T \gtrsim 10^{5.5}$ K, with a low density of $n_{\rm H} \approx 4 \times 10^{-3}$ cm^{-3}. Gas in this phase fills about 50% of the total volume of the galaxy, and cools on a timescale of about Myr through X-ray emission and adiabatic expansion.

Warm ionized medium. Gas in this phase is ionized by ultraviolet (UV) photons from young massive stars. It normally has $T \approx 10^4$ K and large density range $n_{\rm H} \approx 0.3 - 10^4$ cm^{-3}. Such gas accounts for only $\approx$ 10% of the total volume, and cools through line emission. It can be observed at optical wavelengths (such as Balmer lines). This gas phase is particularly associated with the H II regions created by recent star formation and planetary nebulae.

Warm neutral medium. Gas in this phase is heated by photo-electrons from dust grains. The typical temperature is about $T \approx 5 \times 10^3$ K, while the typical density is $n_{\rm H} \approx 0.6$ cm^{-3}. It occupies $\approx$ 40% of the total volume, and can be observed by

Gas phase	Temperature (K)	Density (cm^{-3})	Volume ratio (%)
Hot ionized medium	$\sim 10^6$	$\sim 10^{-3}$	50
Warm ionized medium	$\sim 10^4$	$0.3 - 10^4$	10
Warm neutral medium	≈ 5000	≈ 0.6	40
Cold neutral medium	≈ 100	≈ 30	1
Diffuse molecular gas	≈ 50	≈ 30	0.1
Dense molecular gas	10-50	$10^3 - 10^6$	0.01

Table 1.1: Physical parameters typical of different phases of ISM. Adapted from Klessen & Glover (2014).

the H I 21 cm line due to its neutral chemical state.

Cold neutral medium. Such gas is also heated by photo-electrons, but then cooled through fine structure line emission. Its temperature is about $T \approx 100$ K, and it density is about $n_{\mathrm{H}} \approx 30\ \mathrm{cm}^{-3}$, accounting for $\approx 1\%$ of the total volume. As described in the model by Field et al. (1969), both warm neutral medium and cold neutral medium can exist at the same pressure, while the inter-conversion between the two phases depends on the change of gas density.

Diffuse molecular gas. Such gas has similar physical properties as the cold neutral medium: $T \approx 50$ K, $n_{\mathrm{H}} \approx 100\ \mathrm{cm}^{-3}$, and accounting for $\approx 0.1\%$ of the total volume. However, now with sufficient density to shield the central part of the atomic hydrogen cloud from photodissociation (referred to as self-shielding), hydrogen molecules form within. Therefore, gas in this phase is often mixed with the cold neutral medium. CO molecules can also exist under this density, making it possible to trace this gas phase with associated emission.

Dense molecular gas. In gravitationally bound molecular clouds, the gas density increases to $n_{\mathrm{H}} \approx 10^3 - 10^6\ \mathrm{cm}^{-3}$ due to cloud collapse, and the temperature can drop to as low as 10 K. We can still trace such gas with CO emission, but we can also observe it with the far-infrared (IR) emission from dust. Due to its high density, this gas is also the site of star formation.

Besides the thermal and chemical state, the evolution of the ISM is also affected by many other physical mechanisms, among which the significant ones are gravity, turbulence, and magnetic fields. Gravity drives gas accumulation, molecular cloud formation and the star formation within. As summarized in the review by Elmegreen & Scalo (2004), the ISM has long been observed to be turbulent from the Doppler broadening of spectral lines. This turbulence exists over a wide range of sizes, from sub-parsec scales within molecular clouds to kilo-parsec scales encompassing galactic discs. The corresponding velocity dispersion has a typical value between 1-10 km/s depending on the spatial scale. The energy sustaining such motion is provided by stellar feedback and differential galactic rotation. Turbulence plays various roles in the evolution of ISM. First, it can compress gas to high densities, triggering star formation, while at the same time providing kinematic support against gravity and suppressing the star formation rate. Second, turbulence contributes to the hierarchical structure of the ISM, creating a complex network of filaments, clumps, and voids. Moreover, it can dissipate energy because of gas viscosity and change the gas thermal state, mix the metals produced via stellar feedback, and amplify the interstellar magnetic field through dynamo processes.

Magnetic fields (B-fields) also play an important role in the physics on the ISM. Current theories propose that the interstellar B-field arises from galactic-scale dynamo amplification of seed fields generated by Biermann batteries in early AGNs and/or Population III stars (Kulsrud & Zweibel 2008). Observing these fields presents challenges, but astronomers employ methods such as polarimetry, the Zeeman effect, and Faraday rotation to map their orientation and strength (see the recent review by Pattle et al. (2023)). As summarized in Crutcher (2012), the typical galactic magnetic field strength in the Milky way ISM is $\sim 10\,\mu$G, and can increase to $\sim$ mG in dense regions. Influenced by turbulence and galactic dynamics, ISM B-fields exhibit a complex, tangled structure, which in return shapes the dynamics of ISM: magnetic pressure provides support against gravitational collapse, thus regulating star formation rates (e.g. Federrath & Banerjee 2015; Girichidis et al. 2018); the B-field orientation channels gas flows, contributing to the formation of filamentary gas structures (e.g. Soler et al. 2013; Ade et al. 2016). Moreover, magnetic fields affect the propagation of charged particles like cosmic rays, thus influencing the ISM thermal and chemical state. We here show an example of magnetic field morphology in part of the Orion Molecular Cloud (OMC) in Figure 1.1. The alignment between the B-field and gas structure changes from being parallel in low-density regions to perpendicular in dense regions, indicating different roles of B-field in gas dynamics.

1.2 GMCs and clumps

While the existence of molecules in the ISM was first confirmed by optical observations of the diffuse interstellar bands (Swings & Rosenfeld 1937; McKellar 1940), the study of GMCs began with the detection of interstellar CO $J = 1 \rightarrow 0$ radio emission line by Wilson et al. (1970). Follow-up Galactic Plane surveys using the CO line (e.g. Dame et al. 2001) found many cloud-like dense molecular gas structures, while recent observations powered by modern millimeter interferometer

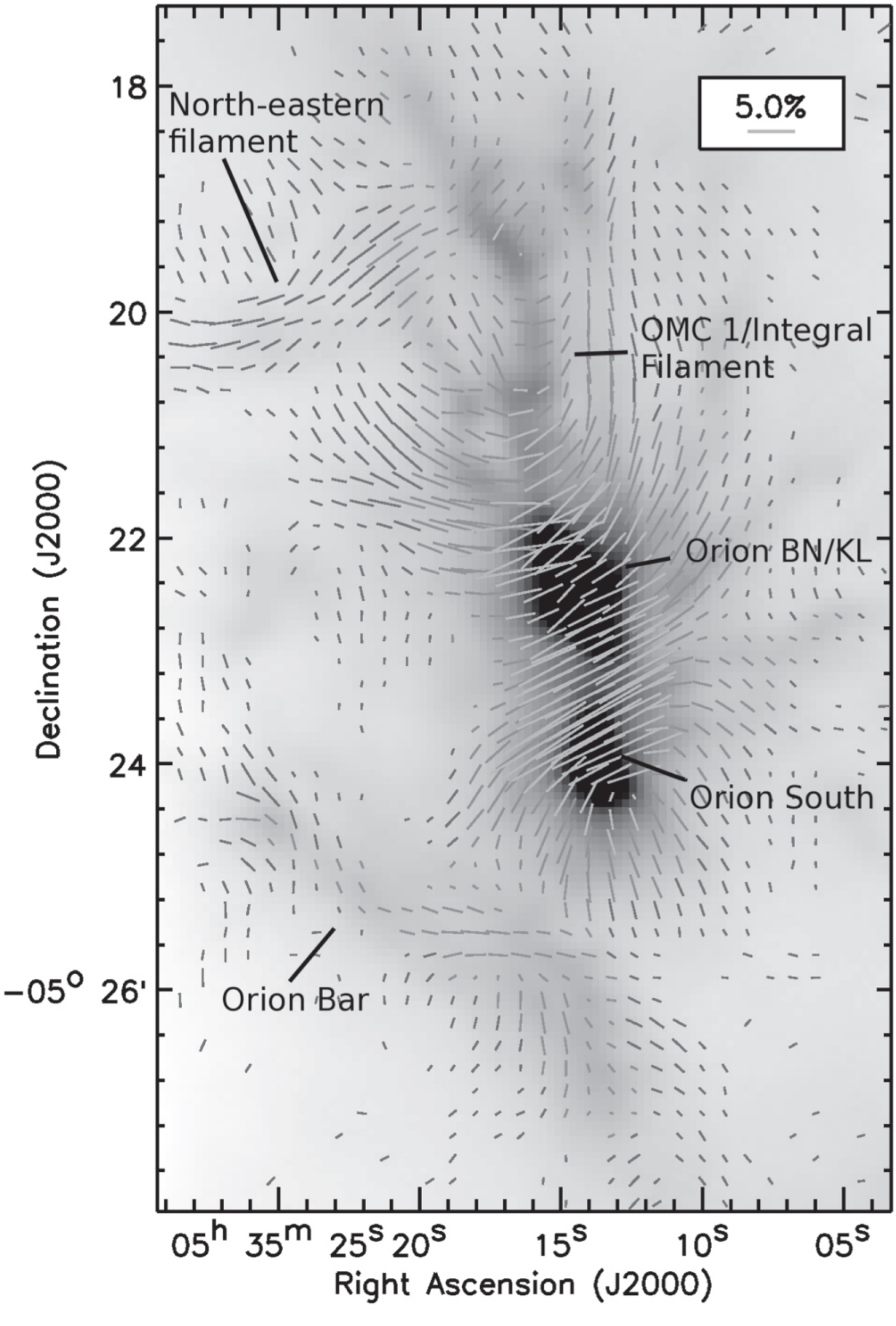

Figure 1.1: Polarization map of the OMC 1 region of the "integral filament" in Orion A. The gray vectors show the B-field direction. While the background image is a SCUBA-2 850 μm emission map, representing gaseous mass structure. Image credit: Ward-Thompson et al. (2017).

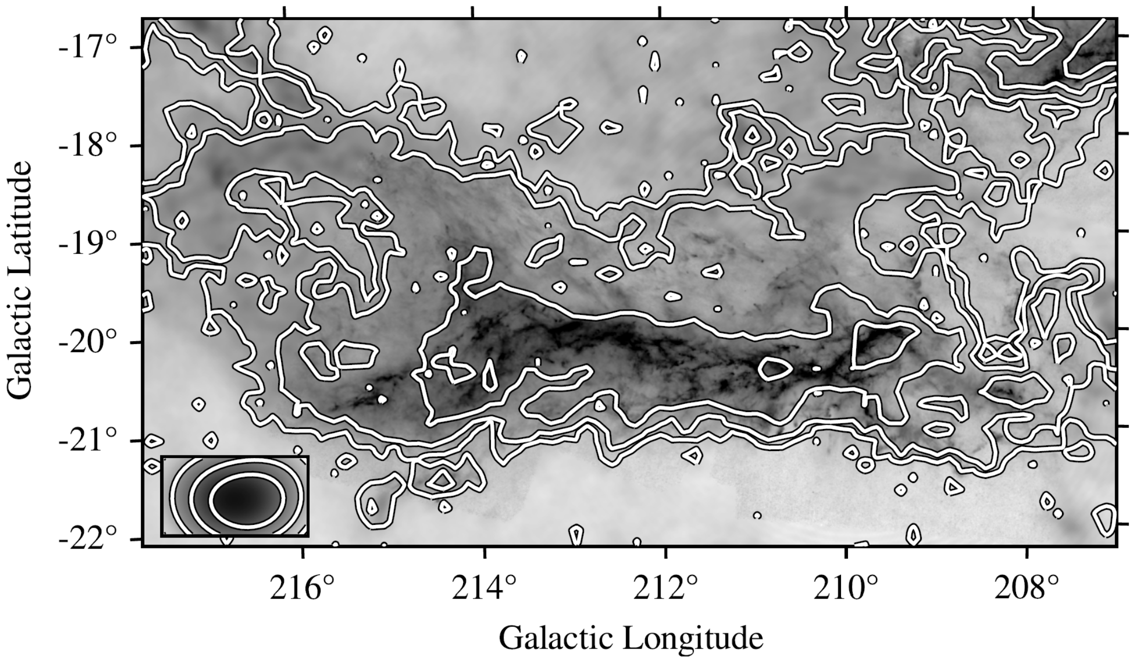

Figure 1.2: Observations of the Orion A GMC. The dust emission map is plotted as the gray background (Lombardi et al. 2014), while the ^{12}CO $J = 1 \rightarrow 0$ emission is shown as the white contours (Wilson et al. 2005), both on log scales. The inner figure at the lower left corner shows the same maps convolved to 50 parsec resolution, mimicking the typical observations of GMCs in nearby galaxies. Image credit: Chevance et al. (2023).

arrays can detect molecular gas from nearby galaxies to high-redshift galaxies at $z \sim 2$ (Tacconi et al. 2020). Besides the CO emission line, we can also trace the cold dense gas with dust emission and extinction, while extinction observations are limited to the Solar neighborhood due to the lack of background sources and line of sight blending. In Figure 1.2 we show both CO and dust emission observations of Orion A (Wilson et al. 2005; Lombardi et al. 2014), a GMC at a distance of $\sim$ 460 pc, with a mass $M \sim 8 \times 10^4$ M$_\odot$. Both tracers here show a filamentary structure throughout the cloud. However, the CO emission tracing molecular mass has clear boundaries due to sensitivity limits, while the dust emission tracing the total column density shows that the GMC is part of a large structure, which combines both atomic and molecular gas. Such differences illustrate the challenges in defining GMCs. In the synthetic observations in Chapter 4, I define GMCs as enclosed CO emission contours above certain thresholds, which is aimed for direct comparisons with extragalactic observations using the same tracer.

Observed GMCs generally have masses of $\sim 10^4 - 10^6$ M$_\odot$, sizes $\sim$ 100 pc, mean hydrogen molecule number densities $n_{\mathrm{H}_2} \sim 100$ cm^{-3}, and gas temperatures $T \sim 10$ K (Solomon et al. 1987; Scoville et al. 1987; Dame et al. 1987, 2001). These GMC properties are not independent of each other. From observations of nearby GMCs, Larson (1981) first finds that the GMC velocity dispersion is proportional to the cloud size. The review by Heyer et al. (2016) summarizes the relation between the cloud mass M, mean radius R and velocity dispersion along the line of sight σ_v as

$$\sigma_v = \sigma_0 \left(\frac{R}{1\ \mathrm{pc}}\right)^a \text{ and } M = \Sigma_{\mathrm{mol}} \pi R^b, \tag{1.1}$$

where $a \approx 0.5$ and $b \approx 2$. σ_0 is the line width measured on 1 pc scale, and Σ_{mol} is the average molecular mass surface density. For Milky Way, $\sigma_0 \approx 0.7$ km/s, and $\Sigma_{\mathrm{mol}} \approx 100\ \mathrm{M_\odot pc^{-2}}$ (Solomon et al. 1987; Heyer et al. 2009). However, both values vary across galaxies due to the differing galactic environments of GMCs. Chevance et al. (2023) make an empirical conclusion that Σ_{mol} increases with kpc-scale gas surface density, and σ_0^2 is proportional to Σ_{mol} due to the balance between turbulent and gravitational energy. As for magnetic field strengths, Zeeman effect measurements on nearby GMCs find a general relation that

$$B = \begin{cases} B_0 & \text{if } n_{\mathrm{H}} < n_0 \\ B0 \left(n_{\mathrm{H}}/n_0\right)^{\kappa} & \text{if } n_{\mathrm{H}} \geq n_0 \end{cases}, \tag{1.2}$$

where $B_0 \approx 10\mu$G, $n_0 \approx 300\ \mathrm{cm^{-3}}$, and $\kappa \approx 0.65$ (Crutcher 2012).

GMCs form out of relatively diffuse ISM, which requires accretion of gas to create such over-densities. Note that the accretion of new gas can happen throughout the lifetime of GMC. As discussed in Dobbs et al. (2014), mechanisms on various scales can contribute to the gas concentration. With decreasing spatial scales of the energy sources, these mechanisms include: (a) compression in galaxy mergers, (b) compression from galactic shear motion, spiral density waves, and bars, (c) cloud-cloud collisions, (d) compression from shock waves at the boundary of SNe driven shells and bubbles, (e) gas flows converging driven by turbulence, and (f) collapse of gravitationally unstable regions. These mechanism can interplay with each other. For example, the supernovae shock powers the turbulence in the ISM that can drive gas flow, and cloud-scale gravitational instability is often created by mechanisms on larger scales like galactic shear and cloud-cloud collisions. When the gas density is high enough, the local region becomes optically thick to photo-dissociating radiation via a combination of molecular self-shielding and dust attenuation of the far-ultraviolet (FUV) photons. Dust grains also provides formation sites of H_2 via physisorption and chemisorption. For a dust-to-gas ratio Z'_d (for standard Galactic conditions, $Z'_d = 1$), the H_2 formation time is about

$$t_{\mathrm{H}_2} \approx \frac{1000}{Z'_d n_{\mathrm{H}}}\ \mathrm{Myr}. \tag{1.3}$$

For a typical GMC with $n_{\mathrm{H}} = 100\,\mathrm{cm}^{-3}$, $R = 3$ pc, and $\sigma_0 = 0.7$ km/s, this time scale (~ 10 Myr)is comparable to the free-fall time (~ 5 Myr, defined later in equation 1.7) and turbulent eddy turnover time ($t_{\mathrm{eddy}} \sim 2R/\sigma_0 \sim 9$ Myr), indicating that GMC dynamics and chemistry are coupled. Note that CO molecule formation generally requires a higher shielding column density than H_2, so there can exist a substantial part of H_2 mass in the "CO dark" region (Sternberg & Dalgarno 1995; Hu et al. 2021b).

After the formation of a GMC, its evolution is mainly controlled by the star formation within. Star formation does not occur everywhere in the GMC because of the non-uniform internal cloud structure. Driven by supersonic turbulence and self-gravity, clumps of higher density form within GMCs, and whether these can collapse further depend on their physical conditions. A minimum requirement for collapse is that gravity be able to overcome thermal pressure (Jeans 1902). For a gas clump with uniform density ρ, temperature T, and mean molecular weight μ, the mass limit for collapse (normally called the Jeans mass) is:

$$M_{\mathrm{J}} = \left(\frac{4\pi\rho}{3}\right)^{-1/2} \left(\frac{5RT}{2\mu G}\right)^{3/2}, \tag{1.4}$$

where R is the ideal gas constant, and G is the gravitational constant. Beside internal gas pressure, the shearing force can also provide support against gravity. For an approximately spherical gaseous region within a rotating disc, its stability can be characterized by the Toomre parameter Q (Toomre 1964):

$$Q = \frac{\kappa c_{\mathrm{s}}}{\pi G \Sigma_{\mathrm{gas}}}, \tag{1.5}$$

where κ is the epicyclic frequency, c_{s} is the sound speed, and Σ_{gas} is the gas surface density. Gaseous regions are stable against gravity if Q is larger than 1. However, the real case can be complicated, since the gaseous and stellar components of one galaxy are gravitationally coupled. Jog & Solomon (1984) find that when both components are stable, gravitational instability may still occur and grow due to the interaction of the two components.

The magnetic field can also stop gravitational collapse, but it only provides support in the direction perpendicular to the field lines. Thus gas collapse along the field lines

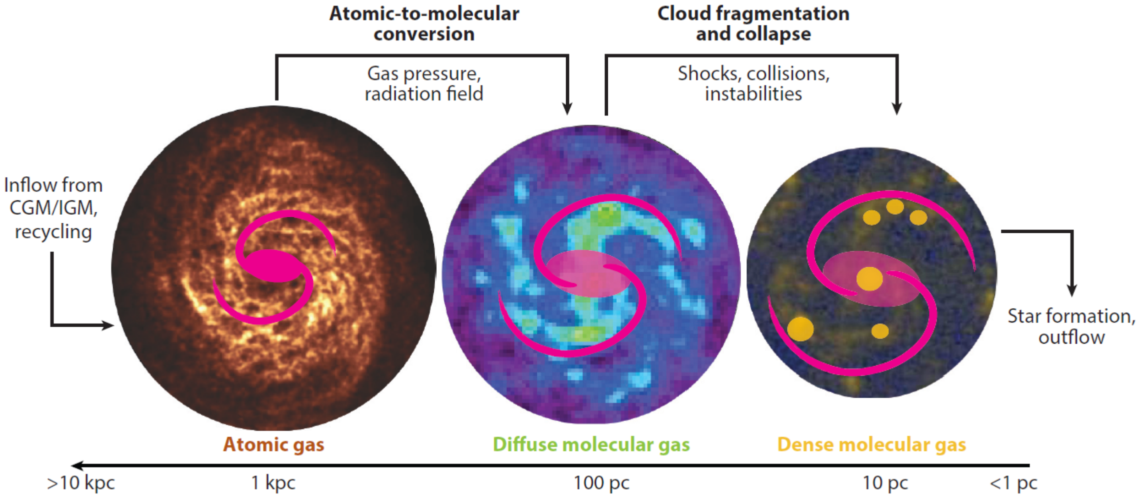

Figure 1.3: Schematic illustration of the connections between atomic ISM, GMC and clumps. The physical mechanisms behind gas phase conversion on different scales are highlighted. Image credit: Saintonge & Catinella (2022).

is still possible. Analogous to M_J, the magnetic critical mass M_ϕ is (Mouschovias & Spitzer 1976):

$$M_\phi = \frac{0.53\phi}{3\pi}\sqrt{\frac{5}{G}}, \tag{1.6}$$

where ϕ is the magnetic field flux. A gas cloud with mass $M \geq M_\phi$ is referred to as super-critical, while one with $M < M_\phi$ is sub-critical. The role of magnetic field in clump/protostar mass aggregation is still unclear. Hull et al. (2017) compare the B-field properties from ALMA observations and MHD simulations, and argue that the morphology of magnetic field is unlikely to be preserved across different spatial scales. Such result indicates limited influence of B-field in material channeling from GMCs to dense cores, then protostellar disks. Finally, even clumps that are measured to be stable under these criteria can still be driven to collapse by external shock waves or cloud-cloud collisions. We illustrate the path of gas from the galactic environment all the way to star-forming clumps in Figure 1.3, where we can see that the GMCs are at the crossroads of various physical scales and mechanisms.

1.3 Star formation and stellar feedback

When gravity becomes the dominant force in dense clumps, gas starts to convert into stars. The natural reference time scale for such a system is the free-fall time,

$$t_\mathrm{ff} = \sqrt{\frac{3\pi}{32G\rho}}, \tag{1.7}$$

where ρ is the gas density. The free-fall time represents the lower limit of the GMC collapse time if only gravity is considered. However, GMCs are observed to convert their gas into stars at a rate much smaller than would be expected from free-fall collapse. To quantify the efficiency of star formation in a given region, Krumholz & McKee (2005) define the star formation efficiency per free-fall time (SFE) as:

$$\epsilon_{\rm ff} = \frac{\dot{M}_*}{M_{\rm gas}/t_{\rm ff}}, \tag{1.8}$$

where $\dot{M}_*$ is the star formation rate (SFR), and $M_{\rm gas}$ is the total gas mass. $\epsilon_{\rm ff}$ is measured to be very low in various kinds of observations. Krumholz et al. (2019) compile measurements of $\epsilon_{\rm ff}$ from different methods, and conclude that $\epsilon_{\rm ff} \approx 0.01$ for regions above parsec scale, with a dispersion of $\lesssim 0.5$ dex. We describe in Section 1.4 the measurement methods for the physical properties used in equation 1.8.

Several theoretical models have been developed to explain the low $\epsilon_{\rm ff}$. The earliest ones assume that if the interstellar magnetic field is strong enough, gas collapse will be stopped until non-ideal magnetohydrodynamic (MHD) processes become significant in high density regions and reduce the magnetic flux. However, Zeeman effect B-field strength measurements suggest that GMCs are generally super-critical, and therefore that magnetic support against gravity is limited. Some other models focus on the turbulence in the cloud. As shown in equation 1.1, for a region with size R, the velocity dispersion $\sigma_v \propto R^{0.5}$, thus the kinetic energy per unit mass $e_{\rm K} \propto R$. If the region has a uniform density ρ, it gravitational binding energy per unit mass scales with R as $e_{\rm G} \propto G\rho R^3/R \propto R^2$. Therefore, the virial ratio $\alpha_{\rm vir}$ for a random sub-region of a cloud is inversely proportional to R, indicating that the most local regions of GMCs are gravitationally unbound. This statement is supported by a number of works that models the probability density function (PDF) of the GMC density and the evolution of self-gravitating parts of a GMC (e.g. Krumholz & McKee 2005; Hennebelle & Chabrier 2011; Padoan et al. 2012; Federrath & Klessen 2012). But turbulence alone not fully explain the low $\epsilon_{\rm ff}$ in observations, since the density PDF of a collapsing cloud will increase its high-density end with time, causing $\epsilon_{\rm ff}$ to rise during GMC evolution (Murray & Chang 2015; Burkhart 2018). Recent works find that stellar feedback can disrupt such high density regions and finally disperse the GMC, therefore stopping the star formation process (e.g. Kim et al. 2018; Grudić et al. 2021; Chevance et al. 2020; Kim et al. 2022). We will further discuss different stellar feedback mechanisms and their effects at the end of this section.

Once stars are formed, their properties and evolution are largely determined by their masses. Observations have found that the relative number of stars that form during a single star-forming burst follow a mass distribution known as the initial mass function (IMF). The first attempt to measure the IMF was made by Salpeter (1955), who bound that is can be described as:

$$\frac{dN}{d\log M} \propto M^{-\alpha}, \tag{1.9}$$

where M is the stellar mass at birth, N is the number of stars, and $\alpha = 2.35$. Later observations confirmed that this power law extends over 2 magnitude of stellar mass, from about 1 $M_\odot$ to 100 $M_\odot$. However, for sub-solar-mass stars, the power law is no longer suitable. Chabrier (2003) modeled the lower end of IMF ($M < 1M_\odot$) as a log-normal distribution with a peak at $\sim 0.1 - 0.3 M_\odot$. Recent observations also suggest that the slope of IMF above 1 $M_\odot$ may vary from $\alpha = 2.35$ in different galaxies, depending on the local environment (see the review by Hennebelle & Grudić 2024). Therefore, most stars are born with a low mass, and these stars may contribute little to the integrated light output by an external galaxy due to the steep stellar mass-luminosity relationship. Knowledge of the IMF is therefore crucial to recovering the total stellar mass of galaxies where effectively only massive stars can be observed.

Throughout their evolution, stars inject momentum and energy into the ISM via various stellar feedback processes. The stellar feedback suppresses star formation, dissolves star clusters, and finally disperses the host cloud. Here we provide a brief summary of main stellar feedback mechanisms and their effects on the ISM. We refer the readers to Chevance et al. (2023) for a more detailed review.

Jets and outflows. This wind-like stellar feedback originates from circumstellar disks around protostars and disk-magnetosphere interfaces. Its energy source is the interaction between magnetic fields and the rotating accretion disk. Jet and outflows are important for the dispersal of the natal cores of individual stars, but are not strong enough to disperse entire GMCs (Li & Nakamura 2006; Matzner & Jumper 2015).

Photoionization. Hot and massive stars, such as O and B type stars can emit significant amounts of UV photons that can ionize hydrogen atoms, increasing the gas temperature to $T \approx 10^4$ K, and creating regions of ionized gas known as H II regions. Because the increase in temperature also leads to a large increase in pressure, H II regions expand at a speed of ~ 10 km/s after formation, pushing the nearby neutral ISM away. The size and shape of H II regions depend on the local ISM density and structure, and the flux of ionizing photons. Recent simulations find that photoionization can destroy GMCs by both photoevaporation and momentum injection, and finally suppresses the SFE (Kim et al. 2018; Grudić et al. 2021). Meanwhile, the H II bubble expansion are also observed to trigger star formation on the edge due to compression of the surrounding gas (e.g. Zavagno et al. 2020).

Radiation pressure. A zero-age population of stars that fully samples the IMF emits most of its light at UV wavelengths where the ISM is optically thick, so almost all radiation momentum is deposited in the gas. The resulting force is known as direct radiation pressure that can counter gravity and limit the SFE. After absorbing the radiation, dust re-emits the energy in the form of IR light. Dusty ISM is ~ 100 times less opaque to IR than to UV radiation. Therefore the reprocessed radiation can only inject momentum into gas in clouds with sufficiently high column density, which is called indirect radiation pressure. Semi-analytical models and simulations (Wibking et al. 2018; Crocker et al. 2018; Menon et al. 2022a,b) find that for most actively star-forming galaxies, the indirect radiation pressure has limited contribution to the turbulent energy in the ISM. If the cloud IR opacity is high enough, however, the cycle of absorption and re-emission can repeat for many times before the energy escapes, and the indirect radiation pressure may exceed the direct one (Thompson et al. 2015).

Stellar winds. These line-driven winds with a typical speed of $\sim 10^3$ km/s (Vink et al. 2001) originate from O type stars. The direct momentum flux of winds is comparable to that from radiation pressure and supernovae (Leitherer et al. 1999), and scales with metallicity as $\propto Z^{0.8}$ (Kudritzki & Puls 2000). The total momentum contributed by stellar winds can be much higher if the winds are trapped by dense surrounding gas. Under this circumstance, the winds increase the local temperature to $\gtrsim 10^7$ K, creating hot bubbles that can push the gas and potentially eject it out of GMCs. Recent theoretical modeling by Lancaster et al. (2021), however, find that this scenario are likely to be rare: in turbulent ISM, the bubble created by stellar wind has complicated morphology and large area of interface with surrounding denser gas, which strongly enhances energy losses from the hot interior of the bubble, thus less momentum injection. Multi-wavelength observations on H II regions in nearby galaxies (Lopez et al. 2011, 2014) find that the momentum injected from the shock-induced hot gas is on average one to two orders of magnitude larger than that from radiation pressure, but below photoionization pressure.

Supernovae. These violent explosions come either from white dwarfs that accrete or merge beyond the Chandrasekhar mass limit 1.44 $M_\odot$ (type I SNe), or from the death of massive stars $> 8\,M_\odot$ via core collapse (type II SNe). SNe have a significant influence on the structure of both the ISM and galaxies (Hopkins et al.

2018b). However, their effects on individual GMCs are not as important despite the considerable momentum and energy injection. Type I SNe start to occur at ~ 100 Myr after star formation, which far exceeds a typical GMC lifetime. As for type II SNe, they occur at $\approx 3 - 40$ Myr after the birth of stars depending the stellar mass, and during such delay GMCs may have already been dispersed by other stellar feedback mechanisms (Fall et al. 2010; Chevance et al. 2022).

Depending on the cloud mass, GMCs normally have a lifetime of $\sim 10 - 30$ Myr before being destroyed by stellar feedback processes (Chevance et al. 2020). Of all the processes mentioned above, photoionization is likely the dominant one because of its high pressure and negligible time delay. We also note that a large part of the energy injected from stellar feedback can escape through low-density directions to large scales, or be radiated away. Thus the regulation of GMC evolution by feedback greatly depends on cloud properties like density structure and opacity. We schematically illustrate such complexity in Figure 1.4, where different colors present different gas phases: warm ionized gas in the H II regions near stars (red), warm neutral atomic gas around H II regions (blue) where hydrogen is photodissociated (PDR), and cold molecular gas (gray). This figure illustrates three mechanisms by which H II regions and GMCs can interact: (1) a H II region can totally destroy a host low-mass cloud; (2) H II bubble expansion can occur in a preferred direction, compressing the GMC into a dense filament and leaking ionizing photons into the ISM; (3) H II regions can be totally bounded by their dense host clouds. Any given GMC may experience more than one of these scenarios during its lifetime.

1.4 Simulation and synthetic observation

Because of the complex interplay of the physics mechanisms introduced above, simulations are crucial for the theoretical modeling of GMC evolution and star formation. There are three unique advantages of simulations: first, we can trace the simulated cloud throughout its lifetime, while in observations we only have a snapshot of the current universe; second, we can directly obtain the cloud physical properties from the simulation output, while in observations many measurements are made with indirect tracers; third we can evaluate the relative importance of each physical mechanism by turning it on or off in different simulations, which is impossible in a real galaxy. We tabulate the main physical processes included in GMC simulations and corresponding numerical methods in Table 1.2.

For this thesis we use the simulation code GIZMO for our theoretical modeling. GIZMO is a state-of-the-art numerical simulation code designed for astrophysi-

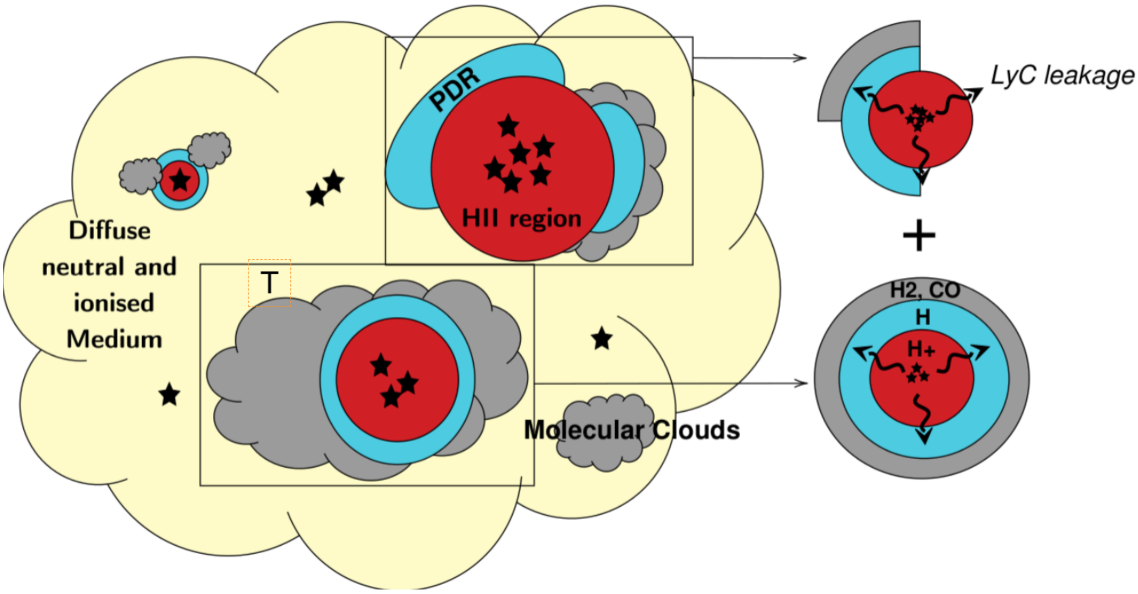

Figure 1.4: Schematic illustration of the H II region effects on the GMC. Different colors represent different gas phases as labeled, and the black stars are the newly formed stars. Image Credit: Ramambason et al. (2022).

cal hydrodynamics and N-body problems (Hopkins 2015; Hopkins & Raives 2016; Hopkins 2016). It offers unique advantages by employing the Lagrangian "meshless finite mass" (MFM) method or "meshless finite volume" (MFV) method. Compared with traditional smoothed particle hydrodynamics (SPH) and grid-based methods, GIZMO's MFM and MFV approaches allow for adaptive resolution that follows the flow of matter, capturing shocks, instabilities, and complex gas dynamics with high accuracy, as well as reducing numerical viscosity and kernel bias issues. These advantages make GIZMO particularly effective for simulating the diverse and dynamic environments of GMCs. Furthermore, its modular design allows for easy incorporation of additional physics, such as magnetohydrodynamics (MHD), radiative transfer, and stellar feedback processes, making it a versatile tool for a wide range of astrophysical applications.

Previous simulations of GMC evolution can be categorized into two types. The first type of simulation sets up the initial condition as individual clouds at ~ 100 pc or smaller scale. Such simulations normally solve the radiation transfer problem explicitly, and follow the interaction between stellar feedback and the ISM with high resolution. For example, Grudić et al. (2019) perform simulations of individual GMCs with various stellar feedback treatments, and find that the star formation is completed within $\sim 1t_{\rm ff}$ after the first gas collapse. Fukushima et al. (2020) study the relation between GMC life time and surface density with a set of ray-tracing RHD simulations, and find a increasing trend of cloud life time with higher $\Sigma_{\rm gas}$. Kim et al.

Physical mechanism	Numerical method
Gravity	Tree Algorithms Particle-Mesh Methods
Ideal MHD	Smooth Particle Hydrodynamics Adaptive-Mesh Refinement Moving-Mesh Methods Meshless Finite-Mass/Volume
Radiation Transfer	Ray Tracing Monte Carlo Method Two Moments Method Flux-Limited Diffusion Method
Star formation	Sink Particle/Cell
Stellar feedback	Sub-grid Models

Table 1.2: Numerical methods for realizations of different physical mechanisms. For details of each method, we refer the readers to the review by Teyssier & Commerçon (2019).

(2021) simulate GMCs of $10^5\,\mathrm{M}_\odot$ with detailed treatments of turbulence, radiation, magnetic fields and stellar feedback, and find that the GMCs are rapidly dispersed by UV radiation. However, such simulations generally assume an ideal initial condition for the GMC, and omit the effects of large scale dynamics like cloud-cloud collision and galactic shear. The second type of simulations trace the cloud lifetime within a simulated galaxy. The main benefits of this approach is its inclusion of a realistic galactic environment, which may be important for many aspects of GMC evolution. For example, Jeffreson et al. (2021a,b, 2024) study the lifetime of GMCs in a galactic simulation with a mass resolution of $10^3\,\mathrm{M}_\odot$. Their results show that photoionization effect quickly disperses low-mass clouds, while more massive clouds have extended lifetimes because the mass lost to photoionization is replenished by ongoing accretion. Bending et al. (2020) perform a zoom in simulation of part of a spiral arm, whose initial condition is extracted from a galactic simulation, and find that ionizing feedback is effective in breaking up massive clouds with large masses into less massive ones. However, Grisdale et al. (2019) present short GMC lifetime results ($\sim$ 3-4 Myr) in their simulations which have no ionizing radiation feedback, indicating that ionizing radiation may not be the only cause of short cloud lifetime. Nevertheless, the resolution in these studies is much lower than that typically used in single-cloud models, and their sub-grid models do not treat stellar feedback as accurately as in the higher-resolution isolated-cloud simulations. A promising avenue for future work is clearly to calibrate sub-grid models in high-resolution cloud simulations, then apply them in large-scale galactic ones.

Even once one has run a simulation, however, comparing it to observations is not

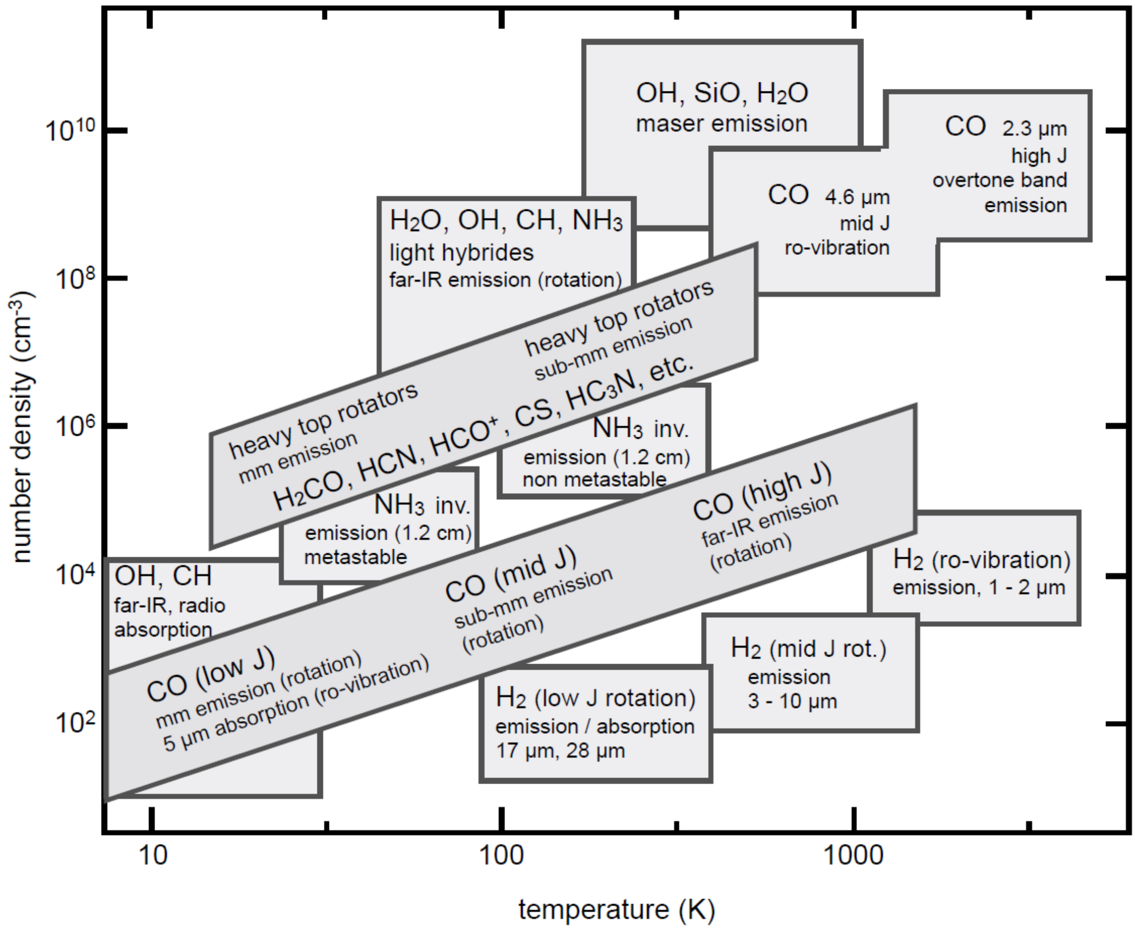

Figure 1.5: Commonly used emission tracers for GMC study. Gray bands mark the most suitable temperature and density ranges for different molecules. Image credit: Klessen & Glover (2016).

trivial. The reason is that the observational measurements of cloud properties are often indirect and rely on various assumptions, and thus may differ from the quantities directly extracted from simulation output. An ideal way to overcome this inconsistency is to produce synthetic radiation and derive physical quantities using techniques similar to observations. Figure 1.5 illustrates the density and temperature ranges where different emission tracers perform best. Here we provide a brief summary of several observational techniques that are crucial to our study, and the corresponding synthetic observation methods.

Mass and density. As introduced in Section 1.2, CO emission is commonly used to trace molecular gas. For a certain region with total CO emission luminosity $L_{\rm CO}$, its total molecular mass can be derived as $M_{\rm H_2} = \alpha_{\rm CO} L_{\rm CO}$, where $\alpha_{\rm CO}$ is the luminosity-to-mass conversion factor. This factor is not a constant, but instead varies at least somewhat as a function of physical conditions, and must therefore be calibrated with a combination of simulations and cross-checks against other methods – see the review by Bolatto et al. (2013) for more details. Due to projection effects, going from a measurement of mass to a measurement of cloud density ρ replies on further assumptions about the line-of-sight scale of the cloud, and the common practice is to idealize the cloud as a sphere with uniform density. When making synthetic measurements from simulation data, we need to first determine the CO molecule abundance and emissitivity throughout the cloud, either by on-fly calculation or post-analysis, then project the CO emission into a 2D map. From the resulted map we then identify GMCs as enclosed contours, derive their masses from the total CO luminosity, and their densities by treating them as spheres with mean radii the same as the projected shapes.

B-field strength. There are two main methods to measure magnetic field strength in neutral cold gas. The Davis-Chandrasekhar-Fermi (DCF) method (Davis & Greenstein 1951; Chandrasekhar & Fermi 1953) utilizes the linear polarization of continuum radiation emitted or absorbed by dust grains, which are aligned to magnetic fields by external radiation torques (Lazarian 2007). The dispersion of polarization angles tells us ratio between the turbulent energy and the magnetic energy. The reason is that a strong B-field and retain an ordered morphology against turbulence, which results in a small dispersion in the polarization angles. One can derive the plane-of-sky (POS) B-field strength with measurements of mean density, line-of-sight velocity dispersion, and polarization angle dispersion. Many works have used MHD simulations to calibrate the DCF method under different physical conditions, and we refer the readers to the review by Liu et al. (2022) for more details. The second method observes the Zeeman-effect-induced frequency differences between the left and right circularly polarized components of spectral lines, and larger differences indicates stronger line-of-sight (LOS) B-field. The Zeeman effect observation is the only available method that can directly measure the B-field strengths in the ISM (Crutcher et al. 1993). As summarized by Crutcher (2012), commonly used spectral lines include H I 21 cm line, OH, and CN, each tracing a different density range. To mimic the first method, we need to either assume or model a background radiation field, calculate the degree of grain alignment as a function of radiation field and local gas conditions, then integrate the polarization angle along the LOS using the simulated B-field structure to produce a synthetic polarization map. When mimicking Zeeman effect measurements, we need to derive the local emissivity or absorption coefficient of the spectral line of interest, solve the equation of radiative transfer along a line of sight, and derive the Stokes parameters from the resulting spectrum.

SFR. There are many ways to estimate star formation rates – see Kennicutt &

Evans (2012) for a detailed review – so here we will focus only on two that will be relevant for this thesis: young stellar object (YSO) counting and Hα emission. Stars with ages $\lesssim 2$ Myr are embedded in dusty circumstellar disks, leading to excess IR emission that can be identified from high resolution IR observations. With currently favored IMFs (Chabrier 2003, e.g.), the mean mass of these stars $\langle M_* \rangle = 0.5\,\mathrm{M}_\odot$, while a recent survey of star formation products in the solar neighborhood finds a slightly smaller mean mass $\sim 0.41\,\mathrm{M}_\odot$ (Kirkpatrick et al. 2024). The duration of an IR excess t_{excess} is estimated to be ~ 0.5 Myr for Class 0/I phases combined, or $\sim$ 2 Myr if the Class II phase is also considered (Evans et al. 2009). Later analysis of YSOs in Perseus and Taurus narrows the duration of Class I phase to ~ 0.38 Myr (Carney et al. 2016). By counting the number of YSOs within, one can measure the SFR of a certain region as:

$$\dot{M}_* = N(\mathrm{YSOs})\langle M_* \rangle / t_{\mathrm{excess}}. \tag{1.10}$$

This equation assumes constant SFR and negligible YSO displacement during the duration of t_{excess}. It also needs correction for incompleteness if the low mass YSOs can not be resolved, for example, in the observations of GMCs in the Magellanic Clouds (Indebetouw et al. 2008; Chen et al. 2009, 2010). With the resolution of the *James Webb Space Telescope* (JWST), the application YSO counting can potentially be extended to Andromeda. But for farther galaxies where individual YSOs can not be resolved, observers commonly use Hα emission to trace the photoionization effect of recently formed massive stars, and convert the total Hα luminosity into an estimate of the SFR. This requires both the assumption of an underlying IMF, and the correction for absorption of the Hα line by dust in dusty regions (Kennicutt & Evans 2012). When mimicking these techniques in the synthetic observations, YSO counting can be simply reproduced by selecting all stellar particles with ages < 2 Myr in the simulation. To produce a synthetic Hα map, by contrast, we need to calculate the local electron and proton density and the recombination coefficient to derive the Hα luminosity.

1.5 This work

While much effort has been made to study GMCs with both observations and theoretical modeling, there still remain many open questions: how large is the variation of SFE across different clouds? What is the role of magnetic fields during GMC formation? And how different are the star formation processes in extragalactic clouds from the local ones? Answering these questions requires precise measurements of cloud physical properties, which are hindered by systematic errors from projection, chemical, and excitation effects. Firstly, the three-dimensional (3D) structure reconstructed from projected two-dimensional (2D) observations is very likely to deviate from the intrinsic one, leading to large errors of 3D quantities like volume density. Moreover, emission from GMCs strongly depends on the local chemical composition and excitation, which is non-uniform throughout the cloud and can make the measurements spatially biased towards certain parts of the cloud. Removal of these biases can greatly enhance our understanding of GMCs and star formation.

With the recent development of astrochemistry post-processing tools and simulations with realistic stellar feedback algorithms, we now have the ability to study the effects above in detail. The motivation for this thesis is: to produce realistic synthetic observations from advanced simulations by exactly following the observational techniques, and to build an accurate model of the GMC life cycle and the star formation process within.

This thesis is constructed as follows: Chapter 2 studies the star formation efficiencies of 12 molecular clouds in the Solar neighborhood with the help of a 3D density reconstruction model, and measures a small dispersion of $\epsilon_{\rm ff}$ both in and across GMCs. The result suggests that star formation is mainly regulated by cloud-scale physical processes. In Chapter 3 we focus on the problem of how could molecular clouds form out of sub-critical neutral ISM. By carefully generating synthetic Zeeman effect observations, we find that the sub-critical results in previous observations are caused by systematic biases, and that in reality magnetic fields are not strong enough to prevent gravitational collapse even in predominantly atomic gas. We further compare two commonly used SFR tracers, Hα emission and YSO counting, in Chapter 4, and find significant spatial mismatches between them on sub-100 pc scales. Such discrepancy is however limited in dense regions, allowing us to develop a calibration model for Hα-traced SFR in massive GMCs. We then summarize the discoveries of this thesis and propose future work in Chapter 5.

Chapter 2

High-precision star formation efficiency measurements in nearby clouds

Context and Contribution

This chapter has been previously published as High-precision star formation efficiency measurements in nearby clouds, by **Zipeng Hu, Mark R. Krumholz, Riwaj Pokhrel, and Robert A. Gutermuth, 2022, MNRAS, 511, 1431-1438**. *The work is presented here exactly as in the publication. I have analyzed the observation data. I have written the majority of the paper, with inputs and suggestions from co-authors.*

Abstract

On average molecular clouds convert only a small fraction $\epsilon_{\rm ff}$ of their mass into stars per free-fall time, but different star formation theories make contrasting claims for how this low mean efficiency is achieved. To test these theories, we need precise measurements of both the mean value and the scatter of $\epsilon_{\rm ff}$, but high-precision measurements have been difficult because they require determining cloud volume densities, from which we can calculate free-fall times. Until recently, most density estimates treated clouds as uniform spheres, while their real structures are often filamentary and highly non-uniform, yielding systematic errors in $\epsilon_{\rm ff}$ estimates and smearing real cloud-to-cloud variations. We recently developed a theoretical model to reduce this error by using column density distributions in clouds to produce more accurate volume density estimates. In this work, we apply this model to recent observations of 12 nearby molecular clouds. Compared to earlier analyses, our method reduces the typical dispersion of $\epsilon_{\rm ff}$ within individual clouds from 0.16 dex to 0.12 dex, and decreases the median value of $\epsilon_{\rm ff}$ over all clouds from ≈ 0.02 to ≈ 0.01. However, we find no significant change in the ≈ 0.2 dex cloud-to-cloud dispersion

of $\epsilon_{\rm ff}$, suggesting the measured dispersions reflect real structural differences between clouds.

2.1 Introduction

Star formation is inefficient. A star forming region with little resistance to self-gravity will convert its gaseous mass to stars within a single free-fall time $t_{\rm ff} = \sqrt{3\pi/32G\rho}$, where ρ is the volume density. The ratio of the actual gas depletion time $t_{\rm dep}$ to $t_{\rm ff}$ is called the star formation efficiency per free-fall time $\epsilon_{\rm ff}$ (Krumholz & McKee 2005). Zuckerman & Evans (1974) were the first to point out that the observed star formation rate of the Milky Way as a whole implies that, averaged over all molecular clouds, $\epsilon_{\rm ff} \ll 1$. Krumholz & Tan (2007) extended this conclusion to the denser parts of molecular clouds traced by HCN, and more recent work has obtained $\epsilon_{\rm ff} \sim 0.01$ both for nearby clouds (e.g., Evans et al. 2014; Heyer et al. 2016; Lee et al. 2016; Ochsendorf et al. 2017) and for $\sim$ 100 pc-scale patches in nearby galactic discs (e.g., Krumholz et al. 2012; Utomo et al. 2018). The study-to-study dispersion in $\epsilon_{\rm ff}$ is ≈ 0.3 dex, while the dispersion within any single study is about $0.3 - 0.5$ dex (Krumholz et al. 2019).

Theoretical efforts to explain the origin of observed low $\epsilon_{\rm ff}$ values can be categorized into two main types. Some theories focus on galactic scale physical processes (e.g. Kim et al. 2011; Ostriker & Shetty 2011; Faucher-Giguère et al. 2013), while others are developed from internal star formation regulation processes within individual molecular clouds (e.g. Elmegreen & Parravano 1994; Krumholz & McKee 2005; Hennebelle & Chabrier 2011; Krumholz et al. 2011; Federrath & Klessen 2012; Padoan et al. 2012). Despite predicting similarly-low mean $\epsilon_{\rm ff}$ values, the two types of models yield significantly different estimates for the *dispersion* of $\epsilon_{\rm ff}$ – models regulated on the cloud scale generally predict much smaller dispersions than those regulated on the galactic scale (Lee et al. 2016; Krumholz & McKee 2020). Therefore, it is important to measure cloud-scale $\epsilon_{\rm ff}$ values with enough fidelity to extract both its mean value and dispersion. The most accurate measurements to date are those of Pokhrel et al. (2021), thanks to two advantages over previous studies: first, they derived their column density maps from *Herschel* dust emission maps, which allow them to sample a substantially larger dynamic range of column density than previous studies using extinction maps. Second, they use the SESNA catalog (R. Gutermuth et al., in preparation) of young stellar objects (YSOs), which is much more complete in dense regions than earlier catalogues, and for the first time includes accurate corrections for contamination by extragalactic interlopers and edge-on disks (Gutermuth et al. 2008, 2009). They determine a median value $\log \epsilon_{\rm ff} = -1.59$ with a dispersion of 0.18 dex in a sample of 12 nearby molecular clouds.

However, most previous $\epsilon_{\rm ff}$ measurements, including those of Pokhrel et al. (2021), incur a substantial error when calculating the volume density, which is required for the free-fall time. The fundamental challenge is that the volume density is a three-dimensional quantity, which is not directly accessible in a two-dimensional observation. The most common practice in literature is to estimate the density by assuming that the area of interest is the projection of a uniform sphere, whose radius is equal to the mean radius of the projected shape. For a cloud with a total projected area A and a total mass M, this approximation gives a density estimate $\rho_{\rm sph} = 3M/4\sqrt{A^3/\pi}$. This method has been used by a number of studies in the Milky Way (e.g., Krumholz et al. 2012; Lada et al. 2013; Evans et al. 2014; Pokhrel et al. 2021) and in the Large Magellanic Cloud (Ochsendorf et al. 2017). While simple, this procedure likely introduces significant systematic errors, coming from two primary sources. One is that in the past decades, it has become clear that the interstellar medium is characterised mainly by filamentary structures (e.g. Schneider & Elmegreen 1979; Dobashi et al. 2005; Arzoumanian et al. 2011; André et al. 2014; Kainulainen et al. 2016), which results in elongated contours identified from column density maps. The mean density of such structure is likely to be different from that calculated with spherical assumption. Second, for fixed $\epsilon_{\rm ff}$, the star formation rate in a given volume of gas will be $\epsilon_{\rm ff} \int (\rho/t_{\rm ff})\, dV$, and thus the quantity of interest for measuring $\epsilon_{\rm ff}$ is the mass-weighted mean of $t_{\rm ff}^{-1}$. Since the relationship between free-fall time and density is non-linear, $t_{\rm ff} \propto \rho^{-1/2}$, this is not identical to the free-fall time computed from the mean volume density, which is what the spherical assumption measures. In a medium containing significant density structure, the two can differ substantially (e.g. Hennebelle & Chabrier 2011; Federrath & Klessen 2012; Federrath 2013; Salim et al. 2015).

Hu et al. (2021a, hereafter H21) recently proposed an alternative approach to estimate the free-fall time weighted mean density $\rho_{\rm eff}$, which is defined as

$$\rho_{\rm eff} = \left(\frac{\int \rho^{3/2}\, dV}{\int \rho\, dV} \right)^2, \tag{2.1}$$

where ρ is the local volume density and the integral is over the cloud volume. This method immediately yields the correct free-fall time for the purposes of estimating $\epsilon_{\rm ff}$. H21 analyse star formation simulations from Cunningham et al. (2018), and show that one can estimate $\rho_{\rm eff}$ with higher accuracy than is obtained from the simple spherical assumption by making use of the full two-dimensional (2D) column density distribution, rather than simply its mean. Applied to simulations, their method corrects a ≈ 0.13 dex overestimation and removes a ~ 0.25 dex scatter in $\epsilon_{\rm ff}$ caused by spherical assumption. In this paper, we apply this model to the observations of Pokhrel et al. (2020) and Pokhrel et al. (2021) in order to derive higher-accuracy $\epsilon_{\rm ff}$ measurements than have previously been possible. We summarise the observations in Section 2.2, introduce the Hu et al. model in Section 2.3.1, describe its application to the data Section 2.3.2, present the results of the analysis in Section 2.4, and draw conclusions in Section 2.5.

2.2 Observations

Our data reduction and analysis method is described in Pokhrel et al. (2020), and full details are provided there. Here we simply summarise for convenience. This study analyses 12 nearby star forming regions: Ophiuchus, Perseus, Orion-A, Orion-B, Aquila-North, Aquila-South, NGC 2264, S140, AFGL 490, Cep OB3, Mon R2, and Cygnus-X. For each region we have a matched protostellar catalogue and cloud column density map. The latter are derived from *Herschel*/PACS and *Herschel*/SPIRE imaging at 160, 250, 350, and 500 μm, convolved to a common resolution (André et al. 2010). To obtain the column density in each pixel, we fit the spectral energy distribution with a dust emission model where the only two free parameters are the temperature and the column density. The best-fitting column density can be equivalently expressed in column of H_2 molecules, $N(\mathrm{H_2})$, or column of gas mass $\Sigma_{\rm gas}$, which are related by $\Sigma_{\rm gas} = 2m_{\rm H}/XN(\mathrm{H_2})$, where $m_{\rm H} = 1.67 \times 10^{24}$ g is the hydrogen atom mass and $X = 0.71$ is the hydrogen mass fraction of the local interstellar medium (Nieva & Przybilla 2012). On the obtained column density map, we first mask pixels with the best-fitting dust temperature implies that the dust in that pixel falls on the Rayleigh–Jeans (R-J) tail of the modified black body spectrum across all *Herschel* bands, since in this case our fits represent only lower limits on the temperature, and thus the best-fit column densities are only upper limits. The exact temperature limits are provided in Table 2 of Pokhrel et al. (2020). Second, we mask pixels with derived column densities $N(\mathrm{H_2}) > 10^{23}\,\mathrm{cm^{-2}}$, because for these dust optical depth effects can be significant and thus fitted $N(\mathrm{H_2})$ values may only represent lower limits. The effect of both masks is negligible in our results, since for all clouds the masked regions constitute less than 0.5% of the cloud by either area or mass, and, for many clouds, no pixels are masked at all.

The SESNA catalog (R. Gutermuth et al., in preparation) we use for protostars is a combination of *Spitzer* and Two Micron All-Sky Survey observations (2MASS;

Skrutskie et al. 2006), spanning about 90 $\deg^2$. For the farthest target Cygnus-X, the deeper UKIDSS (Lawrence et al. 2007) near-IR Galactic Plane Survey (Lucas et al. 2008) is used. We mask parts of column density maps outside SESNA coverage. After removing field stars, we classify sources in the SENSA field with excess IR emission as Class I YSOs (embedded protostars), Class II YSOs (which have cleared their envelopes, but retain circumstellar discs), or contaminants by using flux selections and a series of reddening-safe colors (Gutermuth et al. 2009). We calculate $\epsilon_{\rm ff}$ from the counts of Class I YSOs, since these have a short lifetime of ≈ 0.5 Myr, and thus are less sensitive to time-varying star formation rates than Class II objects, which integrate over ≈ 2 Myr (see discussion in Section 5.1 of Pokhrel et al.).

Before analysing the data, we must first remove two types of contaminants. First, Class II objects may be misclassified as Class I if they are edge-on and the disc occults the central star. The median misclassification rate from recent studies (Gutermuth et al. 2009; Kryukova et al. 2012, 2014) is 3.5%, and we therefore reduce the count of Class I objects by 3.5% of the total count of Class II objects in the same area. Second, there are 4.5 ± 0.5 extragalactic contaminants per square degree whose colours are similar enough to YSOs for them to be included in the SENSA catalog for Class I objects. To compensate, we subtract 4.5 objects per square degree from our Class I YSO counts.

A final correction applies only to Cygnus-X, our most distant target. The YSO sensitivity for the SESNA catalog is ~ 0.1 M$_\odot$ for all other clouds, but in the case of Cygnus-X, its relatively large distance (~ 1400 pc), denser field stars, more regions of bright nebulosity, and shallower IRAC data result in a much lower YSO sensitivity (~ 1 M$_\odot$). Assuming a Chabrier (2003) IMF, this implies that the fraction of detected YSOs is 0.163 of the total present. Thus, we divide the Class I object count in Cygnus-X by this fraction to achieve a uniform sensitivity of 0.1 M$_\odot$ in our sample.

2.3 Methods

To predict the free-fall time weighted mean density $\rho_{\rm eff}$ from the spherical density $\rho_{\rm sph}$, we apply the method of H21 to contours generated from the *Herschel* column density maps. We first briefly introduce the model in Section 2.3.1, and then we present the application of this model to the observations in Section 2.3.2.

2.3.1 H21 model

To determine the relationship between ρ_{eff} and ρ_{sph}, H21 analysed simulations of the formation of low-mass star clusters in a dense molecular clump by Cunningham et al. (2018). These simulations include gravity, magnetic fields, turbulence, radiation feedback, and protostellar jets/outflows. Adopting a periodic box size of 0.65 pc, a dynamic resolution range of (1.6×10^{-4} pc, 2.5×10^{-3} pc), and gas with solar metallicity, they produce star formation efficiencies consistent with observations. We refer readers to Cunningham et al. for full details.

H21 construct synthetic dust observations of the simulations, and draw column density contours on the projected images at a range of column densities. For each contour that encloses one or more protostars, they measure both the true effective density ρ_{eff} of the enclosed mass and the density ρ_{sph} that one would derive from the spherical assumption. They also consider a number of other projected quantities that would be accessible to an observer, in order to search for an estimator for ρ_{eff} more accurate than just ρ_{sph}. They find that using the Gini coefficient g of the column densities enclosed by a contour allows a substantially better prediction of ρ_{eff}, and define the new estimator

$$\rho_g = 10^{kg-b}\rho_{\text{sph}}, \tag{2.2}$$

where ρ_g is the predicted value of ρ_{eff}, and $k = 4.6$ and $b = 0.93$ are coefficients determined by fitting the simulated data. We discuss how these are modified in the presence of observational bias in Section 2.3.2.

In order to accomplish our goal of obtaining high-accuracy estimates of ϵ_{ff}, it is important to understand the uncertainties in this relation. Although the values of k and b are fitted from exact simulation data without error bars, we can nonetheless estimate the errors on these quantities from bootstrapping. We randomly choose elements from simulation sample with replacement until we obtain a new sample with the same size as before. Then we fit equation 2.2 on this new sample and repeat this process for 10^4 times. We take our uncertainties to be the 16th and 84th percentiles of the fitted k and b values, which give $k = 4.6 \pm 0.1$ and $b = 0.93 \pm 0.03$. These errors are small enough that they are unimportant compared to the other effects we discuss below.

The mean of residual between ρ_g and ρ_{eff} is 0.18 dex. While this is a substantial improvement over ρ_{sph} (for which the residual is 0.42 dex), the mean residual of our model should still be considered as an error source in the calculation of ϵ_{ff} of a single region. When determining the overall mean ϵ_{ff} and its dispersion, however, we are calculating mean values and percentiles from a sample of many contours. In the analysis we present below, each measurement we make will represent an average over at least 20 distinct contours, with implies an upper limit of 0.04 dex on the contribution of our imperfect estimate of $\rho_{\rm eff}$ to the overall error budget of star formation efficiencies.

We conclude our discussion by addressing two possible concerns regarding the H21 method. First, the method implicitly assumes that star-forming clouds are approximately self-similar, so that the relationship between $\rho_{\rm eff}$ and $\rho_{\rm sph}$ is not determined by tiny-scale density structures that do not have any counterpart in the column density structure measured on scales accessible to the observations. This is an assumption, but it is a plausible one given both the simulations and the available observations. On the simulation side, H21 show that the absolute sizes of contours are very poor predictors of the $\rho_{\rm eff} - \rho_{\rm sph}$ relationship – exactly what we expect if the structure is close to self-similar. With respect to observations, we note that, due to the different distances of the clouds in our sample, the *Herschel* column density maps cover a resolution range from 0.02 pc to 0.24 pc. We do not find systematic differences in cloud structure between clouds observed with lower or higher physical resolution, indicating the self-similar assumption is valid at least within this range of scales.

A second concern is that, while H21 show that estimates of $\epsilon_{\rm ff}$ derived from ρ_g, which we denote $\epsilon_{\rm ff,g}$ are unbiased in the sense that the expectation value of $\epsilon_{\rm ff,g}$ matches the true value of $\epsilon_{\rm ff}$, this does not automatically guarantee that estimates for the *dispersion* of $\epsilon_{\rm ff}$ values derived using ρ_g, which we denote $\sigma_{\rm g}$, represent an unbiased estimate of the intrinsic dispersion $\sigma_{\rm eff}$. Indeed, if the residual errors of the estimated $\epsilon_{\rm ff,g}$ are random, then $\sigma_{\rm g}$ will naturally be larger than the intrinsic dispersion $\sigma_{\rm eff}$, which is why the goal of the H21 model is to make the errors in $\epsilon_{\rm ff,g}$ as small as possible. However, it is in principle possible for the expectation value of $\sigma_{\rm g}$ to be *smaller* than $\sigma_{\rm eff}$, if the errors in $\epsilon_{\rm ff,g}$ are correlated and directional, meaning that contours for which the true value of $\epsilon_{\rm ff,eff}$ is smaller than the mean over all contours tend to have positive errors, while for contours where the true value of $\epsilon_{\rm ff,eff}$ is larger than the mean, the errors tend to be negative. If such a correlation existed, it would artificially reduce the dispersion, leading us to underestimate rather than overestimate σ_g.

To investigate this scenario, we measure $\rho_{\rm eff}$ and ρ_g for each of the contours used in H21, and from these compute $(\epsilon_{\rm ff,g}/\epsilon_{\rm ff,eff})$ and $(\epsilon_{\rm ff,eff}/\epsilon_{\rm ff,eff,mean})$, where $\epsilon_{\rm ff,eff}$ is the true star formation efficiency (determined from the true mean effective density $\rho_{\rm eff}$ in the simulation), $\epsilon_{\rm ff,g}$ is the star formation efficiency inferred using ρ_g, and $\epsilon_{\rm ff,eff,mean}$

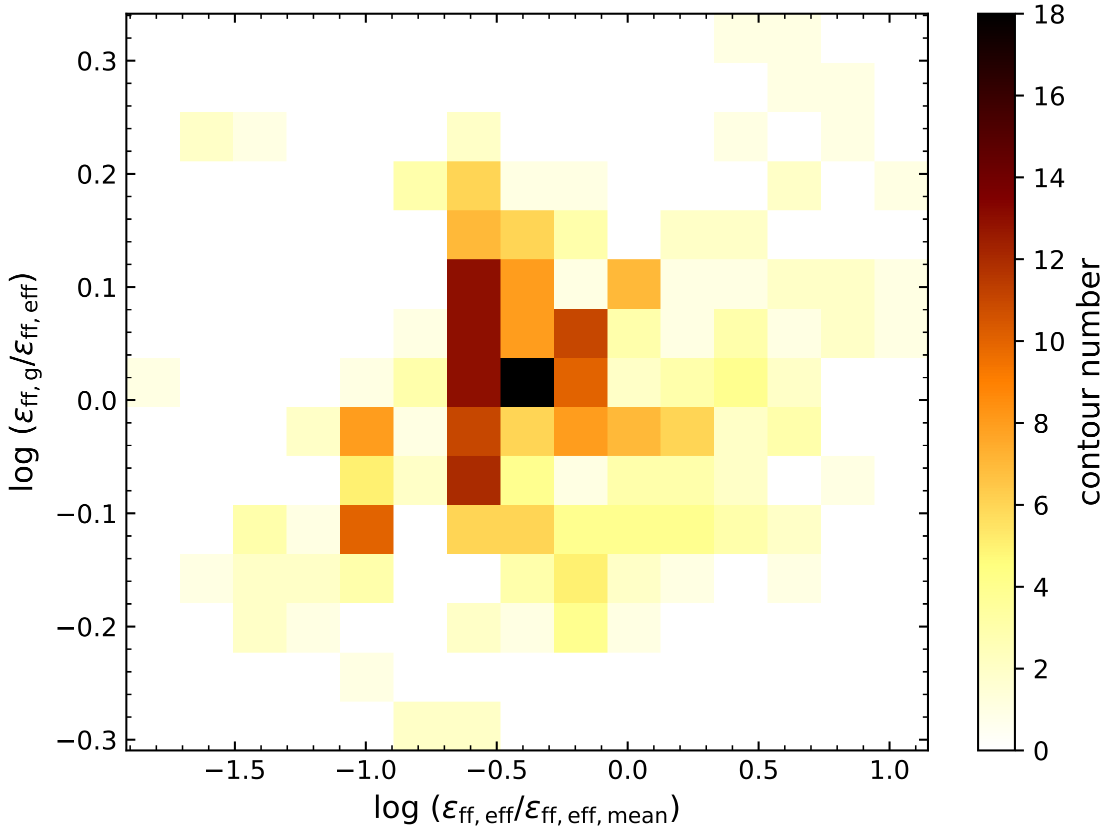

Figure 2.1: 2D distribution plot of $(\epsilon_{\rm ff,g}/\epsilon_{\rm ff,eff})$ versus $(\epsilon_{\rm ff,eff}/\epsilon_{\rm ff,eff,mean})$. The values are determined from simulation contours, and the color shows the number of contours in each bin.

is the mean value of $\epsilon_{\rm ff}$ over all simulation contours. We plot the joint distribution of these two ratios in Figure 2.1, and it is clear that there is no significant negative correlation, as would be required to render $\sigma_{\rm g}$ an underestimate of $\sigma_{\rm eff}$. Linear regression between these two ratio values returns a coefficient of determination $R^2 = 0.05$, confirming this visual impression. Thus we expect that errors in $\epsilon_{\rm ff,g}$ are randomly-directed, making the estimated star formation efficiency dispersion $\sigma_{\rm g}$ an upper limit of the intrinsic dispersion $\sigma_{\rm eff}$.

2.3.2 Application to *Herschel* observations

The first step in applying our method to the *Herschel* observations is to generate column density contours across the full range of $N(\rm H_2)$ covered by the observations. For each of the 12 regions, we start by finding the lowest $N(\rm H_2)$ value such that all pixels with column density above it are inside the SESNA coverage; equivalently, we set the minimum value of $N(\rm H_2)$ to be the lowest possible choice such that the contour sits entirely within the SENSA footprint. We define M_0 as the total gas mass enclosed by this contour. We then draw 100 $N(\mathrm{H}_2)$ contours at higher $N(\mathrm{H}_2)$, with the levels chosen such that the total mass above each level is equally spaced from M_0 to $M_0/100$ with a step of $M_0/100$; we only retain contours that contain at least one protostar, consistent with the selection we apply to the simulations in H21. We show an example of Ophiuchus cloud column density map with $N(\mathrm{H}_2)$ contours, protostar positions, and SESNA coverage area in Figure 2.2.

For every contour, we measure four values: total gas mass M_{gas}, total area A, completeness-corrected total protostar number N_{PS} and the Gini coefficient g of the surface density of all pixels within the contour (see H21 for details). From these parameters we derive 5 additional quantities: mean gas surface density $\Sigma_{\mathrm{gas}} = M_{\mathrm{gas}}/A$, star formation surface density Σ_{SFR}, the volume density ρ_{sph} and free-fall time derived from the spherical assumption $t_{\mathrm{ff,sph}}$ (see Section 2.1), and the corresponding star formation efficiency per free fall time $\epsilon_{\mathrm{ff,sph}}$. To calculate Σ_{SFR}, we assume the mean mass of protostars in SESNA to be $M_{\mathrm{PS}} \approx 0.5 M_\odot$ (Evans et al. 2009), and the mean duration of protostellar phase included in SESNA observations to be $t_{\mathrm{PS}} \approx 0.5$ Myr (Dunham et al. 2014, 2015). Thus, $\Sigma_{\mathrm{SFR}} = N_{\mathrm{PS}} M_{\mathrm{PS}}/A t_{\mathrm{PS}}$, and $\epsilon_{\mathrm{ff,sph}} = \Sigma_{\mathrm{SFR}}/(\Sigma_{\mathrm{gas}}/t_{\mathrm{ff,sph}})$.

Our next step is to account for the limited resolution and dynamic range of the observations, which is much smaller than that of the simulations. First consider the effects of resolution: the *Herschel* beam will smear out the density structure on scales comparable to the beam FWHM, and this will suppress the Gini coefficient. We must therefore remove from our sample contours small enough that beam-smearing precludes an accurate estimate of g. To do so, for each contour we compute the ratio of the mean contour radius $r = \sqrt{A/\pi}$ to the resolution R of the *Herschel* maps (expressed as the effective beam FWHM, taken from Table 1 of Pokhrel et al. 2020). To check when beam smearing becomes significant, we artificially blur our data: for each cloud we construct 8 column density maps smeared by Gaussian beams with sizes uniformly spaced between R and $20R$, and place contours on these smeared maps exactly as we do for the original maps. We plot the distribution of g values for all contours with $\Sigma_{\mathrm{SFR}} > 0$ in Figure 2.3. The figure clearly shows the expected effect: contours with small r/R have systematically smaller values of g than larger ones. To quantify this, we fit the distribution of $(\log(r/R), g)$ values with a piecewise linear function

$$g = \begin{cases} k(\log(r/R) - x_0) + y_0 & \text{if } \log(r/R) < x_0 \\ y_0 & \text{if } \log(r/R) \geq x_0 \end{cases}, \tag{2.3}$$

where k, x_0, and y_0 are free parameters. The green line shows the best fit, $k = 0.47$,

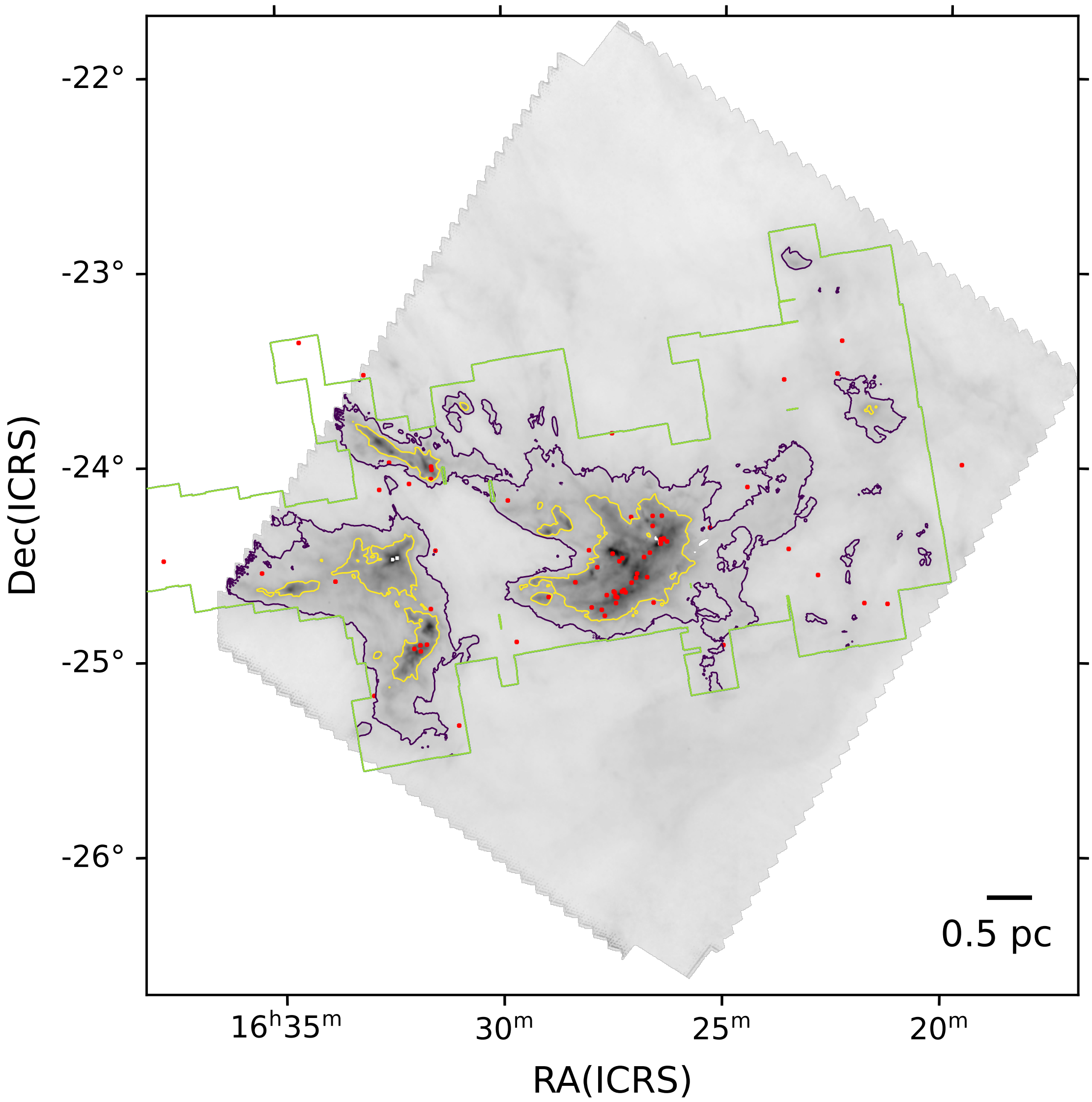

Figure 2.2: A column density map of the Ophiuchus Cloud derived from *Herschel* observations. The green contour is the Spitzer coverage area, and we we illustrate the largest contour that fits within this footprint in purple; the yellow contour is set at a level that encloses half as much mass as the purple one. The red dots are the positions of protostars.

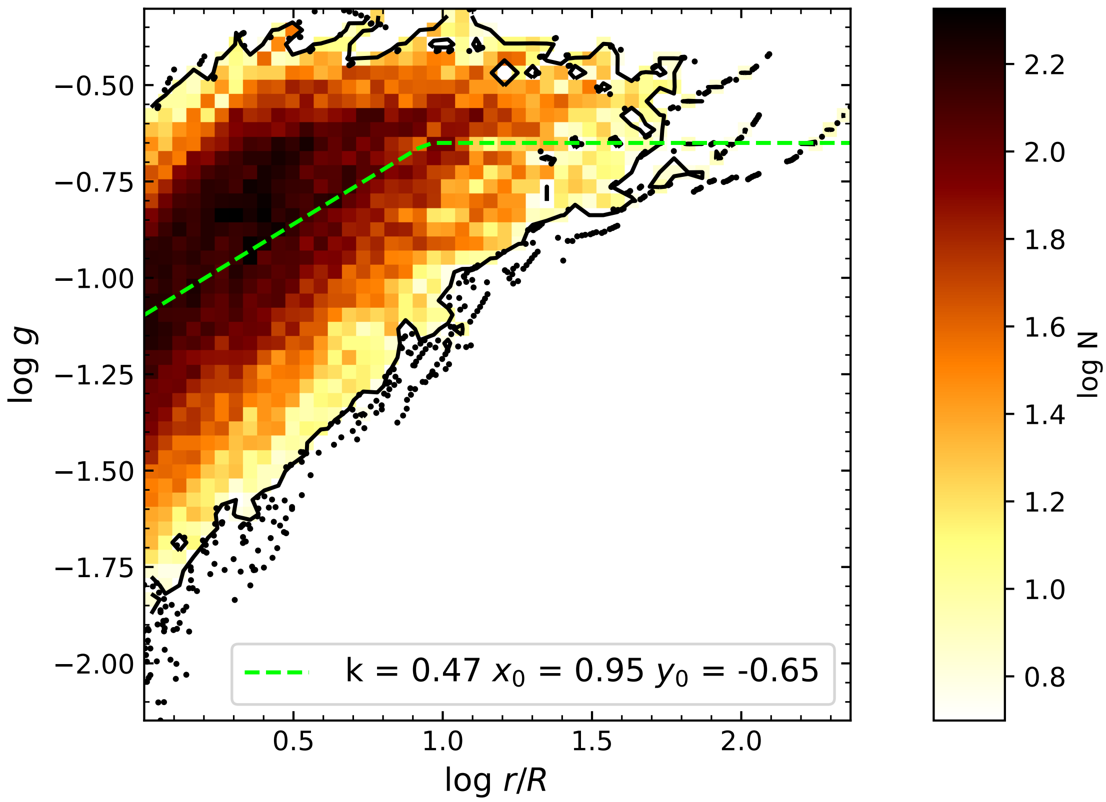

Figure 2.3: 2D distribution plot of g versus $\log(r/R)$. The values are determined from the smeared contours, and the color shows the number of contours in each bin (one black dot represents one single contour). The green dash line shows the piece-wise function equation 2.3 fitted to this distribution.

$x_0 = 0.95$, and $y_0 = -0.65$, which illustrates the effect in which we are interested: the distribution of g values becomes independent of resolution when $\log(r/R) \geq 0.95$, and drops below this threshold. We therefore remove from our analysis of the original, unsmeared maps any contour with $\log(r/R) < 0.95$. We also select contours that contain at least one protostar, since we obviously cannot compute $\epsilon_{\rm ff}$ values for those that contain none.

We perform a similar analysis to control for the effects of the limited dynamic range of the observations, i.e., the fact that there are minimum and maximum measurable values of $\Sigma_{\rm gas}$, and this in turn imposes limits on the maximum possible value of g. Define $\eta = \Sigma_{\rm gas,min}/\Sigma_{\rm gas,max} < 1$ as the ratio of minimum and maximum column densities within a given map contour. The value of η necessarily limits the range of g, since as $\eta \to 1$, the column densities within the contour all become the same, and clearly we must therefore have $g \to 0$.

This effect means that we must truncate our sample by discarding contours for which $\eta > \eta_{\rm max}$, where the value of $\eta_{\rm max}$ must be determined. To do so, we need to estimate the quantitative relation between g and η from the molecular cloud column density distribution. Previous observations has shown the column density distribution of molecular clouds can be characterised by a log-normal peak and a power-law tail towards to higher end (e.g. Kainulainen et al. 2009; Goodman et al. 2009; Froebrich & Rowles 2010; Lombardi et al. 2010; Schneider et al. 2011, 2015; Pokhrel et al. 2016); we concentrate on the power-law tail, since we only select star-forming contours with column density above average, and we find that our contours do indeed have approximately power-law distributions of pixel column density, with slopes ≈ -2. For such a distribution, $dN_\mathrm{p}/d\Sigma_\mathrm{gas} \propto \Sigma_\mathrm{gas}^\alpha$, if the range of measurable column densities is limited to Σ_min to Σ_max, the resulting Gini coefficient is

$$g = 1 - 2 \begin{cases} \frac{(3+2\alpha)\eta^{2-\alpha} - (\alpha+2)\eta^3 - (\alpha+1)\eta^{-2\alpha}}{(2\alpha+3)(\eta-\eta^{-\alpha})(\eta^{-\alpha}-\eta^2)}, & \alpha < -1, \alpha \neq -2 \\ \frac{\eta}{\eta-1} - \frac{1}{\log(\eta)}, & \alpha = -2 \end{cases}. \tag{2.4}$$

We can use this result to study where limited dynamic range begins to affect our results by examining the locations of our contours in the (η, g) plane – contours that lie near the upper limit suggest that our measured values of g may be compromised by limited dynamic range, while those that lie well below the limit are likely to suffer only minimal effects.

We plot 2D histograms of g versus $\log\eta$ for both our *Herschel* observations and for the C18 simulations, together with equation 2.4, in Figure 2.4. We see that, for both the simulations and observations, the distribution approaches the limit as $\eta \to 1$, but falls significantly below it when $\eta \ll 1$. Based on this figure, we choose to truncate our sample at $\log\eta_\mathrm{max} = -0.7$, since for both the simulations and the observations the data approach the maximum value of g for $\log\eta > -0.7$, but fall well below it for smaller η.

To ensure that our truncation of the sample at both small radii and small dynamic range does not create an inconsistency between the observations and our simulations, we apply the same cuts to the simulations and re-fit the relationship between ρ_eff, ρ_sph, and g, using the same method as described in H21. Doing so yields $k = 4.3 \pm 0.1$, $b = 0.84 \pm 0.04$, and a coefficient of determination $R^2 = 0.70$. The error range of k and b are obtained from half-sample fitting as described in Section 2.3.1. Such values are close to previous ones. For consistency, we will use the new fitted model coefficients throughout the rest of this manuscript.

Applying the down-selections described above to the *Herschel* data, we obtain 2905 contours that form the data set for further analysis. For all selected contours, we apply equation 2.2 (with the modified values of k and b) to determine their effective volume density ρ_g, and replace ρ_{sph} with ρ_g to recalculate the new result star formation efficiency denoted as $\epsilon_{\mathrm{ff,g}}$.

2.4 Results

With the properties determined from the unsmeared contours on different surface density levels, we first investigate how the triplet (g, $\epsilon_{\mathrm{ff,sph}}$, $\epsilon_{\mathrm{ff,g}}$) changes with Σ_{gas}. In Figure 2.5 we show the 2D histogram of g versus log (Σ_{gas}). We can find no significant relation between g and Σ_{gas} in this plot, which is consistent with the simulation results. The median value of g is $g_{\mathrm{median}} = 0.24$, which is above 0.2, the value for a uniform-density sphere (H21). This indicates that the free-fall time of most contours will be overestimated by the spherical assumption. For a typical Gini coefficient $g = 0.24$, our estimated uncertainties on k and b in equation 2.2 translate to an increase in the dispersion of ϵ_{ff} by 0.01 dex, which is negligible. For this reason, we will simply treat k and b as constants fixed to their central values for the remainder of this analysis. Similarly, given that we have an average of 300 contours per cloud, the 0.18 dex mean residual scatter of the H21 model corresponds to only a $\sim$ 0.005 dex scatter in the percentiles and mean values of ϵ_{ff}, negligibly small.

To study the difference between estimates of ϵ_{ff} derived using the spherical assumption and our improved method, we define two quantities: the mean star formation efficiency for an individual cloud $\langle\epsilon_{\mathrm{ff}}\rangle$, and the mean dispersion in star formation efficiency σ. We compute these as follows: for each cloud, we sort the contours by Σ_{gas} and place them in 10 bins of equal size, or fewer if that leaves a cloud with < 20 contours per bin. (Recall that Σ_{gas} is the mean gas surface density inside a given contour, not the contour level itself, so two contours at the same level still generally have different Σ_{gas}.) Within each bin, we denote the 16th, 50th, and 84th percentiles of ϵ_{ff} (for both $\epsilon_{\mathrm{ff,sph}}$ and $\epsilon_{\mathrm{ff,g}}$) as $\epsilon_{\mathrm{ff,16}}$, $\epsilon_{\mathrm{ff,50}}$, and $\epsilon_{\mathrm{ff,84}}$. We plot these quantities as a function of Σ_{gas} in Figure 2.6. We then define the mean star formation efficiency for one cloud $\langle\epsilon_{\mathrm{ff}}\rangle$ as [1]

$$\langle\epsilon_{\mathrm{ff}}\rangle = \frac{\int_{\log\Sigma_{\mathrm{gas,min}}}^{\log\Sigma_{\mathrm{gas,max}}} \epsilon_{\mathrm{ff,50}}\, d(\log\Sigma_{\mathrm{gas}})}{\log\Sigma_{\mathrm{gas,max}} - \log\Sigma_{\mathrm{gas,min}}}, \tag{2.5}$$

where $\Sigma_{\mathrm{gas,min}}$ and $\Sigma_{\mathrm{gas,max}}$ are the minimum and maximum contour surface density available for a given cloud; in terms of Figure 2.6, $\langle\epsilon_{\mathrm{ff}}\rangle$ is simply the mean value of the coloured line for each cloud. We evaluate this integral by approximating it as a

[1] In both equation 2.5 and equation 2.6, $\epsilon_{\mathrm{ff,16}}$, $\epsilon_{\mathrm{ff,50}}$ and $\epsilon_{\mathrm{ff,84}}$ are functions of Σ_{gas}

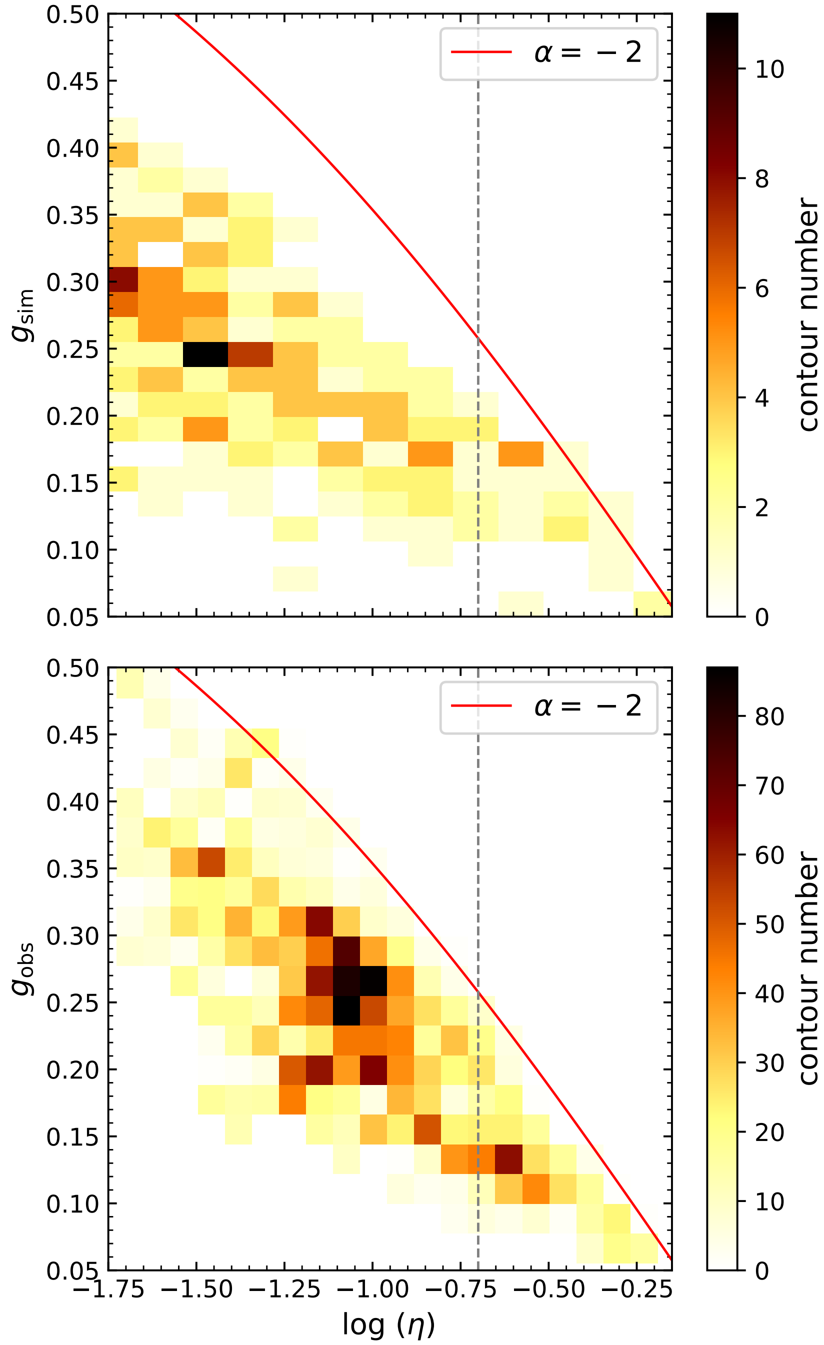

Figure 2.4: 2D histograms of contour Gini coefficients g and column density range $\log(\eta)$. Top panel: Simulation contours. Bottom panel: *Herschel* map contours. The solid line plots in both panels shows the theoretical value of g for contours with perfect power-law column density distributions with $\alpha = -2$ (equation 2.4), the approximate value we measure in both simulations and observations; results for other values of α within the uncertainty of the fits are nearly indistinguishable. The grey dashed vertical line shows $\log(\eta) = -0.7$. Note that the simulations, which have greater dynamic range than the observations, extend well beyond the range of η shown in the plot.

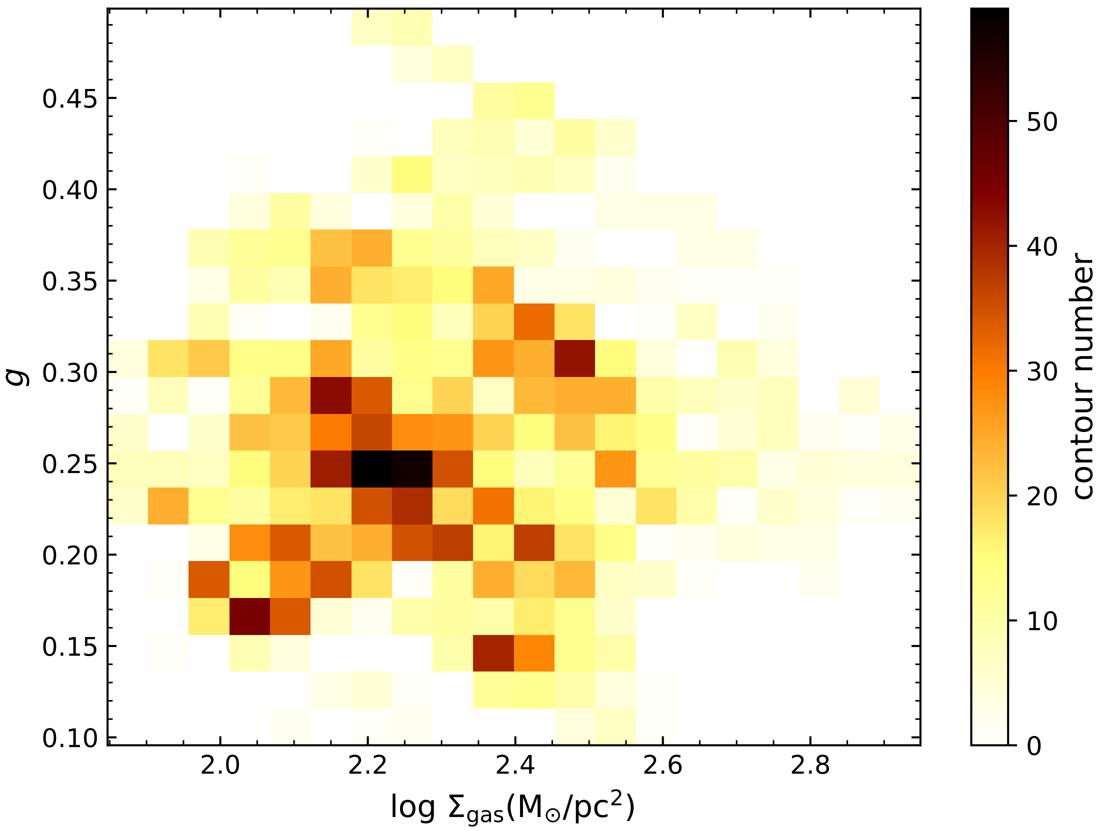

Figure 2.5: 2D histogram plot of g versus log $(\Sigma_{\rm gas})$. The values are determined from the unsmeared contours after all selections, and the color shows the number of contours in the bin.

finite sum over our groups. Similarly, we define the mean star formation efficiency dispersion σ as

$$\sigma = \frac{\int_{\log \Sigma_{\rm gas,min}}^{\log \Sigma_{\rm gas,max}} (\log \epsilon_{\rm ff,84} - \log \epsilon_{\rm ff,16})\, d(\log \Sigma_{\rm gas})}{2(\log \Sigma_{\rm gas,max} - \log \Sigma_{\rm gas,min})}, \tag{2.6}$$

where we again evaluate numerically as a finite sum over our bins of $\Sigma_{\rm gas}$. In terms of Figure 2.6, σ is simply half of the mean width of the grey band that surrounds each of the coloured lines.

We report the $\langle\epsilon_{\rm ff}\rangle$ and σ values we measure using the spherical assumption (denoted by subscript sph) and with equation 2.2 (subscript g) for all 12 clouds in Table 2.1. After applying our model, the median value of $\log\langle\epsilon_{\rm ff}\rangle$ decreases from $\log\langle\epsilon_{\rm ff,sph}\rangle = -1.73$ to $\log\langle\epsilon_{\rm ff,sph}\rangle = -1.90$. This is consistent with the prediction in H21 that use of the spherical assumption leads to a ~ 0.13 dex overestimation of $\epsilon_{\rm ff}$. We also measure the difference in dispersion $\Delta\sigma = \sigma_{\rm sph} - \sigma_{\rm g}$ derived using the spherical assumption versus using equation 2.2 for each cloud. We find that 8 of the 12 studied clouds yield positive $\Delta\sigma$, corresponding to a reduction in the dispersion; the mean reduction is $\Delta\sigma_{\rm mean} = 0.02$ dex. This demonstrates that our model does decrease the dispersion, but less than the ~ 0.15 dex found when testing the method on simulated data in H21. This is likely due to the difference between the simulated data and observations. H21 calibrate their method based on simulations from Cunningham et al. (2018) that use periodic boundary conditions, so the column density maps used in the calibration are from infinitely large self-similar clouds. The observed clouds, however, are from of finite size, so, for example, they can contain large-scale density gradients that are absent in periodic boxes. This suggests that we might obtain an improved version of equation 2.2 by analyzing a zoom-in galactic simulation.

For all 12 clouds, we determine the standard deviations (STD) of both types of $\langle\epsilon_{\rm ff}\rangle$ values: $\mathrm{STD}_{\rm sph} = 0.18$, and $\mathrm{STD}_{\rm g} = 0.22$. There is a slight increase after applying the H21 model, the reason for which might be that there are real physical differences between clouds that we have uncovered by not adopting the uniform spherical assumption. Given the relatively small $\Delta\sigma_{\rm median}$ we obtain, it is also interesting to ask whether we could forgo individualized corrections altogether, and simply adopt the median value $g = 0.24$ for all contours. Doing so would still produce a 0.1 dex median value decrease in $\epsilon_{\rm ff}$, while leaving the dispersion unchanged. However, such an approach would miss an important subtlety: while $g = 0.24$ is the median value for all contours on all scales, the value of g also changes systematically with size scale: on the largest scales of the 12 clouds we study, $g_{\rm median} = 0.35$. Properly accounting for this is crucial to obtaining the correct changes in $\epsilon_{\rm ff}$ versus $\Sigma_{\rm gas}$, and

Cloud	$\log\langle\epsilon_{\rm ff,sph}\rangle$	$\log\langle\epsilon_{\rm ff,g}\rangle$	$\sigma_{\rm sph}$ (dex)	$\sigma_{\rm g}$ (dex)	$\Delta\sigma$ (dex)	$\log\Sigma_{\rm gas}$ ($\mathrm{M}_\odot/\mathrm{pc}^2$)
Ophiuchus	-1.45	-1.59	0.18	0.13	0.05	(2.05, 2.79)
Persus	-1.76	-1.97	0.28	0.31	-0.03	(1.85, 2.67)
Orion-A	-2.12	-2.29	0.13	0.15	-0.02	(2.24, 3.00)
Orion-B	-1.86	-2.03	0.19	0.16	0.03	(2.10, 2.64)
Aquila-N	-1.79	-2.03	0.31	0.23	0.08	(2.02, 2.56)
Aquila-S	-1.69	-1.84	0.18	0.11	0.07	(1.92, 2.78)
NGC 2264	-1.84	-2.18	0.04	0.05	-0.01	(1.97, 2.77)
S140	-1.62	-1.78	0.04	0.03	0.01	(1.95, 2.36)
AFGL 490	-1.45	-1.56	0.01	0.00	0.01	(2.14, 2.32)
Cep OB3	-1.76	-1.82	0.13	0.11	0.02	(1.92, 2.41)
Mon R2	-1.69	-1.97	0.06	0.09	-0.03	(1.77, 2.48)
Cygnus-X	-1.63	-1.67	0.41	0.40	0.01	(1.90, 2.78)
Median	-1.73	-1.90	0.16	0.12	0.01	
Mean	-1.72	-1.89	0.16	0.15	0.02	
STD	0.18	0.22				

Table 2.1: Estimates of $\langle\epsilon_{\rm ff}\rangle$ and σ for individual clouds, using both the spherical assumption (values with subscript "sph") and the Gini model equation 2.2 (values with subscript "g"); $\Delta\sigma = \sigma_{\rm sph} - \sigma_{\rm g}$. The column $\log\Sigma_{\rm gas}$ reports the (min, max) contour average surface density measured for each cloud. Finally, the last three rows list the median, mean, and standard deviation values (STD) of the corresponding columns.

thus the correct $\Delta\sigma$ values within individual clouds. For this reason, we prefer to use individual-contour corrections when possible.

2.5 Conclusions

We use a new method proposed by H21 to combine column density maps derived from *Herschel* with young stellar objects from the SESNA catalog to determine the star formation efficiency per free-fall time $\epsilon_{\rm ff}$ in 12 nearby clouds. Our method provides a more realistic estimate of the mean volume densities of clouds seen in projection, reducing the error incurred by assuming that projected clouds are spherical, and allowing higher-precision estimates of $\epsilon_{\rm ff}$ than previously possible. We find that the spherical assumption leads to ~ 0.1 dex overestimation of $\log\langle\epsilon_{\rm ff}\rangle$, and also increases the estimated intra-cloud dispersion in $\log\langle\epsilon_{\rm ff}\rangle$ by ~ 0.02 dex on average. With our new method, we find that our sample of 12 clouds has a median star formation efficiency per free-fall time $\log\langle\epsilon_{\rm ff}\rangle = -1.9$, and the median spread in $\log\langle\epsilon_{\rm ff}\rangle = 0.12$ dex within a single cloud. The inter-cloud dispersion in $\log\langle\epsilon_{\rm ff}\rangle$ is nearly identical, at 0.2 dex, and this value is, within the uncertainties, unaffected by the use of the H21 model for the gas density. This strongly suggests that the intra-cloud dispersion we are measuring reflects a real variation in cloud properties, not an observational error.

Our results confirm the existence of a universal $\epsilon_{\mathrm{ff}} \sim 0.01$ value, and, importantly, let us identify a real ≈ 0.2 dex spread from cloud to cloud with 3D cloud geometry considered for the first time. As discussed in Pokhrel et al. (2021), such a small spread is in tension with models where star formation is regulated mainly by galactic-scale processes, but individual molecular clouds undergo rapid collapse (e.g. Kim et al. 2011; Ostriker & Shetty 2011; Faucher-Giguère et al. 2013). These models predict a much larger dispersion. Conversely, however, our measured spread in ϵ_{ff} can be used to evaluate the spread in parameters that enter models for cloud-scale regulation of star formation, which do predict dispersions comparable in size to the observed one. For example, in the turbulence regulated star formation of Krumholz & McKee (2005), a ~ 0.2 dex spread in ϵ_{ff} could naturally be explained by a $\sigma_\alpha \sim 0.3$ dex spread in cloud virial parameters (or a $\sigma_{\mathcal{M}} \sim 0.7$ dex spread in Mach number), while in the similar model of Hennebelle & Chabrier (2011) the required dispersion is $\sigma_\alpha \sim 0.8$ dex ($\sigma_M \sim 0.6$ dex), and for the model of Padoan et al. (2012) would require $\sigma_\alpha \sim 0.5$ dex. For comparison, Lee et al. (2016) study 195 star forming giant molecular clouds and find a scatter of 0.32 dex in the virial parameter. Thus observed clouds have approximately the level of dispersion in virial parameter required to reproduce the spread we see in ϵ_{ff}. In future work, we can use the same technique of high-precision estimates of ϵ_{ff} deployed here to search not just for the dispersion in ϵ_{ff}, but to look for systematic variations with virial parameter or other cloud properties, thereby opening up a new method for testing theories of star formation.

Acknowledgements

We acknowledge the anonymous referee for the insightful advice on this manuscript. MRK acknowledges funding from Australian Research Council awards DP190101258 and FT180100375. RP and RAG acknowledge support from NASA ADAP awards NNX15AF05G, 80NSSC18K1564 and NNX17AF24G. RP acknowledges funding from NASA ADAP award 80NSSC18K1564, and RAG acknowledges funding from NASA ADAP awards NNX11AD14G and NNX13AF08G. We further acknowledge high-performance computing resources provided by the Australian National Computational Infrastructure (grants jh2 and ek9) through the National and ANU Computational Merit Allocation Schemes, and by the Leibniz Rechenzentrum and the

Gauss Centre for Supercomputing (grant pr32lo).

This research has made use of data from the Herschel Gould Belt survey (HGBS) project, a Herschel Key Programme jointly carried out by SPIRE Specialist Astronomy Group 3 (SAG 3), scientists of several institutes in the PACS Consortium (CEA Saclay, INAF-IFSI Rome and INAF-Arcetri, KU Leuven, MPIA Heidelberg), and scientists of the Herschel Science Center (HSC).

Data Availability

The data underlying this article will be shared upon reasonable request to the corresponding author.

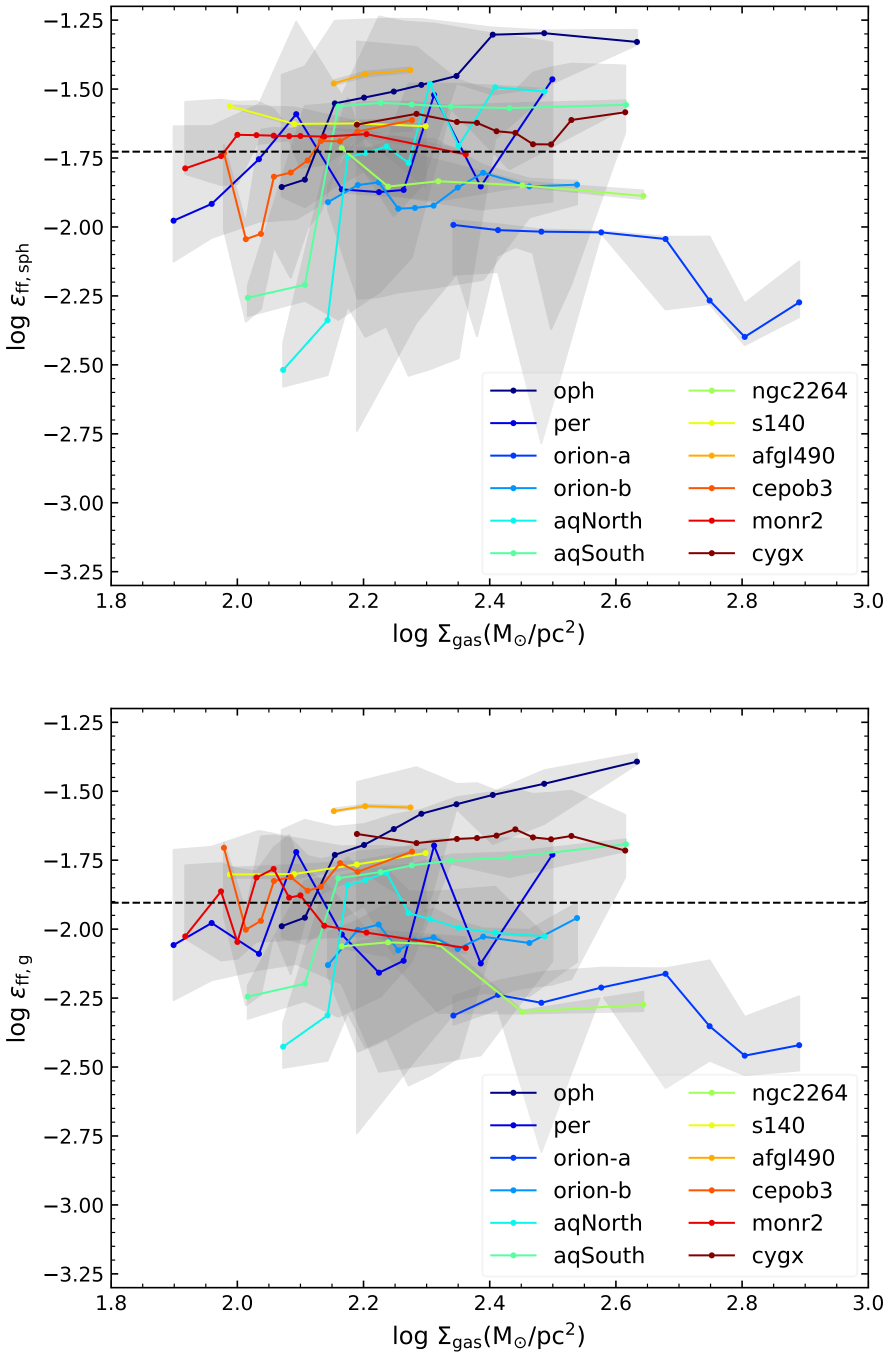

Figure 2.6: Distributions of log $\epsilon_{\rm ff,sph}$ (top) and log $\epsilon_{\rm ff,g}$ (bottom) as a function of log $\Sigma_{\rm gas}$. For each cloud, the coloured line and grey band show the 50th percentile and 16th-84th percentile range of $\epsilon_{\rm ff}$ in a bin of $\log \Sigma_{\rm gas}$. The black dashed lines show the median values $\langle\epsilon_{\rm ff,sph}\rangle$ and $\langle\epsilon_{\rm ff,g}\rangle$ over all clouds.

Chapter 3

The sub-critical illusion: synthetic Zeeman effect observations from galactic zoom-in simulations

Context and Contribution

This chapter has been previously published as The sub-critical illusion: synthetic Zeeman effect observations from galactic zoom-in simulations, by **Zipeng Hu, Benjamin D. Wibking, and Mark R. Krumholz, 2023, MNRAS, 521(4), 5604-5615**. *The work presented here is slightly modified from the published version. I have performed the simulations, produced the synthetic observations, and analyzed the data. I have written the majority of the paper, with inputs and suggestions from co-authors.*

Abstract

Mass-to-flux ratios measured via the Zeeman effect suggest the existence of a transition from a magnetically sub-critical state in H I clouds to a super-critical state in molecular clouds. However, due to projection, chemical, and excitation effects, Zeeman measurements are subject to a number of biases, and may not reflect the true relations between gravitational and magnetic energies. In this paper, we carry out simulations of the formation of magnetised molecular clouds, zooming in from an entire galaxy to sub-pc scales, which we post-process to produce synthetic H I and OH Zeeman measurements. The mass-to-flux ratios we recover from the simulated observations show a transition in magnetic criticality that closely matches observations, but we find that the gravitational-magnetic energy ratios on corresponding scales are mostly super-critical, even in the H I regime. We conclude that H I clouds in the process of assembling to form molecular clouds are already super-critical even before H_2 forms, and that the apparent transition from sub- to super-criticality between H I and H_2 is primarily an illusion created by chemical and excitation biases

affecting the Zeeman measurements.

3.1 Introduction

The dynamical importance of magnetic fields (B-field) relative to gravity during the star formation process remains an open question. Quantitatively, for a uniform spherically symmetric cloud of mass M, volume V, and radius R, threaded by a uniform magnetic field of intensity B, the ratio of magnetic to gravitational energy is

$$\frac{E_{\mathrm{mag}}}{E_{\mathrm{grav}}} = \frac{B^2 V}{8\pi} \times \frac{3R}{5GM^2} \propto \frac{B^2 R^4}{M^2} \propto \left(\frac{\Phi}{M}\right)^2, \tag{3.1}$$

where $\Phi = \pi R^2 B$ is the magnetic flux, which is conserved under ideal magnetohydrodynamics (MHD). Mouschovias & Spitzer (1976) show that clouds can collapse only if their mass-to-flux ratio M/Φ exceeds a critical value

$$\left(\frac{M}{\Phi}\right)_{\mathrm{crit}} = \frac{1}{3\pi}\sqrt{\frac{5}{G}}. \tag{3.2}$$

A cloud with $\mu_B \equiv (M/\Phi)/(M/\Phi)_{\mathrm{crit}} > 1$ is called super-critical, implying a weak magnetic field compared to gravity, while a cloud with $\mu_B < 1$ has strong magnetic field support against gravity and is called sub-critical. In a sub-critical cloud, the magnetic field strength will rapidly grow during a uniform gravitational collapse, preventing further contraction long before stars form (Mouschovias & Spitzer 1976). Thus if the bulk of the interstellar medium (ISM) is magnetically sub-critical, non-ideal MHD effects are required to allow stars to form. One candidate effect is the ambipolar diffusion (Shu 1977; Shu et al. 1987), whereby in the very poorly ionised regions found at high densities, neutral gas becomes decoupled from ions, allowing it to cross the field lines and further collapse. Alternately, turbulent motion of the gas might lead to magnetic reconnection and change the B-field topology, releasing magnetic flux and enabling collapse (Vishniac & Lazarian 1999). Understanding whether such non-ideal processes are needed, and if so which ones are dominant, requires observational work to precisely measure the magnetic field structure both in and around molecular clouds.

The most direct method of measuring magnetic fields, and by far the least uncertain when it comes to measuring field strengths, is via the Zeeman effect, which reveals the strength of magnetic fields along the line of sight (B_{LOS}) via the frequency splitting these fields induce between the components of emission or absorption lines with different polarisations. By using a range of Zeeman-sensitive tracers (most commonly H I, OH, and CN), the method can cover a large range of total hydrogen column density (N_H). Crutcher (2012) summarizes the results of 5 Zeeman effect surveys (Crutcher et al. 1999; Bourke et al. 2001; Heiles & Troland 2004; Falgarone et al. 2008; Troland & Crutcher 2008), which show a clear transition at $N_\mathrm{H} = 10^{21-22}\,\mathrm{cm}^{-2}$: diffuse H I regions with lower column densities are mostly sub-critical, while OH and CN measurements that trace denser regions indicate that they are mostly super-critical. Troland et al. (2016) make much more precise Zeeman effect measurements with both H I and OH tracers in the Orion Veil, and Thompson et al. (2019) conduct an OH absorption line Zeeman effect survey in the molecular cloud envelopes. Both these studies find results consistent with the Crutcher (2012) review, showing a sub-critical to super-critical transition in the same column density range. The mechanism behind such a transition, however, is still unclear, partially due to the lack of observations in the atomic-molecular transition regime. In an early attempt to explore this regime, Ching et al. (2022) perform H I narrow self-absorption (HINSA) Zeeman effect observation on L1544, and their result suggests that the cloud is already super-critical when H_2 molecules start to form.

Partly in an attempt to probe the sub- to super-critical transition, quite a few theoretical works have also investigated magnetic fields in the cloud formation process using MHD simulations. Bertram et al. (2012) determine the mass-to-flux ratios in cores ($\sim$ 0.1 pc) and clumps ($\sim$ 1 pc) from their simulations starting with a range of initial magnetic field strengths. They find that the mass-to-flux ratio of the structures they form is only loosely related to the initial criticality of the large scale environment. The recent work by Ibáñez-Mejía et al. (2021) starts from a galactic-scale simulation with a box size of 1 kpc, then zooms into 3 dense clouds, reaching a maximum resolution of 0.1 pc. They report the criticality transition happens when the hydrogen number density $n_\mathrm{H} \approx 100$ cm^{-3}. Although these simulations produce results similar to observations, it is still unclear how the sub- to super-critical transition occurs, particularly since their simulations use ideal MHD. Priestley et al. (2022) produce synthetic molecular line observations from the prestellar cores in their non-ideal MHD simulations, and argue that magnetically sub-critical cores can actually appear super-critical in observations.

One significant limit of these works, however, is that they begin from an arbitrarily prescribed uniform magnetic field morphology, rather than a realistic galactic magnetic field structure. Given that observations indicate that magnetic fields are continuously connected from galactic to cloud scales (e.g., Li et al. 2014), this is a potentially significant issue. Moreover, none of the works published to date have solved the radiative transfer problem when producing H I 21 cm line synthetic observations, or fully solved the problem of non-local thermodynamic equilibrium (non-LTE) excitation for the Zeeman-sensitive OH lines. Since the regions of interest are precisely those where H I self-absorption is expected to be strongest (as illustrated by the Ching et al. 2022 HINSA observations), and where the density is well below the OH critical density, this is another potentially significant limitation.

In this paper we study the transition between the sub-critical and super-critical ISM using ideal MHD simulations that start from the scale of the whole galaxy and then zoom in to reach maximum resolutions in dense regions up to ≈ 0.4 pc. These simulations allow us to for the first time combine realistic galactic magnetic field structures with detailed dynamics on the cloud scale in a single self-consistent calculation. We post-process our simulations to derive realistic chemical compositions, and we then solve the radiative transfer equation including non-LTE excitation effects along different lines of sight to produce synthetic H I and OH observations. Our goal is to understand the extent to which observed mass-to-flux ratio accurately reflect the ratio of magnetic to gravitational energy in the 3D volume they probe, and, to the extent that they do so, to understand how the sub- to super-critical transition that appears in the observations arises in the true 3D structure of the gas and magnetic field as they assemble to form molecular clouds.

This paper is structured as follows: Section 3.2 summarises the numerical method and simulation data. Section 3.3 describes our post-processing analysis method to derive chemical composition, calculate radiative transfer, and produce the synthetic observations. Section 3.4 presents the comparison between synthetic observations and true 3D energy relations. Section 3.5 discusses the physical meaning behind the results, and possible future work in this area. Section 3.6 concludes the work done in the paper.

3.2 Simulation

Our work begins from a simulation of an entire galaxy. To produce synthetic OH Zeeman effect observations from this, we need to locate molecular clouds with strong OH emission. Then we can produce synthetic H I observations in the atomic regions surrounding the selected molecular clouds. To achieve this goal, the scheme of the simulations in this work has 3 main steps: (1) carry out MHD simulations of a full galaxy; (2) identify regions with strong OH emission; (3) re-simulate the formation history of the selected regions with higher resolution. We discuss both the numerical method and the detailed scheme of simulations in this section.

3.2.1 Numerical method

Our full-galaxy simulations are based on the galactic magnetic field structure simulation by Wibking & Krumholz (2023, hereafter WK22). Here we simply summarise the physics and numerical methods, and highlight areas where our treatment differs from that of WK22. For details on the remainder of the methods, we refer readers to WK22. We solve the equations of ideal MHD with the GIZMO code (Hopkins 2015; Hopkins & Raives 2016; Hopkins 2016), which uses a mesh-free, Lagrangian finite-mass Godunov method. The simulations include a time-dependent chemistry network that tracks the abundances of H I, H II, He I, He II, He III, and free electrons, and uses these abundances to calculate the atomic cooling rates due to hydrogen and helium. We also include metal line cooling, using cooling rates interpolated from a prescribed table as a function of density and temperature under the assumption of ionization equilibrium and solar metallicity. The table is computed with CLOUDY (Ferland et al. 1998), using the method of Smith et al. (2008) as applied in the GRACKLE chemistry and cooling library (Smith et al. 2017).

For gas particles with density $\rho_{\rm g}$ larger that a threshold $\rho_{\rm crit}$, we calculate a local star formation rate density

$$\rho_{\rm SFR} = \epsilon_{\rm ff} \frac{\rho_{\rm g}}{t_{\rm ff}}, \tag{3.3}$$

where $\epsilon_{\rm ff}$ is the star formation efficiency, $\rho_{\rm g}$ is the local gas density, and $t_{\rm ff}$ is the local gas free-fall time. As summarized in the review by Krumholz et al. (2019), $\epsilon_{\rm ff}$ has a mean value ≈ 0.01 across a wide density range, which is also the value we adopt. We set the value of $\rho_{\rm crit}$ to be approximately equal to the Jeans density at our mass resolution; in the simulations of WK22, the mass resolution $\Delta M = 859.3\ {\rm M}_\odot$, and we therefore set $\rho_{\rm crit} = 100\ {\rm m_H\ cm^{-3}}$, but we increase the mass resolution and thus $\rho_{\rm crit}$ in the zoom-in stages as described below. If $\rho_{\rm g} > 100\rho_{\rm crit}$, we increase $\epsilon_{\rm ff}$ to 1 in order to limit the computational cost, since high densities require correspondingly small time steps. This effectively sets an upper limit of $100\rho_{\rm crit}$ on the gas density resolved by the simulation, since gas particles with higher density will instantly be converted into stellar particles. Gas particles for which $\rho_{\rm SFR} > 0$ have probability

$$P = 1 - \exp(-\epsilon_{\rm ff}\Delta t/t_{\rm ff}) \tag{3.4}$$

of being converted to a star particle per time step of size Δt. Stellar particles represent clusters that only interact with the galactic environment via gravity and feedback.

While our treatment of star formation and cooling is identical to that of WK22 (other than our use of a higher $\rho_{\rm crit}$ at higher resolution), our treatment of stellar feedback is necessarily slightly different because our resolution will be high enough that stellar particles no longer represent clusters massive enough that we expect them to sample the full initial mass function (IMF). This matters because it means that we cannot compute stellar feedback simply by integrating over the IMF. Instead, for each stellar particle, we stochastically draw its stellar population from a Chabrier IMF (Chabrier 2005) through the stellar population synthesis code SLUG (da Silva et al. 2012; Krumholz et al. 2015), following the approach to using SLUG as a subgrid model described by Fujimoto et al. (2018) and Armillotta et al. (2019). We compute stellar evolution using the Padova stellar tracks (Bressan et al. 2012), and derive stars' ionising luminosities from their masses and ages using the "starburst99" spectral synthesis method (Leitherer et al. 1999). We determine which stars end their lives as type II supernovae, and the stellar ages at which those supernovae occur, using the tabulated results of Sukhbold et al. (2016). Our numerical treatment of ionisation and supernova feedback is identical to that of WK22; our method in the present paper differs only in how we determine the ionising luminosity, number, and timing of supernovae produced by a given stellar particle.

3.2.2 Zoom-in method

The original WK22 simulation follows a Milky Way-like galaxy at a mass resolution $\Delta M = 859.3$ $M_\odot$, insufficient to resolve the small, dense regions from which the OH lines used in Zeeman effect measurements arise. In order to capture these regions, we carry out two additional simulation stages to zoom into molecular clouds from the galactic scale. For the first stage, we use the $t = 0.6$ Gyr snapshot in WK22's MHD simulation as our initial condition. We choose this snapshot because both the mass-weighted mean magnetic field strength (6 μG) and total SFR (2 $M_\odot yr^{-1}$) are stable and close to the values observed for the present-day Milky Way. WK22 explore the properties of the simulated galaxy at this time in detail, so we will not discuss them further here.

As a first step toward increasing the resolution, at this point we switch the feedback prescription over to the SLUG-based method described in Section 3.2.1 and continue the simulation at the same resolution for another 0.1 Gyr. During this time the SFR undergoes a transient increase, since no supernovae occur for ≈ 4 Myr after the change in feedback prescription, but thereafter the SFR stabilises at around 3 $M_\odot$ yr^{-1} for the last 0.05 Gyr. Once the simulation reaches 0.7 Gyr of evolution, our next zoom-in step is that we replace each gas particle with 10 smaller particles, which are randomly distributed around the center of mass of their parent particle with a distance of 0.2 times the parental smoothing length. All other physical parameters remain the same during the split, except that the particle mass is divided by 10, and the smoothing length is divided by $10^{1/3}$. In this way we increase the mean gaseous mass resolution to ≈ 90 $M_\odot$. During this stage we also increase $\rho_{\rm crit}$ to 10^4 m_H/cm^3, which is approximately the Jeans density at the mass resolution we will reach during the next zoom-in stage; we use this value rather than the Jeans density during this simulation stage to ensure that there are no transients after we zoom in again. We continue this mid-resolution run for another 21 Myr, to $t = 0.721$ Gyr. We show the face-on gas surface density $\Sigma_{\rm gas}$ at this time in Figure 3.1.

In order to select regions for further zoom-in, we use the chemistry post analysis code DESPOTIC to derive the OH 1665 and 1667 MHz emission line luminosities of each gas particle; we provide details of our method for doing so in Section 3.3.1. For each gas particle we first determine its total luminosity $L_{\rm OH}$ as the sum of these 2 lines, then randomly select 7 particles with $L_{\rm OH} > (2/3)\max(L_{\rm OH})$, where the maximum is computed over all gas particles. We then draw a sphere with a radius of 0.3 kpc around each selected particle; we show these regions as white circles in Figure 3.1. We choose this radius to be close to the gaseous disc scale height 0.34 kpc. The free-fall times of the 7 spheres range from 1.2 Myr to 21 Myr, with a median value of 3.8 Myr. Therefore, simulating the last 10 Myr of these regions will be sufficient to reconstruct their formation history.

We record the particle IDs of all gas particles within the 7 spheres, then find them in an earlier simulation snapshot 10 Myr before the one shown in Figure 3.1 ($t = 0.711$ Gyr). Using the method described above, we split these gas particles into 10 again, reaching a mass resolution of 8.9 $M_\odot$; the corresponding Jeans length is ≈ 0.4 pc, which we can use as an estimate of the spatial resolution in the dense regions. We then re-simulate the last 10 Myr ($t = 0.711 - 0.721$ Gyr), so that the regions we will use in our final analysis have all been simulated for ≈ 1 free-fall time at our highest resolution. We refer to this final stage as the high-resolution run.

To check if the simulation result is consistent after splitting selected gas particles, we compare the face-on surface density maps of the mid- and high-resolution runs at t = 0.721 Gyr for one example region in Figure 3.2. We see that, as expected, the large-scale density structure is the same, but that the higher resolution case shows more structure at high $\Sigma_{\rm gas}$.

To derive some basic physical parameters on the molecular cloud scale (~ 100 pc), we draw $(100\ \mathrm{pc})^3$ cubes around the densest particle for each group of split particles in the last high-resolution snapshot. This size is close to the typical size of the largest molecular cloud complexes (Krumholz 2014b). In Table 3.1, we tabulate the total mass in the form of H I, $M_{\rm HI}$, total mass in H_2, M_{H_2}, volume-weighted

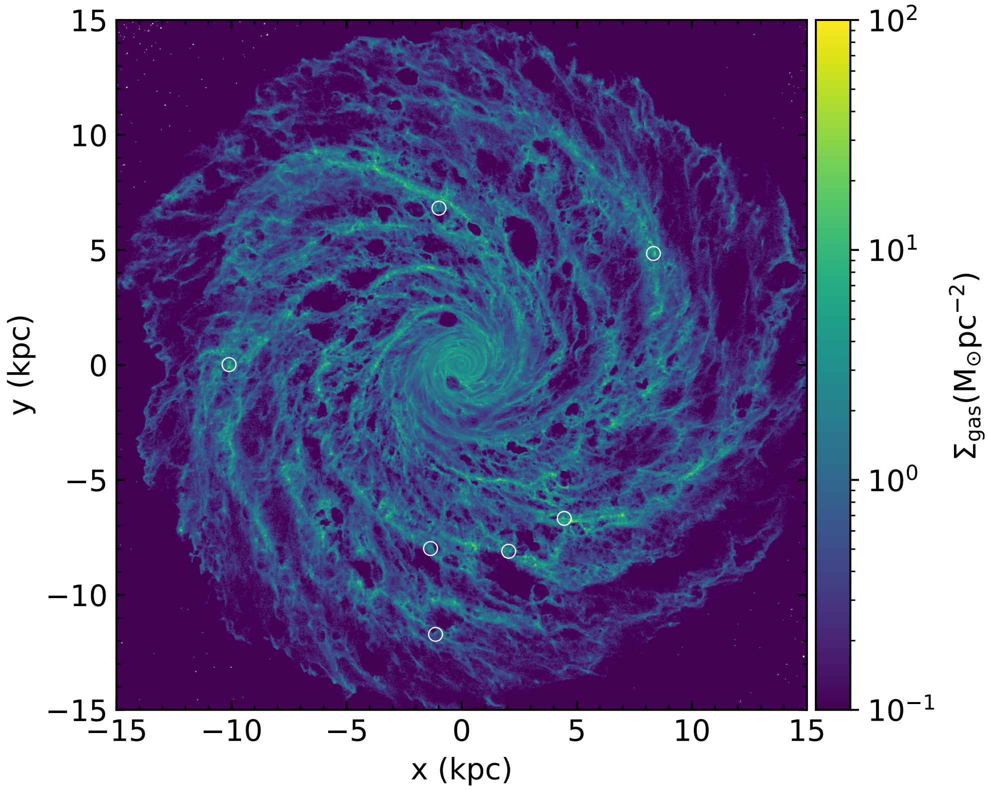

Figure 3.1: Face-on gas surface density map of the last snapshot ($t = 0.721$ Gyr) of the mid-resolution run. The 7 white circles, each of radius 0.3 kpc, are the high OH luminosity regions we select for the highest resolution simulation stage.

Cloud	$M_{\rm HI}$ (10^5 M$_\odot$)	$M_{\rm H_2}$ (10^5 M$_\odot$)	$\bar{n}_{\rm H}$ (cm^{-3})	$\bar{B}_V$ (μG)	$\bar{B}_M$ (μG)
1	0.35	0.23	5.0	2.7	5.1
2	0.26	0.54	5.8	1.4	4.9
3	0.35	0.72	6.6	1.2	9.9
4	0.55	0.75	8.3	1.2	7.9
5	1.1	1.4	16	15	22
6	1.0	3.0	20	7.2	20
7	1.6	10	53	17	48

Table 3.1: Physical parameters derived from (100 pc)^3 cubes drawn around the centres of mass of the high resolution regions at simulation time $t = 0.721$ Gyr. $M_{\rm HI}$ and $M_{\rm H_2}$ are the total mass in the form of H I and H$_2$, respectively. $\bar{n}_{\rm H}$ is volume weighted mean hydrogen number density. $\bar{B}_V$ and $\bar{B}_M$ refer to volume-weighted and mass-weighted mean magnetic field strength, respectively.

mean hydrogen number density, $\bar{n}_{\rm H}$, and volume-weighted and mass-weighted mean magnetic field strengths, $\bar{B}_V$ and $\bar{B}_M$, in each of these 7 cubes at $t = 0.721$ Gyr. We explain how we derive $M_{\rm HI}$ and $M_{\rm H_2}$ in Section 3.3.1.

3.3 Synthetic Observations

To study the mechanism behind the observed mass-to-flux ratio transition, we need to produce synthetic observations using methods that match real observational methods as closely as possible. This process consists of 3 main steps: (1) determine the chemical state of each gas particle, and its absorption and emission coefficients in the H I and Zeeman-sensitive OH lines, respectively; (2) solve the equation of radiative transfer to obtain synthetic spectra; (3) produce synthetic emission maps and B-field maps from the spectra, using the same techniques used to analyse observed spectra. We now proceed to describe these steps in detail.

3.3.1 Chemistry and excitation calculation

Since our simulation does not include molecular chemistry, and even simulations that do include chemistry (e.g., Glover et al. 2010) do not self-consistently compute non-LTE excitation (which is critical for the OH emission), we post-process our simulations using the DESPOTIC astrochemistry and radiative transfer code (Krumholz 2014a). DESPOTIC derives the equilibrium excitation, thermal, and chemical states of clouds from their elemental abundances (assumed to be Solar for the present work), radiation field environment, and physical properties. The thermal equilibrium calculation includes cosmic ray heating, molecule line cooling, the grain

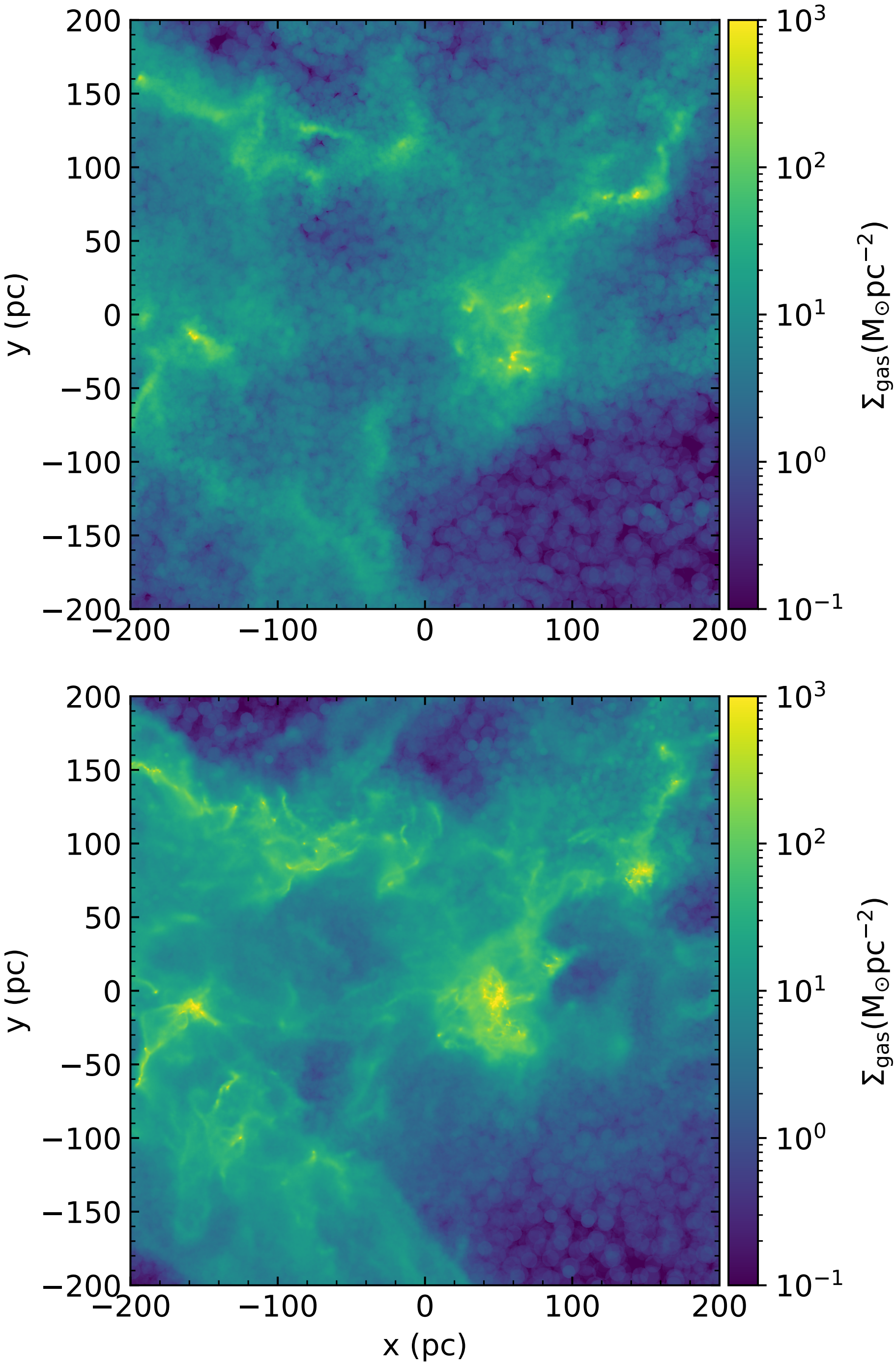

Figure 3.2: Face-on gas surface density maps of cloud 4 in the mid-resolution (top panel) and high-resolution (bottom panel) simulations at time $t = 0.721$ Gyr.

photoelectric effect, and collisional energy exchange between gas and dust, while the chemical equilibrium calculation adopts the H-C-O chemical network by Gong et al. (2017). The excitation calculation, which also determines optical depths for line cooling, uses the large velocity gradient approximation. We refer the readers to Krumholz (2014a) for more details on DESPOTIC.

We perform the chemistry post-analysis following the methodology of Armillotta et al. (2020). The first step is to generate tabulations of the H I and H_2 mass fractions, $X_{\rm HI}$ and $X_{\rm H_2}$, the OH transition line luminosities at 1665 and 1667 MHz, $L_{\rm OH,1665}$ and $L_{\rm OH,1667}$, and the gas temperature,[1] T, as a function of local velocity gradient, dv/dr, hydrogen number density, $n_{\rm H}$, and hydrogen column density, $N_{\rm H}$; note that $n_{\rm H}$ and $N_{\rm H}$ are the number of hydrogen nuclei per unit volume and per unit area, so these quantities are invariant under different chemical compositions. Since all 7 clouds are on spiral arms away from the galactic center, we assume the interstellar radiation field (ISRF) strength to be $\chi = 1\ G_0$, where $1\ G_0$ corresponds to the solar neighbourhood ISRF strength (Draine 1978). We set the primary cosmic ray ionization rate to a Solar neighbourhood-like value $\zeta = 10^{-16}\ \mathrm{s}^{-1}$. We run DESPOTIC on a grid of models covering the parameter range $n_{\rm H} = 10^{-2}-10^{6}\ \mathrm{cm}^{-3}$, $N_{\rm H} = 10^{19}-10^{25}\ \mathrm{cm}^{-2}$, and $dv/dr = 10^{-3}-10^{2}$ km/s/pc. The final grid is $21\times16\times15$ points in size in $(n_{\rm H}, N_{\rm H}, dv/dr)$ space, and is uniformly spaced in logarithm. We have verified by visual inspection that quantities of interest vary smoothly over our grid, so interpolation errors are small.

The second step is to assign values of $X_{\rm HI}$, $X_{\rm H_2}$, $L_{\rm OH,1665}$, $L_{\rm OH,1667}$, and T to each gas particle in the simulations by performing trilinear interpolation in the variables dv/dr, $n_{\rm H}$, and $N_{\rm H}$. We compute the hydrogen number density for each particle as

$$n_{\rm H} = \frac{X_{\rm H}\rho_{\rm g}}{m_{\rm H}}, \tag{3.5}$$

where $X_{\rm H} = 0.71$ is the mass fraction of hydrogen assuming Solar metallicity, $\rho_{\rm g}$ is the local gas density, and $m_{\rm H} = 1.67\times10^{-24}$ g is the mass of the hydrogen nucleus. For $N_{\rm H}$, we adopt the definition in Safranek-Shrader et al. (2017) as

$$N_{\rm H} = n_{\rm H} L_{\rm shield}, \tag{3.6}$$

where $L_{\rm shield}$, named as shielding length, represents the approximate length that

[1]Note that the temperature returned by the DESPOTIC calculation does not match the temperature found by GIZMO because the GIZMO calculation does not include molecular cooling, while DESPOTIC does; thus DESPOTIC generally yields lower temperatures in dense, molecular regions. This difference is unimportant for the dynamics, because in such cold regions thermal pressure is generally an unimportant force, but it matters a great deal for the excitation and radiative transfer calculations.

should be used in estimating the column density of material that shields the gas against the dissociating ISRF. Safranek-Shrader et al. (2017) show that the local approximation to the shielding length that most closely reproduces the results of detailed ray-tracing radiative transfer calculations is to set $L_{\rm shield}$ to the local Jeans length $L_{\rm J}$, with the Jeans length computed using the smaller of the local gas temperature and $T = 40$ K. Finally, we calculate the velocity gradient as

$$\frac{dv}{dr} = \|\nabla \times v\|, \tag{3.7}$$

where v is the local gas velocity. Our grid covers the full range of gas particle properties in the high-resolution simulations, so extrapolation off the grid is not necessary.

To illustrate the outcome of our interpolation procedure, in Figure 3.3 we plot the distribution of gas properties along a 100 pc ray through the minimum of gas temperature in cloud 4. This ray is along the x-axis as shown in Figure 3.2, and we set its coordinates in the transverse direction. In Figure 3.3 we sample the ray at 200 positions spaced at intervals of $\Delta L = 0.5$ pc. We compute the properties shown at each sampling point as a sum over nearby gas particles, weighted by their smoothing kernels following the GIZMO kernel weighting scheme described by Hopkins (2015). The upper panel shows the H I number density $n_{\rm HI}$ (pink), twice the H_2 number density $2n_{\rm H_2}$ (orange), and the gas temperature T (blue), while the bottom panel shows the angle-averaged, frequency-integrated emissivity in the OH 18 cm lines $j_{\rm OH,1665}$ (green) and $j_{\rm OH,1667}$ (red), together with line-of-sight velocity $V_{\rm LOS}$ (black), where we take the LOS direction to be along the ray. In these plots there is a clear transition from H I to H_2 in the central cold region, and we see that OH emission is confined to this region.

3.3.2 Radiative transfer

Our next step is to compute observable spectra. For OH this is straightforward, since Zeeman measurements are made using OH lines seen in emission, and observations indicate that the OH lines used are invariably optically thin. Thus we can compute the OH intensity as a function of velocity simply by integrating the emissivities returned by the DESPOTIC calculation along the line of sight. In practice, we do this by interpolating the particle data onto a 200^3 cube with a $\Delta L = 0.5$ pc voxel size centred on the densest particle; at each voxel we compute the OH emissivities in the 1665 and 1667 MHz lines by interpolating the particle data as described in Section 3.3.1 and used to construct Figure 3.3. We now consider lines of sight

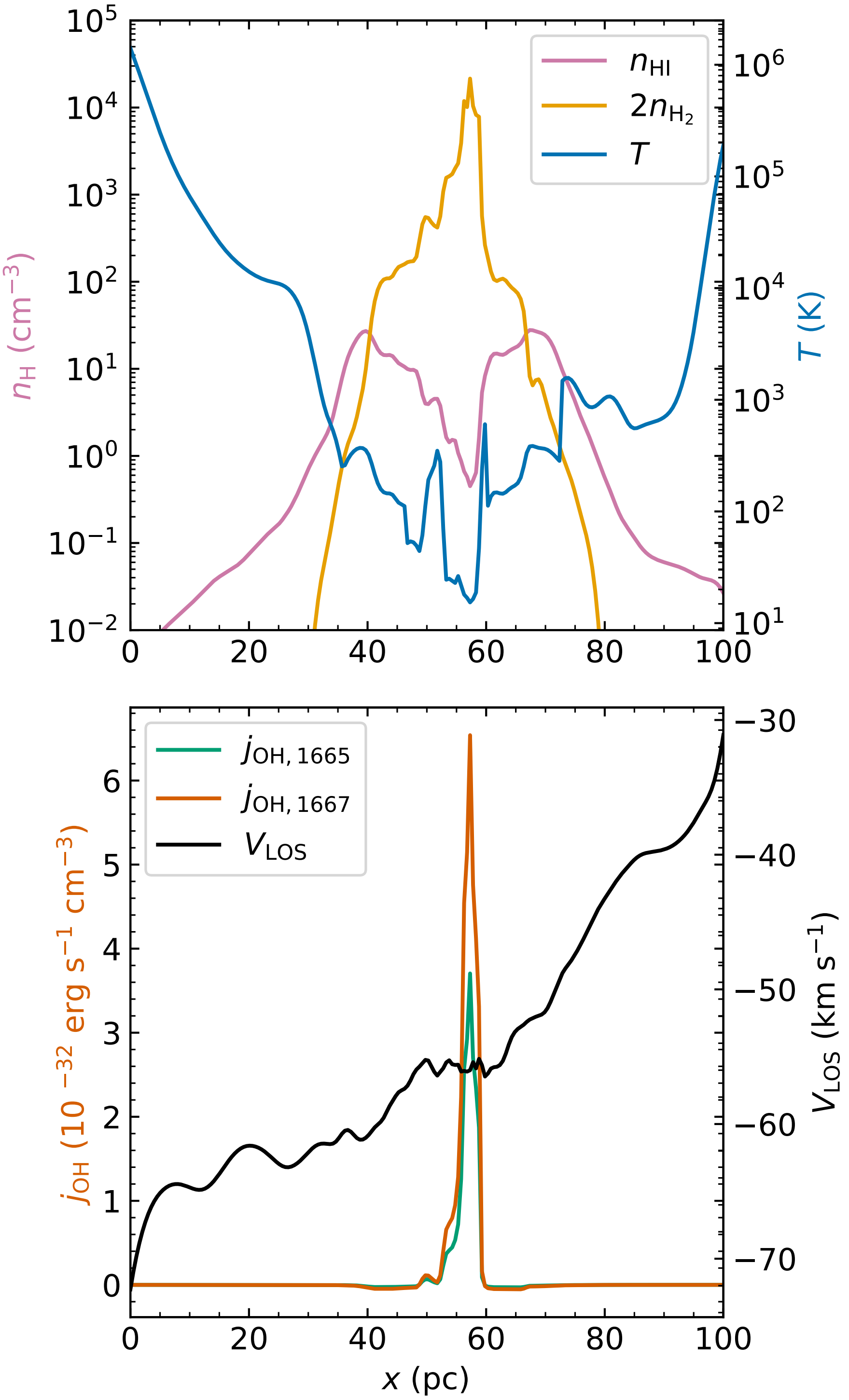

Figure 3.3: Gas properties along a 100 pc ray through the point of the lowest gas temperature for cloud 4; the ray is parallel to the x-axis shown in Figure 3.2. Top panel: number density of H nuclei $n_{\rm H}$ in the form of H I (pink) and H_2 (orange), together with local gas temperature T (blue). Bottom panel: frequency- and angle-integrated emissivity $j_{\rm OH,1665}$ (green line) and $j_{\rm OH,1667}$ (red line) in the OH 18 cm lines, and line-of-sight velocity $V_{\rm LOS}$ (black line).

(LOSs) through each pixel on the face of the cube in the x and y directions, i.e., the two directions that lie within the galactic plane; thus we have a total of 2×200^2 pixels for each of our 7 clouds. For each pixel, we determine its mass weighted mean line-of-sight velocity $\bar{V}_{\rm LOS}$, and consider a grid of velocities over a range $\bar{V}_{\rm LOS} \pm 10$ km/s with 0.1 km/s resolution. We then integrate the intensity in each pixel and at each velocity to produce our final OH spectra.

The situation for H I is more complex, because H I Zeeman measurements are generally made using absorption against background radio continuum sources (e.g., Heiles & Troland 2004), and comparing the on-source absorption profile against an off-source emission profile. We therefore require a full radiative transfer calculation for H I. Our first step in this calculation is to interpolate the particle data onto a regular cube exactly as for OH; at each pixel we have the H I and H_2 number densities $n_{\rm HI}$ and $n_{\rm H_2}$, along with the gas temperature T, gas velocity $\mathbf{v}$, and the local sound speed $c_s = \sqrt{k_B T/m_{\rm H}}$. Then we compute the H I emissivity j_ν and attenuation coefficient κ_ν as

$$j_\nu = \frac{3}{16\pi} A_{ul} E_{ul} n_{\rm HI} \phi_\nu \tag{3.8}$$

$$\kappa_\nu = \frac{3 A_{ul} h c \lambda_{ul} n_{\rm HI}}{32\pi k_B T} \phi_\nu, \tag{3.9}$$

where $\lambda_{ul} = 21.12$ cm is the transition rest wavelength, $E_{ul} = 5.87 \times 10^{-6}$ eV is the transition energy, $A_{ul} = 2.88 \times 10^{-15}$ s^{-1} is the Einstein coefficient, and ϕ_ν is the line shape function, given by

$$\phi_\nu = \frac{\lambda_{ul}}{\sqrt{2\pi} c_s} e^{-(V_c - V_{\rm LOS})^2/c_s^2}, \tag{3.10}$$

where V_c is the channel velocity and $V_{\rm LOS}$ is the component of the gas velocity $\mathbf{v}$ parallel to the LOS.

To produce absorption spectra against background radio sources, we assume that H I emission is negligible, and add up the optical depth along each LOS and for each velocity channel as

$$\tau_\nu = \sum_i \kappa_{\nu,i} \Delta L, \tag{3.11}$$

where i denotes the pixel number, increasing from $i = 1$ for the farthest pixel to $i = 200$ for the nearest one. To produce the corresponding H I emission spectra for an off-source observation, we solve the radiation transfer equation along the same lines of sight by iteratively evaluating

$$I_{\mathrm{HI},\nu,i+1} = e^{-\kappa_{\nu,i}\Delta L} I_{\mathrm{HI},\nu,i} + j_{\nu,\mathrm{i}}\Delta L, \tag{3.12}$$

for each velocity channel, where i again runs for 1 to 200. Our final emission spectrum is the intensity I_{HI} that emerges from the last pixel. In Figure 3.4 we show an example result of applying this procedure to the LOS shown in Figure 3.3; in the figure we plot the brightness temperature $T_{\mathrm{B}} = \lambda_{ul}^2 I_{\mathrm{HI}}/(2k_B)$ (top) and absorption fraction $e^{-\tau}$ (bottom) as functions of the channel relative velocity $\Delta V_{\mathrm{LOS}} \equiv V_c - \bar{V}_{\mathrm{LOS}}$.

3.3.3 Emission and B-field maps

After solving equation 3.12 for all LOSs, we can integrate the derived emission spectra over velocity to produce 2 maps of total H I 21 cm line intensity, I_{HI}, normal to x- and y-axis, respectively. We similarly produce maps of OH velocity-integrated intensity, I_{OH}, averaging the intensities of the 1665 and 1667 MHz lines. We compare the resulting H I and OH total intensity maps to the true column density map for cloud 4 (as shown in Figure 3.2) in Figure 3.5; the true column density N_{H} we show is integrated over the same 100-pc lines of sight used for the simulated emission maps. The three maps do not perfectly mimic each other. The N_{H} and I_{HI} maps differ because low N_{H} regions can be ionised and high N_{H} regions can be optically thick and can be dominated by H_2, all of which decrease the observed intensity. The OH map strongly picks out only the densest region, and due to varying excitation the OH intensity distribution does not perfectly mirror the total density distribution even in regions where there is strong OH emission.[2]

Our final task is to derive magnetic field measurements from the synthetic spectra. We do so using three of the Zeeman techniques described in Section 3.1: OH emission, H I absorption against a background radio source, and H I narrow self-absorption (HINSA).

When one uses OH emission lines to measure the magnetic field strength through the Zeeman effect, the emission regions that contribute more photons to the observer will contribute more to the measured B-field strength. Since the lines are optically thin and single-peaked, the contribution is simply linear in the emission. Therefore,

[2]Careful readers may note that the OH intensity I_{OH} shown in the bottom panel of Figure 3.5 can be slightly negative. This is a real effect, which occurs because differential selection rules for the upper and lower hyperfine states of the OH 1665 and 1667 MHz lines can drive the excitation temperatures below the CMB temperature, so the line is seen in absorption against the CMB. As a result the total intensity of the line, after subtracting off the CMB, can be slightly negative along some lines of sight.

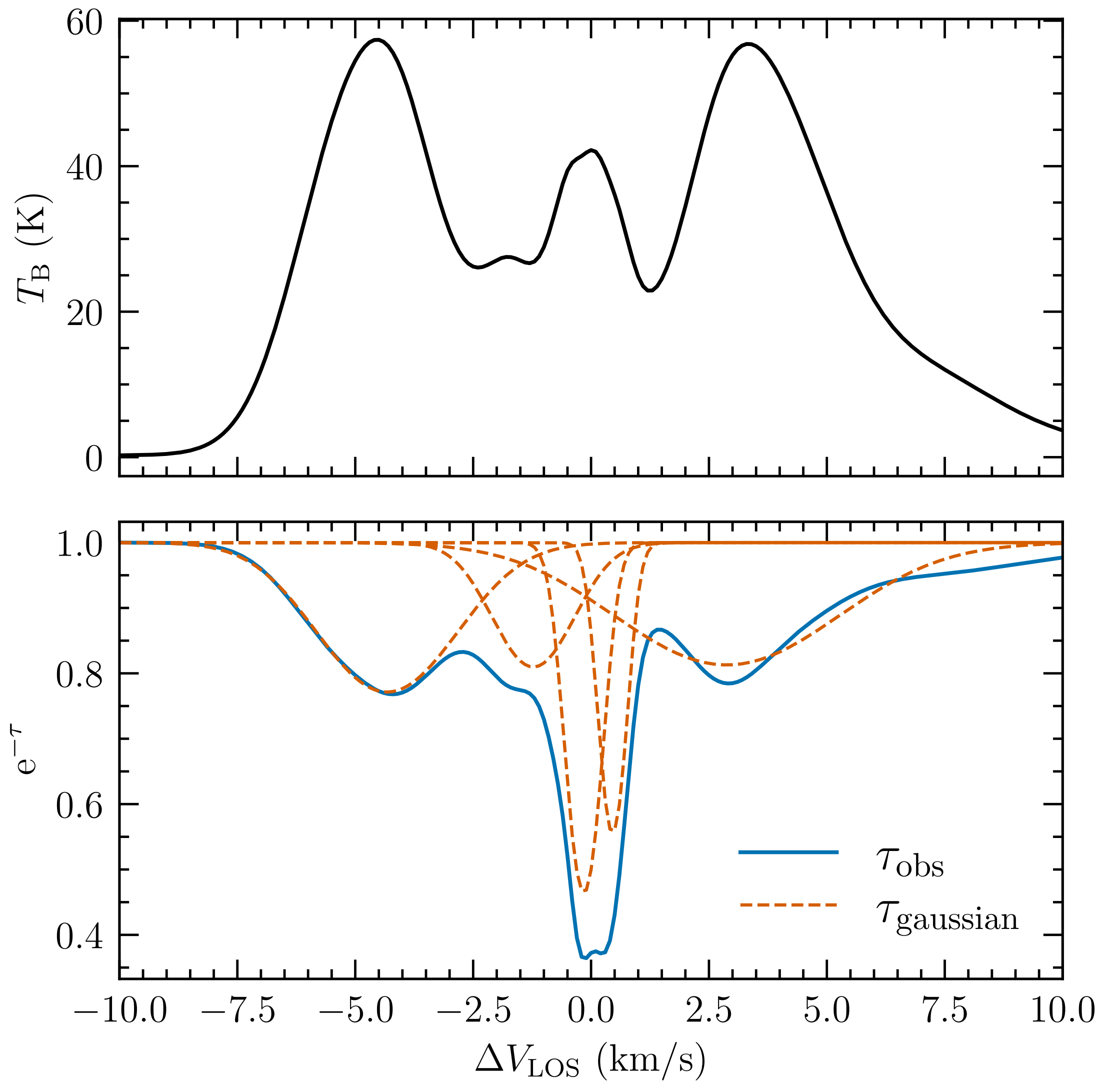

Figure 3.4: Top panel: the synthetic H I emission spectrum (off-source) corresponding to the LOS illustrated in Figure 3.3. T_B is the brightness temperature corresponding to the observed intensity, and ΔV_{LOS} is the difference between the velocity channel and the mass-weighted mean $\bar{V}_{LOS}$ of the whole LOS. The velocity resolution is 0.1 km/s. Bottom panel: absorption depth from the same LOS assuming the presence of a background radio continuum emitter (on-source). The blue line is the observed absorption fraction $e^{-\tau_{obs}}$, while the red dash lines show a decomposition of the absorption spectrum into Gaussian components.

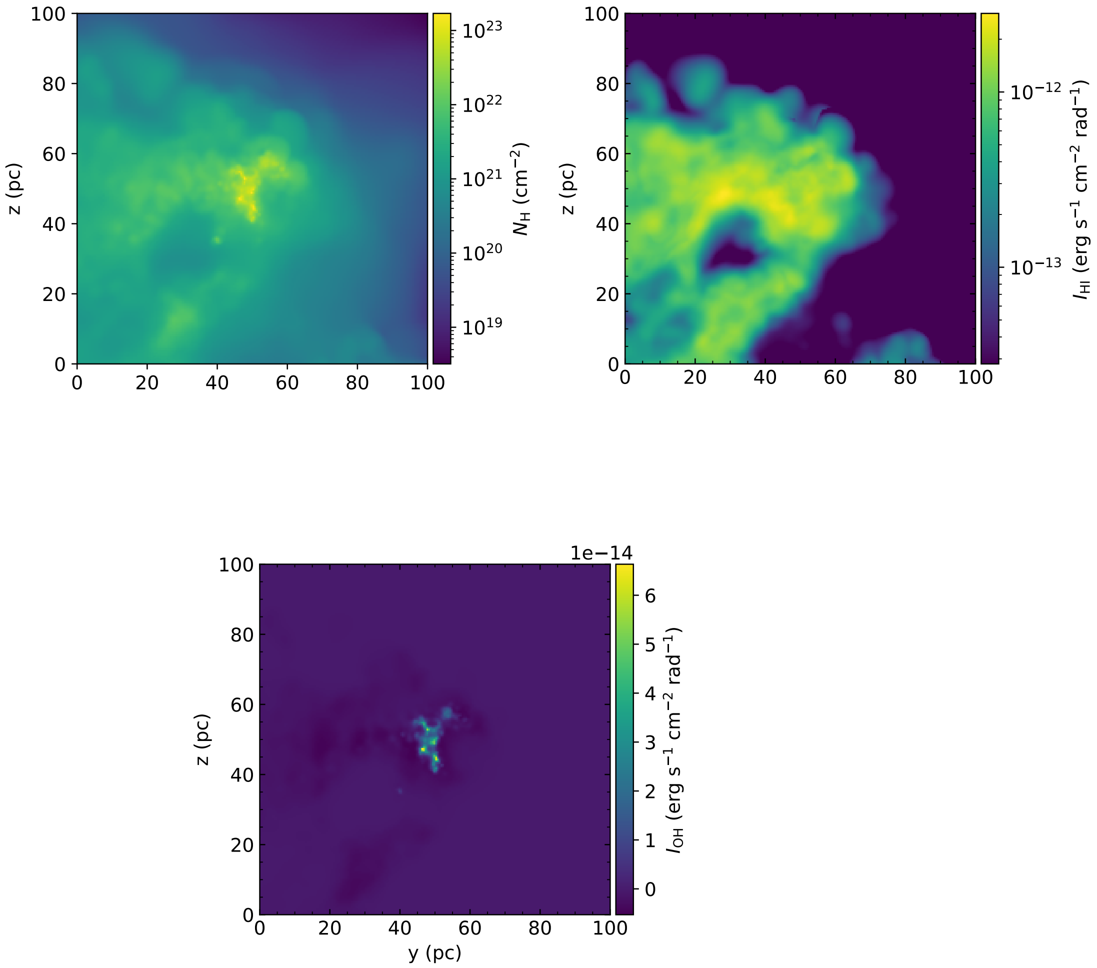

Figure 3.5: Maps from the x-axis projection of the (100 pc)^3 cube extracted around the densest gas particle in cloud 4. Left panel: total column density of hydrogen nuclei $N_{\rm H}$. Right panel: H I emission line velocity-integrated intensity $I_{\rm HI}$. Bottom panel: total intensity $I_{\rm OH}$ in the OH 1665 and 1667 MHz lines; the quantity we plot is the average of the two lines.

we approximate the magnetic field that would be inferred from the OH lines as simply the $L_{\rm OH}$-weighted mean line of sight magnetic field for both OH 18 cm lines. We then take the average of these two values as the final result $B_{\rm OH}$. In Figure 3.6, we compare the true, volume-weighed mean LOS magnetic field for cloud 4 projected along the x-axis with maps generated from synthetic OH observations. For $B_{\rm OH}$ we show only pixels where $I_{\rm OH} > I_{\rm OH,max}/100$ as a rough proxy for where the OH lines would be bright enough to be detectable.

We next consider H I absorption against a background radio continuum source, which is somewhat more complex since each H I absorption spectrum typically contains several cold neutral medium (CNM) components with different $V_{\rm LOS}$. To make separate measurements for each component, following the approach of Heiles & Troland (2004), we perform least-squares fits of at most 5 Gaussians to the absorption spectrum. The optical depth of a single component $\tau_{{\rm comp},\nu}$ is

$$\tau_{{\rm comp},\nu} = \frac{\tau_{\rm norm}}{\sqrt{2\pi\sigma_v^2}}\, e^{-(V_c - V_{\rm comp})^2/(2\sigma_v^2)}, \tag{3.13}$$

where $\tau_{\rm norm}$, σ_v and $V_{\rm comp}$ are parameters to be fit. We show the example of such a multi-component Gaussians as red dash lines in the bottom panel of Figure 3.4. Due to computational resource limitations, we do not perform this decomposition for all of our 5.6×10^5 spectra; instead, for each projection map we decompose 1000 randomly-selected LOSs, chosen out of the set with $N_{\rm HI} \in (10^{19},\ 10^{21.5})$ cm^{-2}, the same column density range observed in Heiles & Troland (2004).

Once we have decomposed the H I spectra, we next compute the synthetic Zeeman-inferred magnetic field for each. This requires some subtlety, because components in velocity space do not necessarily map onto real structures in physical space, as is implicitly assumed by the decomposition procedure used by Heiles & Troland (2004) and others. In such situations, the marginal contribution of the magnetic field in a particular fluid element in space to the magnetic field inferred for a particular Gaussian component will depend to some extent on the details of the decomposition and fitting procedure. However, generically we expect that the contribution of a particular voxel to the magnetic field inferred for a particular component to scale with both the total amount of absorption it contributes and with its marginal contribution to that particular component. We there define a weight w_i for each voxel i's contribution to a particular component of central velocity $V_{\rm comp}$ and dispersion σ_v as

$$w_i = e^{-(V_{\rm LOS,i} - V_{\rm comp})^2/(2\sigma_v^2)} \int k_{\nu,i} d\nu, \tag{3.14}$$

and the resulting synthetic B-field measurement for one Gaussian component as

$$B_{\mathrm{HI,comp}} = \frac{\sum_i w_i B_{\mathrm{LOS,i}}}{\sum_i w_i}. \tag{3.15}$$

We only perform the calculations above for Gaussian components with $\sigma_v < 2$ km/s, to make sure that most of the component lies within the spectral range we have extracted. From all selected LOSs we find 30853 components and derive $B_{\mathrm{HI,comp}}$ values for them.

Our final task is to make synthetic HINSA magnetic field measurements. Since HINSA only occurs where there is cold H I ($T \lesssim 100$ K), we first project only cold H I into column density maps, then find the pixel with the highest column density, and determine the B-field in the cold H I $B_{\mathrm{HI,cold}}$ from the 100-pc long LOS projected onto this pixel. From Figure 3.3 we can see that the cold H I region has nearly constant V_{LOS}, thus we can assume the Doppler profile shape is constant for the whole cold H I region, and determine $B_{\mathrm{HI,cold}}$ as

$$B_{\mathrm{HI,cold}} = \frac{\sum_{\mathrm{i,cold}} B_{\mathrm{LOS,i}} \int k_{\nu,i} d\nu}{\sum_{\mathrm{i,cold}} \int k_{\nu,i} d\nu}, \tag{3.16}$$

where $\sum_{\mathrm{i,cold}}$ means summation over pixels with $T \leq 100$ K. After 2 projections per cube, we have 14 $B_{\mathrm{HI,cold}}$ results. Note that we make only one measurement toward each cloud in order to mimic the approach of the published HINSA measurement (Ching et al. 2022), which is typically conducted along the line of sight through the HINSA maximum.

It is clear that the B-field strength and morphology highlighted by OH concretely differ from the mean B-field over the 100-pc-long LOS, indicating a possible inconsistency between the observed mass-to-flux ratio and the real overall magnetic-gravity energy relation. Since for each LOS we make several B_{HI} measurements from the fitted Gaussian components, individually, and the selected LOSs do not cover the whole (100 pc)^2 area, we can not show a B_{HI} map similar to Figure 3.6.

3.4 Results

In this section, we first reproduce the observed B-N relation with synthetic observations in Section 3.4.1, then explore how well this relation captures the true ratio of gravitational to magnetic energy from the full 3D simulation data in Section 3.4.2.

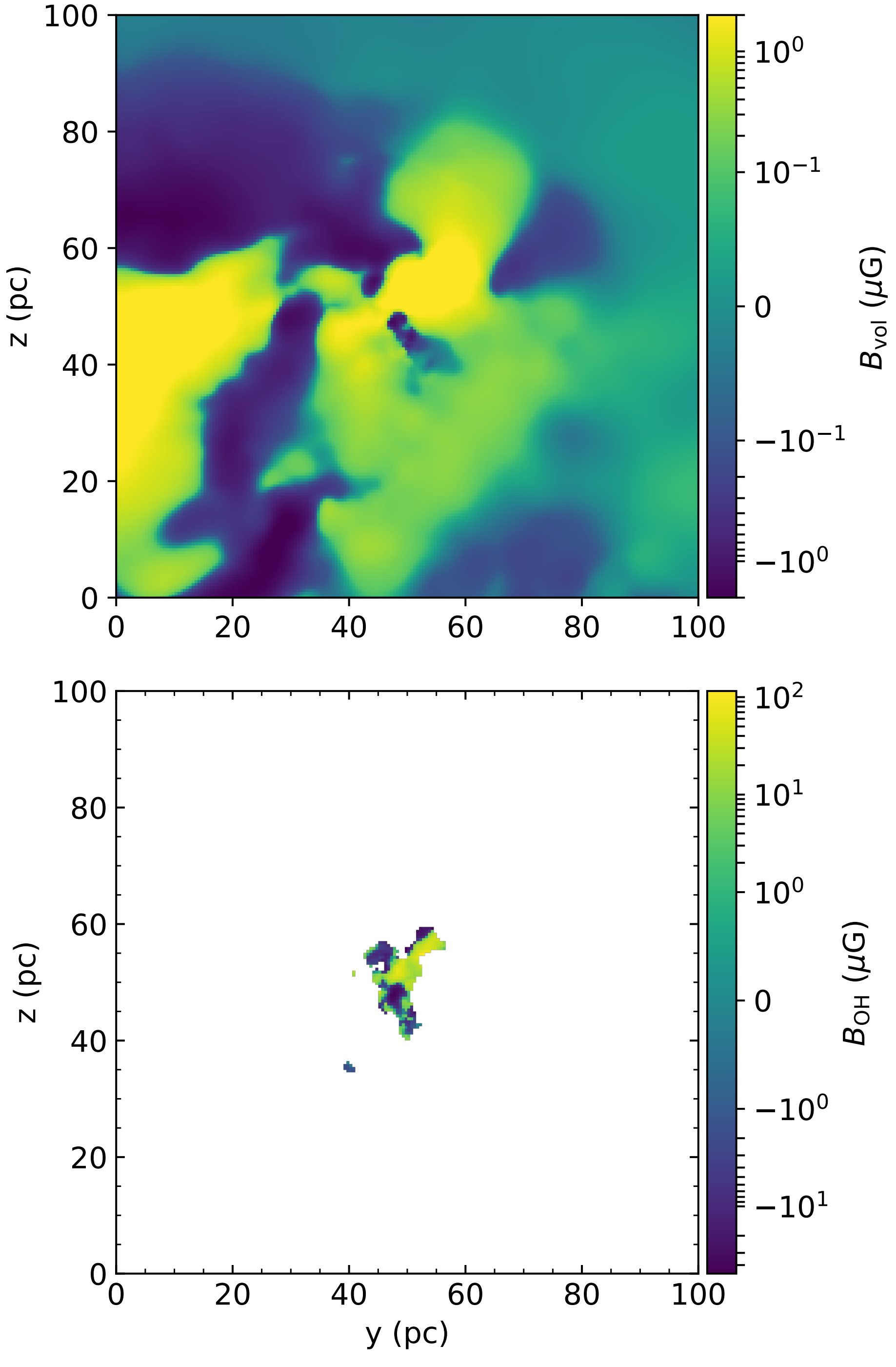

Figure 3.6: Line-of-sight magnetic field maps from the x-axis projection of the (100 pc)^3 cube extracted around the densest gas particle in cloud 4. Top panel: true, volume weighted mean line-of-sight magnetic field $B_{\rm vol}$ map. Bottom panel: magnetic field inferred from synthetic OH Zeeman observations, $B_{\rm OH}$. Note that we only show $B_{\rm OH}$ for pixels with total OH intensity $I_{\rm OH} > I_{\rm OH,max}/100$. Also note that the colorbar range differs in the 2 panels.

3.4.1 Magnetic field versus column density

After making the synthetic observations, we can now compare magnetic field to column density following Crutcher (2012), and look for the magnetic criticality transition. The pixel size is 0.5 pc in both Figure 3.5 and Figure 3.6, which is close to the $3'$ beam width of the Arecibo telescope when applied to a cloud at a distance of $\sim$ 300 pc. Therefore, we simply treat each pixel in the OH emission map as a synthetic beam, and directly take OH-inferred magnetic field values B_{OH} from the pixel values derived in Section 3.3.1. We similarly derive the corresponding column density from the emission intensity maps. Assuming the gas is optically thin (as is assumed in observations), we convert OH intensity into hydrogen column density as

$$N_{\mathrm{H,OH}} = \frac{a\lambda^3 I_{\mathrm{OH}}}{2k_B}, \tag{3.17}$$

where λ is the emission line wavelength, I_{OH} is the velocity-integrated intensity, and a is an empirical constant. For the two OH 18 cm lines, we have $a = 2.12 \times 10^{22}$ cm^{-2} / (K km s^{-1}) for the 1665 MHz line and $a = 1.18 \times 10^{22}$ cm^{-2} / (K km s^{-1}) for the 1667 MHz line, respectively (Troland & Crutcher 2008).

We again follow observational procedure in deriving the column density related to the H I absorption in each Gaussian component. For an isothermal cloud, the H I column density is related to the velocity-integrated optical depth by (e.g., Draine 2011)

$$N_{\mathrm{HI}} = \left(1.82 \times 10^{18} \frac{\mathrm{cm}^{-2}}{\mathrm{K\ km\ s^{-1}}}\right) T_{\mathrm{s,comp}} \int \tau_{\mathrm{comp},\nu}\, dV, \tag{3.18}$$

where $T_{\mathrm{s,comp}}$ is the spin temperature, and the integral is over the velocity range of the absorption spectrum. With the combination of the off-source emission spectrum T_{B} and the on-source absorption spectrum τ, we can determine $T_{\mathrm{s,comp}}$ as

$$T_{\mathrm{s,comp}} = \frac{T_{\mathrm{B,peak}}}{1 - \exp(-\tau_{\nu,\mathrm{peak}})}, \tag{3.19}$$

where the subscript *peak* indicates values measured at the center of the Gaussian component where the line-of-sight velocity $V_{\mathrm{LOS}} = V_{\mathrm{comp}}$. This gives column densities for the H I absorption against background radio source measurements.

Finally, since we did not produce synthetic spectra for the HINSA observations, we simply take the hydrogen column density in the form of H_2 as $N_{\mathrm{H,cold}}$; the approach matches that used in Ching et al. (2022), though in their case they derive the H_2 column from an independent estimate. In our case we take the H_2 column directly from the simulation data.

For consistent comparison with Crutcher (2012), we select H I synthetic beams with a converted column density $N_{\rm HI} \in (10^{19},\ 10^{21})$ cm^{-2}, and OH synthetic beams with a converted column density $N_{\rm H,OH} > 10^{21.5}$ cm^{-2}. In Figure 3.7 we show the median and 16th to 84th percentile range of measured magnetic field strength from synthetic H I absorption and OH measurements in bins of column density 0.25 dex wide; the blue band shows the former, the yellow band shows the latter. We also plot the 14 HINSA measurements toward the densest point in each synthetic map as individual red points. The dashed green line shows the sub- / super-critical transition, defined by

$$|B_{\rm LOS,crit}| = 3\pi\sqrt{\frac{G}{5}}\mu m_{\rm H} N_{\rm H}, \tag{3.20}$$

where $\mu = 1.4$ is the mean mass per H nucleon for gas with the usual composition of $\approx 75\%$ H and $\approx 25\%$ He by mass. Finally, we show the observations compiled by Crutcher (2012) as grey dots with error bars for comparison.

The primary point to take from Figure 3.7 is that our synthetic observations do an excellent job of reproducing the real observations. The median LOS field strength is ~ 1 μG for H I observations, and rises to ~ 10 μG for OH observations. We can also see a clear transition in magnetic criticality at column densities $N_{\rm H} \in (10^{21},\ 10^{22})$ cm^{-2}, such that the majority of the H I absorption measurements indicate sub-criticality, while the OH measurements are almost exclusively in the super-critical region. Again consistent with the result of Ching et al. (2022), most HINSA synthetic observations also lie in the super-critical region.

3.4.2 Gravitational versus magnetic energy

Although the synthetic Zeeman effect measurements agree with previous observational works, these may not reveal the true relation between gravitational energy E_g and magnetic energy E_B. To investigate these, we compute the total gravitational potential and magnetic energies within some volume of interest V as

$$E_g = -\frac{1}{2}\sum_p \sum_{q,q\neq p} \frac{G M_p M_q}{r_{pq}}, \tag{3.21}$$

$$E_B = \int_V \frac{B^2}{8\pi}\, dV. \tag{3.22}$$

In the equations above, G is the gravitational constant, p and q are indices that run over all the GIZMO particles within V, M_p and M_q are the particle masses, r_{pq} is the distance between particle p and particle q, and B is the local total magnetic field strength. We evaluate these energies as a function of size scale by identifying the

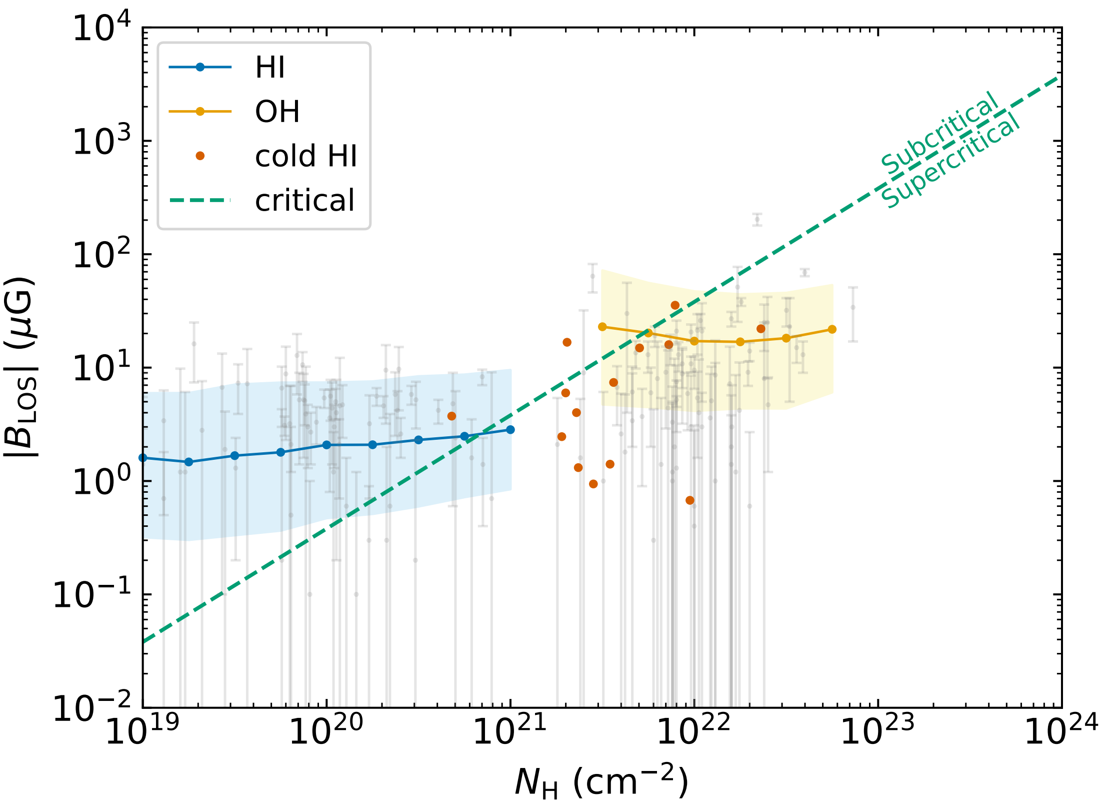

Figure 3.7: Magnetic field strengths inferred from synthetic Zeeman effect observations using H I absorption against background radio sources (blue band), OH emission (yellow band) and H I narrow self-absorption (red points), as a function of inferred column density. For the yellow and blue bands, lines with points show 50th percentile values of the $|B_{\rm LOS}|$ in bins of column density 0.25 dex wide, while the band edges illustrate the 16th to 84th percentile range. Grey points show real observations, from the compilation of Crutcher (2012). The green dashed line represents $\mu_B = 1$ (equation 3.20). Measurements below this line correspond to super-critical conditions, while those above are sub-critical.

densest gas particle in each of our seven sample clouds, then drawing four spheres with radii $r = 10, 25, 50$, and 100 pc. We choose these size scales to span the atomic-to-molecular transition that is, based on the observational diagnostics, closely related to the sub- / super-critical transition: for all seven samples, the H_2 mass fraction is ≈ 0.9 for $r < 10$ pc, but drops to around 0.3 for $90 < r < 100$ pc, indicating that our sample regions span from the molecular core to the cloud edge. The 50 pc sphere is also close in size to the 100 pc region onto which we interpolate onto a grid when computing the synthetic Zeeman effect, though we will see below that the synthetic observations are actually sensitive to considerably smaller scales than this.

In Figure 3.8 we plot the E_g/E_B versus sphere radius for all seven clouds. It is clear that $E_g/E_B > 1$ for all clouds on most scales. The only exception is cloud 1, which has $E_g/E_B \approx 0.6$ on $r = 25$ and 50 pc scales, which may be related to the fact that it has the smallest total mass in our sample; however, even these sub-critical regions are embedded within a larger 100 pc-scale super-critical one. Therefore, from the 3D information, we conclude that all seven clouds are already super-critical on scales where the H I synthetic observations seem to indicate that they are sub-critical. Using the full 3D information, we find no transition from a sub- to a super-critical state across the H I - H_2 transition. This suggests that the observed transition in magnetic criticality across the column density is most likely a result of inconsistency between 2D projected observations and real 3D structures. We explore the nature of this mismatch in the next section.

3.5 Discussion

We have seen that, although both actual Zeeman measurements and our synthetic versions of them indicate the existence of a transition between sub- and super-critical states as material transitions from H I to H_2, no such transition is actually found in our simulations; instead, even on 100 pc scales around giant molecular clouds where the mass is predominantly atomic, clouds are super-critical. Our goal in this discussion is to understand why the H I Zeeman observations seem to indicate the presence of a sub-critical state where none actually exists. We find that this sub-critical illusion has two contributing factors. First, in previous observational work, the column density N associated with a particular H I Zeeman measurement is directly converted from the observed absorption line depth, which measures only H I material, and misses other chemical states of gas. Second, Zeeman effect measurements only provide information on the magnetic field in regions of strong absorption (or emis-

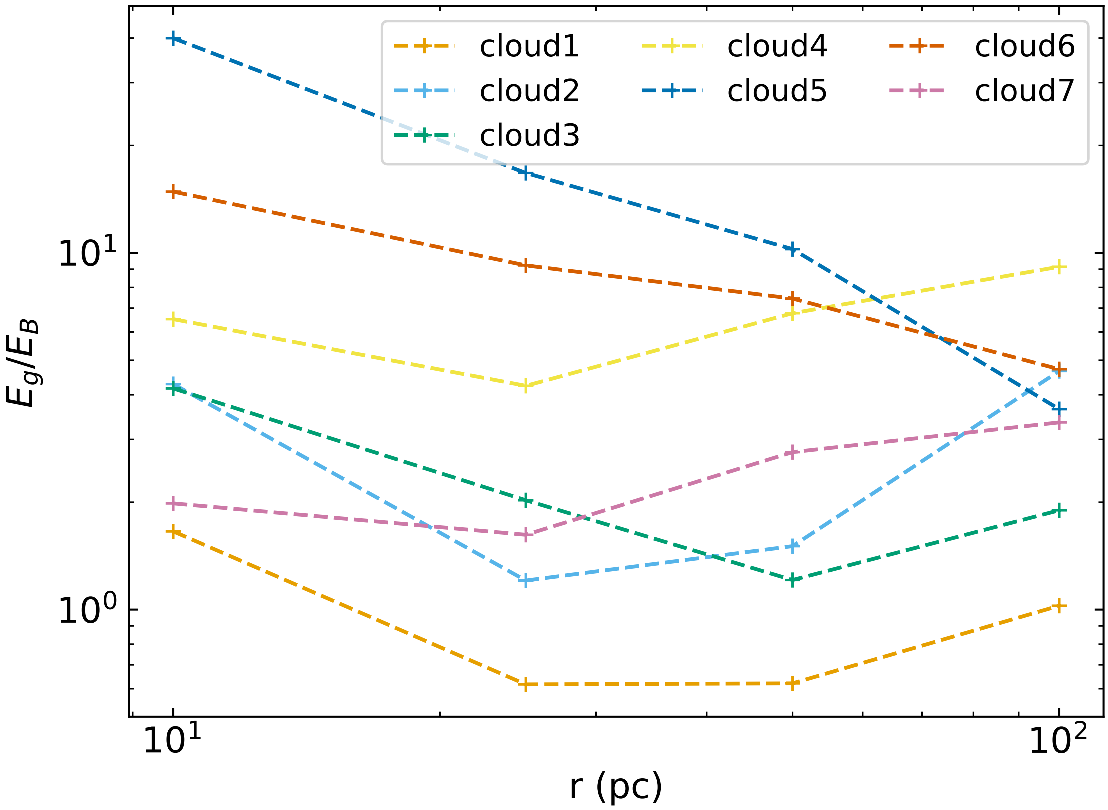

Figure 3.8: Ratios of gravitational energy E_g to magnetic energy E_B measured in spheres with different radii r, centred on the densest point in each sample cloud.

sion for OH), and such regions may not be representative of the true magnetic field strength, leading to a biased estimate of E_g/E_B.

Starting with the first of these factors, to study how accurate the $N_{\rm HI}$ synthetic measurement is, we compare it with results directly derived from the simulation data. For each Gaussian component for which we make a synthetic Zeeman measurement, we first find the related line of sight, then compute the density $n_{\rm HI}$ at positions along that LOS where the LOS gas velocity $V_{\rm LOS}$ lies in the range $V_{\rm comp} \pm \sigma_{v,\rm comp}$, i.e., we find all the fluid elements whose velocities lie within one standard deviation of the central velocity of each component. We then compute the column density $N_{\rm HI,1\sigma_v}$ of these fluid elements. We then define the intrinsic H I column density related to the Gaussian component as $N_{\rm HI,sim} = N_{\rm HI,1\sigma_v}/0.683$, where 0.683 is the fraction of the mass that lies within $\pm 1\sigma$ of the centre for a Gaussian distribution. We also use an identical procedure to derive the total hydrogen column density $N_{\rm H,sim}$ by projecting the total density of H nuclei $n_{\rm H}$; $N_{\rm H,sim}$ differs from $N_{\rm HI,sim}$ in that the former includes all hydrogen regardless of its chemical state, while the latter includes only hydrogen that is chemically in the form of H I.

We can compare these true column densities to the columns $N_{\rm HI}$ derived from the 21 cm spectra using observational methods, as described in Section 3.4.1, equation 3.15 and equation 3.19. The ratios $(N_{\rm HI}/N_{\rm HI,sim})$ and $(N_{\rm HI}/N_{\rm H,sim})$ then tell us how far the observational measurements lie from the H I mass and the total mass. In Figure 3.9 we plot the 16th, 50th and 84th percentiles of $(N_{\rm HI}/N_{\rm HI,sim})$ and $(N_{\rm HI}/N_{\rm H,sim})$, binning the data by observationally-estimated column density $N_{\rm HI}$ in the same pattern as in Figure 3.7. From the figure we can see that the observational procedure recovers about $\sim 40\%$ of H I mass, but only $\sim 10\%$ of the total mass. The reason is that most mass along the line of sight is in the form of H_2 and ionised hydrogen. In retrospect this result is not surprising: observational probes of H I around molecular clouds do not represent a randomly-selected sample of lines of sight through the ISM. Instead, they are probing regions where it is reasonable to believe that dark gas composed mostly of H_2 might exist. This result shows that observationally-inferred mass-to-flux ratios likely suffer from underestimates of $N_{\rm HI}$ due to chemical composition variations.

The second factor contributing to the inconsistency between the observed and true levels of magnetic criticality we identify in Section 3.4 is the limited spatial scale of the magnetic field probed by Zeeman effect measurements. From equation 3.15 we learn that $B_{\rm HI}$ measurements are dominated by regions with large absorption coefficients, which may only reveal only a small part of the overall magnetic field structure. To quantify this effect, we compute an effective length scale probed by

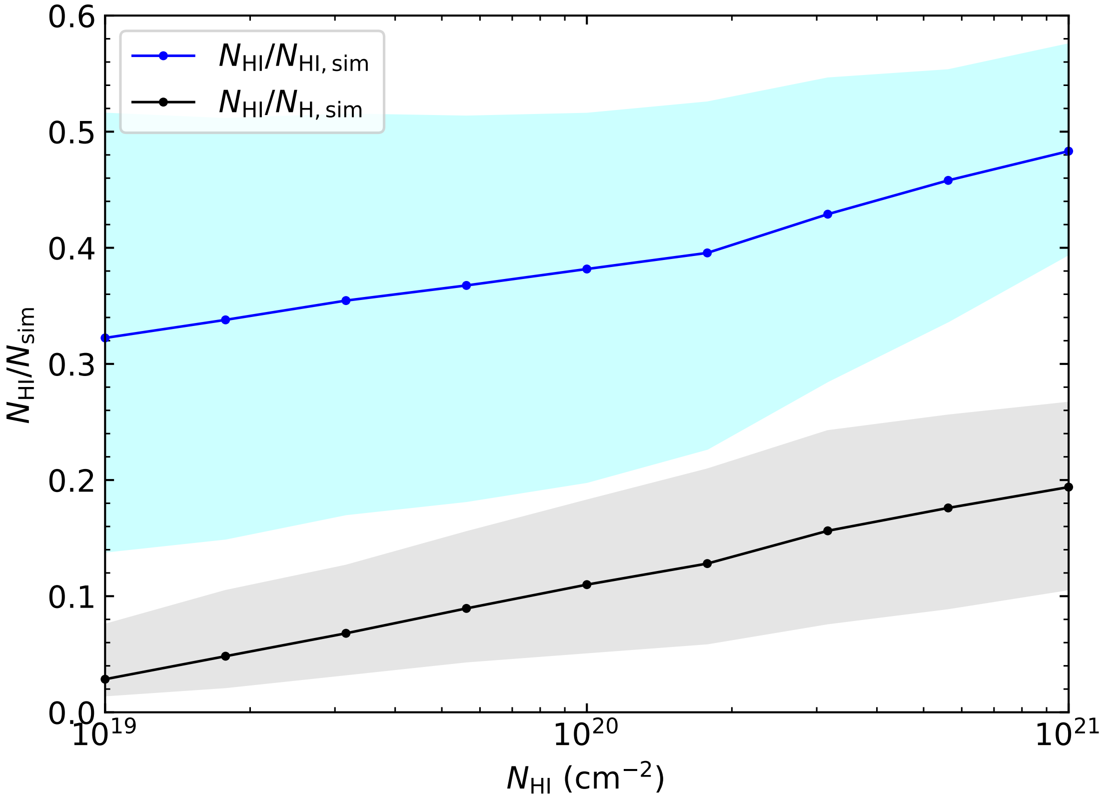

Figure 3.9: The blue band shows the ratio of inferred to true H I column density, ($N_{\rm HI}/N_{\rm HI,sim}$), while the grey band shows the ratio of inferred H I column density to true column density of H nuclei in all chemical states, ($N_{\rm HI}/N_{\rm H,sim}$). For each band, lines with dots show the 50th percentile values in bins of observationally-inferred H I column density $N_{\rm HI}$, while the band edges illustrate the 16th and 84th percentiles.

H I absorption measurements as follows. For each LOS, we assign the ith sample point on that LOS a position $x_i = i\Delta L$. We then define the length scale of H I the B-field measurement $l_{\rm HI}$ to be the weighted standard deviation of x_i, where the weight w_i is defined by that sample point's contribution to the synthetic Zeeman measurement, as defined in equation 3.14. Quantitatively, we compute $l_{\rm HI}$ as

$$x_{\rm mean} = \frac{\sum_i w_i x_i}{\sum_i w_i}, \tag{3.23}$$

$$l_{\rm HI} = \left[\frac{\sum_i w_i (x_i - x_{\rm mean})^2}{\sum_i w_i}\right]^{1/2}, \tag{3.24}$$

where the sum runs over all the sample points i along a given line of sight. Intuitively, $l_{\rm HI}$ calculated in this way quantifies the length along the line of sight of the region that contributes to a Zeeman measurement; for uniform w_i, given our 100 pc sampling region, $l_{\rm HI}$ equals 57.7 pc, while the smallest $l_{\rm HI}$ that we can resolve given our sampling, corresponding to a case where the region that produces the absorption is captured by exactly two sample points that both contribute equally, is 0.25 pc. Performing this calculation over all LOS's, we find that the 16th, 50th, and 84th percentiles of $l_{\rm HI}$ are 4.11 pc, 11.4 pc, and 29.3 pc, respectively. Therefore, our synthetic H I observations generally measure magnetic fields in regions of strong H I absorption whose characteristic size scale is ~ 10 pc. We have perform a similar calculation on OH emission as in equation 3.24, but we change the weight function to $L_{\rm OH}$, and derive the characteristic size scale of OH Zeeman effect measurement as ~ 3 pc.

To see why selecting H I-dominated regions of this size scale might produce a bias, for each (100 pc)^3 cube we identify all sample points where at least 75% of hydrogen atoms are in the form of H I; then we randomly select 20 such points that are at least 10 pc from each other, and draw $r = 10$ pc spheres around them. We determine the E_g/E_B ratio for these spheres, yielding a total of 140 samples – 20 from each of the seven sample clouds. For these samples we find a median $E_g/E_B = 0.25$, and the ratio is less than unity for 63% of them. This result indicates that $\sim$ 10-pc scale regions of H I-dominated gas *are* likely to be locally sub-critical, which is consistent with the observations of Heiles & Troland (2004) and others. However, this is an illusion created by sampling unrepresentative regions: when considering the whole cloud from which these H I regions are drawn on 100 pc scales, or when selecting regions centred on the density maximum rather than maxima of H I absorption, we find that the gas is super-critical, as shown in Figure 3.8.

This analysis leads us to propose a scenario for the relation between gravity and magnetic fields in molecular clouds and their neutral hydrogen surroundings illustrated in Figure 3.10. For a cloud $\sim$ 100 pc in size, its dense molecular core is super-critical, and is revealed as such when it is measured using OH emission lines. Small H I sub-regions in the cloud outskirts are generally locally sub-critical, in the sense that their magnetic energy is larger than their gravitational *self*-energy, consistent with the H I absorption observations. However, even for regions that are genuinely sub-critical on $\sim$ 10 pc scales, if we consider the large scale cloud structure as a whole, the molecular mass ignored in H I observations can greatly increase the total gravitational energy and make the whole cloud super-critical. Magnetic fields may be able to locally support H I regions against gravity, but cannot resist gravitational collapse on the large scale. One can make a useful analogy here to the competition between thermal and gravitational energy in the envelope of the Sun – if one considers only the outer layers of the Sun, say the outer half in radius, its thermal energy is far greater than its gravitational binding energy. However, this is a misleading statistic, because the dominant source of gravitational binding for the outer 20% of the Sun is not its self-energy, but instead the gravitational attraction provided by the remaining 80% of the mass. A measurement that is *only* sensitive to the ratio of thermal to gravitational energy in the envelope will completely miss this effect.

In this view, the apparent transition between sub-critical and super-critical gas seen in Zeeman measurements, and described in Crutcher (2012), is a confusion caused by mixing local and cloud-scale energy relations. Correct recovery of the level of magnetic criticality requires the ability to measure both the magnetic field and the true column across a whole molecular cloud. Previous Zeeman measurements do not provide this ability. Other two main magnetic field measurement techniques, like the Davis-Chandrasekhar-Fermi (DCF) method and the Faraday Rotation method, estimate B-field strengths from polarization observations. B-field strengths measured with these techniques are integrated along the line of sight, thus may also carry the bias introduced by non-uniform B-field and mass distribution. Therefore, with current observational results, the discussion of whether a region is sub- or super-critical is only meaningful for isolated, point-like sources, which in most cases are gravity-dominated cores. If one wants to accurately evaluate importance of B-field relative to gravity on 10 to 100 pc scale, it is necessary to measure B-field strengths throughout the whole interested region, like data points in a Position-Position-Velocity (PPV) cube. Such work is only possible with high resolution Zeeman effect observations performed by advanced facilities like FAST, better if multiple tracers are used.

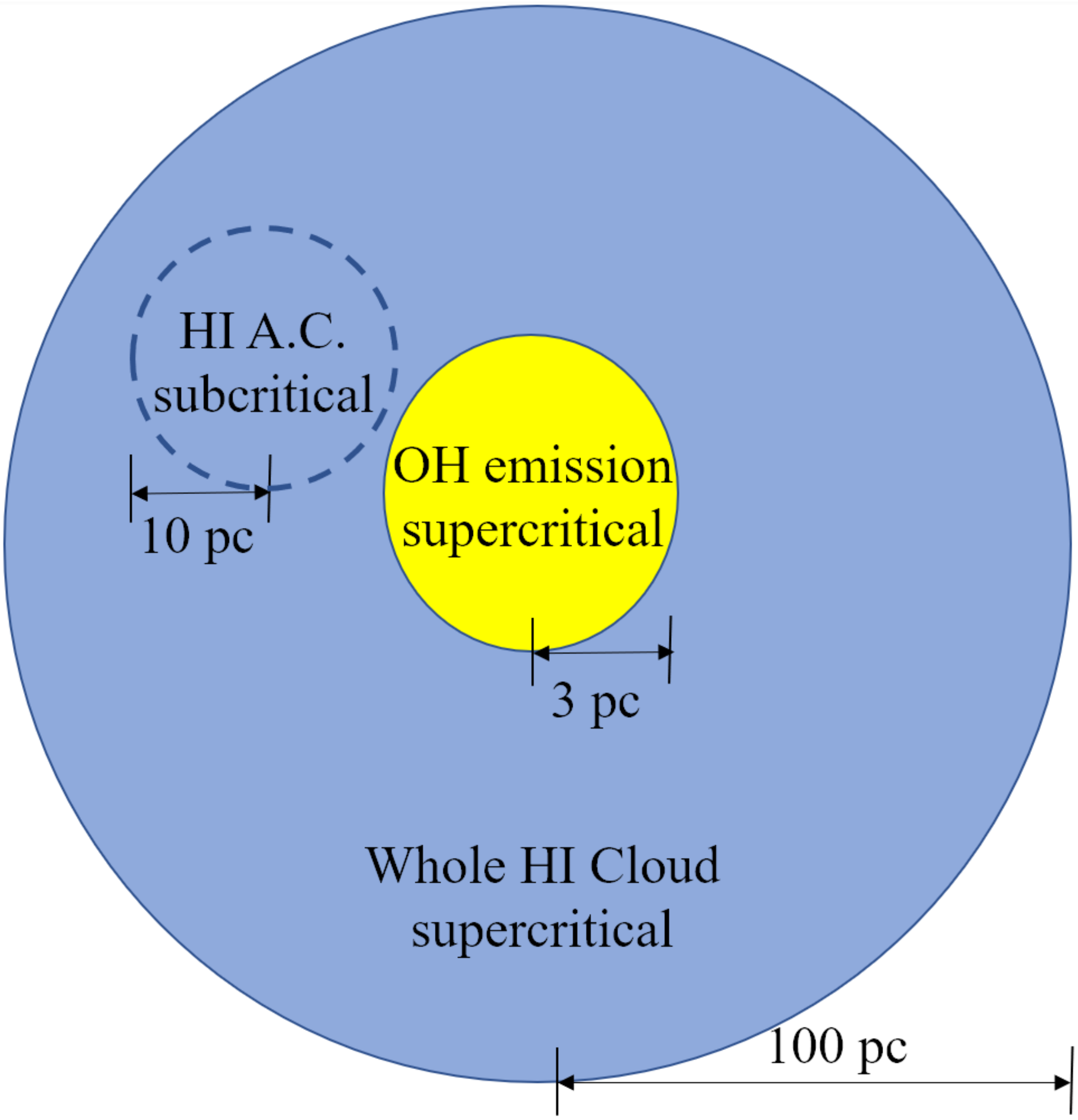

Figure 3.10: Schematic view of regions detected by Zeeman effect observation in the H I cloud. The dashed circle labeled as H I A.C. is the H I sub-region measured by an absorption component (A.C.) in observation. Note that the length scale of different regions is not strictly proportional.

3.6 Conclusions

This work aims at understanding the apparent transition in magnetic criticality between H I- and H_2-dominated regions found in Zeeman effect observations. Such study requires a combination of high-resolution simulations of the molecular cloud formation process and synthetic observations that capture the complexities of Zeeman measurements in different chemical tracers, following real observational procedures as closely as possible. To this end, we perform the first MHD simulation of molecular cloud formation out of realistic full-galactic magnetic field structure. Starting from the low-resolution galactic simulation, we zoom into 7 molecular clouds, then trace and re-simulate their formation history at high resolution (~ 0.4 pc). We then post-process the simulations to derive realistic chemical compositions, gas temperatures, and non-LTE level populations, yielding physically accurate calculations of emissivities and absorption coefficients in the most commonly-used Zeeman-sensitive lines. We use these to solve the radiative transfer equation along 100-parsec-long lines of sight to produce synthetic H I 21 cm line absorption and emission spectra, which mimic the absorption / emission strategy used in real H I Zeeman measurements, as well as synthetic OH emission and H I narrow self-absorption (HINSA) observations. We process these results using the same procedures used in observations to produce realistic synthetic measurements of magnetic field strengths and column densities in different tracers.

We find that our synthetic B vs. N relations are quantitatively consistent with the observed trends summarised by Crutcher (2012): molecular clouds appear to be sub-critical in H I observations, and become super-critical in OH observations; the transition of criticality happens in the hydrogen column density range of $N_{\rm H} \in [10^{21}, 10^{22}]$ cm^{-2}. HINSA measurements probe this column density regime, and generally indicate that clouds are super-critical.

Such results, however, may not reveal the real ratio between gravitational energy and magnetic energy E_g/E_B. We compare out synthetic Zeeman measures to ratios of E_g/E_B computed directly from the 3D simulation data, evaluated over a range of size scales and for a sample of different molecular clouds. On scales from 10 pc to 100 pc we find that the real ratio $E_g/E_B > 1$ for most clouds, which indicates that gravity dominates over magnetic fields. This applies even when averaging over size scales large enough that the material we are probing is largely atomic, indicating that the H I Zeeman observations do not accurately reflect the true dynamical state of the gas.

We identify two main contributors to this inconsistency. First, column densities used in H I Zeeman observations only measures the hydrogen mass in the neutral atomic form, which underestimates the true total column density along lines of sight where the chemical composition is not uniformly atomic hydrogen. Second, the regions probed by H I absorption Zeeman measurements capture density and magnetic field structure in ~ 10 pc-scale regions on the outskirts of molecular clouds. Although these local H I sub-regions may be sub-critical as observed, they are nonetheless part of larger structures that are still super-critical once we include the gravitational influence of the central dense molecular region. We conclude that accurate observational determination of the relative importance of magnetic fields and gravity in the molecular cloud formation process requires careful attention to ensure that the observations accurately capture all the self-gravitating mass, and that the regions captured by observations are representative of entire clouds, rather than small sub-regions within them.

Acknowledgements

The authors acknowledge Prof. Di Li, Dr. Tao-chung Ching, and Dr. Hiep Nguyen for suggestions on synthetic observations. We further acknowledge funding from the Australian Research Council through its Future Fellowship and Laureate Fellowship funding schemes, awards FT180100375 and FL220100020, and high-performance computing resources provided by the Australian National Computational Infrastructure (grants jh2 and ek9) through the National and ANU Computational Merit Allocation Schemes, and by the Leibniz Rechenzentrum and the Gauss Centre for Supercomputing (grant pr32lo).

Data Availability

The data underlying this article will be shared upon reasonable request to the corresponding author.

Chapter 4

On the limitations of Hα luminosity as a star formation tracer in spatially resolved observations

Context and Contribution

This chapter has been previously published as On the limitations of Hα luminosity as a star formation tracer in spatially resolved observations, by **Zipeng Hu, Benjamin D. Wibking, Mark R. Krumholz, and Christoph Federrath, 2024, MNRAS, stae2241**. *The work presented here is slightly modified from the published version. I have performed the simulations, produced the synthetic observations, and analyzed the data. I have written the majority of the paper, with inputs and suggestions from co-authors.*

Abstract

This study examines the limitations of Hα luminosity as a tracer of star formation rates (SFR) in spatially resolved observations. We carry out high-resolution simulations of a Milky Way-like galaxy including both supernova and photoionization feedback, and from these we generate synthetic Hα emission maps that we compare to maps of the true distribution of young stellar objects (YSOs) on scales from whole-galaxy to individual molecular clouds ($\lesssim$ 100 pc). Our results reveal significant spatial mismatches between Hα and true YSO maps on sub-100 pc scales, primarily due to ionizing photon leakage, with a secondary contribution from young stars drifting away from their parent molecular clouds. On small scales these effects contribute significantly to the observed anti-correlation between gas and star formation, such that there is $\sim$ 50% less anti-correlation if we replace an Hα-based star formation map with a YSO-based one; this in turn implies that previous stud-

ies have underestimated the time it takes for young stars to disperse their parent molecular clouds. However, these effects are limited in dense regions with hydrogen columns $N_{\mathrm{H}} > 3 \times 10^{21}$ cm^{-2}, where the Hα- and YSO-based SFR maps show better agreement. Based on this finding we propose a calibration model that can precisely measure the SFR of large molecular clouds (mean radius ¿ 100 pc) with a combination of Hα and CO observations, which provides a foundation for future study of star formation processes in extragalactic molecular clouds.

4.1 Introduction

The Hα emission line produced by hydrogen recombination is one of the most commonly used tracers for star formation, since it is emitted by the photoionized gas created by extreme ultraviolet photons from young massive stars. Observers routinely use this line to measure star formation rates (SFRs) for galaxies out to redshift $z \sim 2.5$, and on scales from whole-galaxy to kpc (e.g., Kennicutt 1983; Shivaei et al. 2015; Ellison et al. 2017; Belfiore et al. 2018). There are two major advantages of this method: first, the Hα line is easy to observe due to its brightness and location in the optical part of the spectrum, and because hydrogen is ubiquitous throughout the Universe; second, compared with other SFR tracers as the dust-reprocessed IR and UV continuum, Hα traces only the most recent star formation (< 5 Myr) due to the short lifetimes of the stars that produce the bulk of the Hα flux and the short recombination times of H II regions (e.g., Weisz et al. 2012; Caplar & Tacchella 2019; Haydon et al. 2020).

Driven in part by the success of Hα-based galactic-scale SFR measurements, there has been great interest of extending such studies to the smaller scales characteristic of individual molecular clouds, $\lesssim 100$ pc. Measurements on such small scales are important for testing star formation theories under different conditions, and have been used to measure quantities such as the characteristic lifetimes of molecular clouds and the strength of stellar feedback (e.g., Kruijssen & Longmore 2014; Kruijssen et al. 2018; Chevance et al. 2020; Chevance et al. 2021). Of all star formation tracers that are bright enough for routine use in extragalactic measurements, Hα is the only one that traces star formation on time scales similar to cloud life times, which can be as short as ~ 10 Myr (Chevance et al. 2023, and references therein). However, systematic uncertainties arise when converting Hα luminosity into SFR on local regions around molecular clouds. The first uncertainty source is the dust attenuation effect, which can cause significant underestimation of local SFRs in regions of high extinction. However, as long as the extinction is not too severe, this effect can be calibrated out using the ratios of Balmer recombination lines (the Balmer decrement method) on both galactic and cloud scales (e.g., Sánchez et al. 2012). The second problem is the stochasticity of massive star formation. In a $\lesssim 100$ pc region the SFR may be too small to sample all stellar masses and evolutionary states, which most often leads to underestimation of the SFR derived from the Hα tracer (da Silva et al. 2014; Gregg et al. 2024). The third and to date most poorly-calibrated bias depends on the size of H II regions. As summarized in Kennicutt & Evans (2012), such regions vary in scale from < 100 pc in the Milky way to $200-500$ pc in actively star-forming galaxies, implying that Hα-bright H II region boundaries may be displaced away from the original star-forming sites. This effect is further complicated by non-uniform gas distributions around newborn stars, which allows ionizing photons to travel farther in directions with less gas and thus make the bias anisotropic (Jin et al. 2022).

There have been limited efforts to characterise and calibrate the effects of stochasticity and finite H II region size. Observationally, one can compare Hα to direct counts of newborn stars, or young stellar objects (YSOs), identified from IR observations. However, beyond the Milky Way such efforts are severely limited by resolution. To date the only published extragalactic comparison of these tracers is from the Large Magellanic Cloud (Ochsendorf et al. 2017), and analysis of these data together with comparable Galactic data sets indicates significant disagreements on cloud scales (Krumholz et al. 2019).

This situation leaves simulations as the best available tool for understanding the spatial scales on which the SFR traced by Hα begins to deviate from the true star formation rate as characterised by direct counts of YSOs, and for quantifying the size of the discrepancy. Although no theoretical effort has been made thus far to study this question, there have been several numerical works that try to calibrate other aspects of Hα emission as a star formation tracer. Tacchella et al. (2022) use simulations of Milky Way-like and dwarf galaxies to study the effect of dust attenuation and calibrate the relation between Hα luminosity and SFR accounting for it, while Flores Velázquez et al. (2020) have estimated the time scales to which different SFR tracers are sensitive with cosmological simulations. However, such galactic scale models generally do not reach spatial resolutions of parsecs, or mass resolutions $\lesssim 100\ \mathrm{M}_\odot$, and thus can not resolve the star formation histories of individual molecular clouds. Kiloparsec-scale galactic box simulations with periodic boundaries can reach such resolutions (e.g., Peters et al. 2017; Kado-Fong et al. 2020), but lack a realistic large-scale galactic environment, which may affect molecular cloud density and spatial structure and ionizing photon transmission. For obvious reasons, they can not be used to study the reliability of Hα over a full range of scales from galactic to sub-kpc.

In this work, we perform high resolution MHD simulations to address these challenges. We start from a moderate resolution Milky-Way like spiral galaxy simulation to create a realistic galactic environment for molecular cloud evolution that we run to statistical steady-state, then increase the mass resolution and continue the simulation for a shorter period to resolve the structures on parsec scales. Our star formation algorithm stochastically draws stars from the initial mass function (IMF), traces the individual stellar evolution to calculate the feedback, and directly follows the propagation of ionizing photons through the galaxy using a Strömgren volume method. Via post-processing, we derive local chemical compositions, and generate synthetic CO, Hα, and YSO observations. Our goal is to answer the following questions: on what scales do star formation rates inferred from Hα agree reasonably well with those inferred directly from YSOs? On scales where agreement breaks down, what are the physical mechanisms responsible? And can we calibrate the Hα tracer to the YSO tracer to allow more accurate mesurements on the scales of individual molecular clouds?

The present paper is organized as follows: Section 4.2 summarizes the numerical method and simulation setup, then outlines the synthetic observation generation method. Section 4.3 compares our synthetic Hα observation with observations of real galaxies in order to validate our methods, and presents scale-dependent comparisons of star formation rates inferred by Hα versus by direct YSO counting. Section 4.4 discusses the physical mechanisms behind the difference, develops a calibration method, and proposes possible future work in this area. Section 4.5 concludes the work done in this paper.

4.2 Methods

We describe in Section 4.2.1 our Milky-Way like galaxy simulation, and list basic physical parameters of the simulated galaxy. We also describe the underlying physics and numerical methods. Then in Section 4.2.2 we introduce our method to produce synthetic SFR measurements traced by both Hα luminosity and YSO counts.

4.2.1 Simulations

Our galactic scale simulation is designed based on the whole-galaxy simulations by Wibking & Krumholz (2023, hereafter WK22) and Hu et al. (2023, hereafter HWK23). The simulation code we use is GIZMO (Hopkins 2015; Hopkins & Raives

2016; Hopkins 2016), which adopts a mesh-free, Lagrangian finite-mass Godunov method to solve the equations of magneto-hydrodynamics (MHD). The simulation include a time-dependent chemistry network that tracks the abundances of H I, H II, He I , He II , and He III , and uses these abundances to calculate hydrogen and helium cooling rates. It also includes metal line cooling computed by interpolating on a set of pre-computed CLOUDY (Ferland et al. 1998) tables assuming Solar metallicity and collisional ionization equilibrium, and as implemented by the GRACKLE chemistry and cooling library (Smith et al. 2017). We implement algorithms for star formation, stellar feedback, and radiative cooling in the same way as in HWK23. Here we provide a brief summary of the physics and numerical methods most relevant to this project, and refer the readers to HWK23 and WK22 for more details.

For every gas particle with a density $\rho_{\rm g}$ above a prescribed threshold $\rho_{\rm crit}$, we determine its local SFR density as

$$\rho_{\rm SFR} = \epsilon_{\rm ff}\frac{\rho_{\rm g}}{t_{\rm ff}}, \tag{4.1}$$

where $\epsilon_{\rm ff}$ is the star formation efficiency, and $t_{\rm ff}$ is the local gas free-fall time. Multiple observational methods across a wide density range yield a mean value of $\epsilon_{\rm ff} \approx 0.01$ (Krumholz et al. 2019), with a dispersion about 0.2 dex in the Milky Way (Hu et al. 2022). Therefore we adopt $\epsilon_{\rm ff} = 0.01$ in equation 4.1. The star formation density threshold we apply in our simulation is $\rho_{\rm crit} = 1000\ {\rm m_H\ cm^{-3}}$, chosen to produce approximate equality between the Jeans mass and the particle mass at our peak gas mass resolution $\Delta M = 89\ {\rm M_\odot}$ (see below). To avoid extremely small time steps in high density region, and the resulting high computational cost, we increase $\epsilon_{\rm ff}$ to 1 for gas particles with $\rho_{\rm g} > 100\rho_{\rm crit}$. In this way, we quickly convert high density gas particles into stellar particles, and set the highest density we resolve in this simulation to approximately $100\rho_{\rm crit}$. During one time step Δt, gas particles with $\rho_{\rm SFR} > 0$ have a probability

$$P = 1 - \exp(-\epsilon_{\rm ff}\Delta t/t_{\rm ff}) \tag{4.2}$$

of being converted to a stellar particle. Once formed, the stellar particles represent sub-clusters that only interact with the galactic environment via gravity and stellar feedback.

When calculating the stellar feedback, we cannot integrate over the IMF because our stellar particles are too small: at our mass resolution, the expected number of SNe per particle is $\lesssim 1$, and the expected number of stars $\gtrsim 20\ {\rm M_\odot}$ – the mass range that dominates ionizing photon production – is $\ll 1$. Instead, for each stellar particle, we use the stellar population synthesis code SLUG (da Silva et al. 2012;

Krumholz et al. 2015) to stochastically draw its stellar population from a Chabrier IMF (Chabrier 2005). In this simulation we only include photonionization and type II supernova feedback, since they are the dominant mechanisms at the scale with which we are concerned. At each hydrodynamical time-step, SLUG reports for each star particle the instantaneous ionizing luminosity, $\dot{N}_{\rm ion}$, the number of individual type II supernovae, $N_{\rm SNe}$, and the mass of the ejecta, $M_{\rm ej}$, added during that time step; we derive the ionizing luminosities from a combination of Padova stellar tracks (Schaller et al. 1992; Meynet et al. 1994; Girardi et al. 2000) and SLUG's "starburst99" treatment of stellar atmospheres (Leitherer et al. 1999), and draw our estimates of which stars end their lives in type II SNe, and the ejecta mass for those that do, from the tabulated results provided by Sukhbold et al. (2016). Assuming each supernovae ejects an equal energy of 10^{51} erg, we can easily derive the energy of the ejecta as $E_{\rm ej} = N_{\rm SNe} \times 10^{51}$ erg, and the momentum as $p_{\rm ej} = \sqrt{2E_{\rm ej}M_{\rm ej}}$. Then for type II supernovae feedback, we inject the ejected mass, momentum, and energy into the neighbouring gas particles proportional to the solid angle centered on the stellar particle and subtended by the effective intersection area between each nearby gas particle and the star, following the approach described in Hopkins et al. (2018a,b). As for the implementation of photonionization, we adopt the algorithm as in Hopkins et al. (2018a): for each star particle, we sort its nearby gas particles with increasing distance, and start from the first gas particle that has a temperature below 10^4 K, which we define as non-ionized. We then calculate the ionization rate $\Delta\dot{N}_{\rm ion}$ needed to fully ionize it, set the temperature of this gas particle to 10^4 K, and deduct $\Delta\dot{N}_{\rm ion}$ from $\dot{N}_{\rm ion}$. We repeat this process on the next closest non-ionized gas particle until $\dot{N}_{\rm ion} \approx 0$.

The initial conditions and set up of our simulation follow the same routine as described in HWK23. Following that paper, we initially run the simulation for 0.7 Gyr at a mass resolution of $\Delta M = 859.3$ $\mathrm{M}_\odot$. During this period the galaxy reaches a stable SFR close to 3 $\mathrm{M}_\odot$ yr^{-1}. We then increase the mass resolution by a factor of 10. To do so, we replace each gas particle with 10 smaller particles randomly distributed around their parent particle's center of mass, with a distance of one fifth of the parental smoothing length. After the split, the child particle mass is divided by 10, the child smoothing length is divided by $10^{1/3}$, while all other physical parameters remain the same. In this way we improve the mass resolution to about 90 $\mathrm{M}_\odot$; as noted above, for our cooling curve this is approximately equal to the Jeans mass at our star formation threshold, and the corresponding Jeans length is ≈ 1 pc, which we take to be the characteristic resolution of our simulation. This split snapshot becomes the initial condition for the next stage of our simulation, which we run for 23 Myr, which is about 4 times of the maximum age of massive stars that can emit ionizing photons (~ 5 Myr) and thus is long enough for the ionization pattern to reach a steady state at the new resolution. During this phase we output snapshots at a 1 Myr frequency. We show the face-on gas column density map $N_{\rm H}$ at 720 Myr (i.e., 20 Myr into the high resolution run) in the upper left panel of Figure 4.1.

4.2.2 Synthetic observation

In order to study the difference between SFR measurements derived from Hα and those using direct star counts, we need to produce two different synthetic maps from our simulation: a YSO mass distribution map and an Hα luminosity map. In addition, we also produce a synthetic CO emission map, for comparison with real extragalactic molecular cloud observations.

Due to their different evolution stages and spectral energy distributions, protostars identified from IR observations are normally classified into two types (e.g., Evans et al. 2009; Carney et al. 2016; Pokhrel et al. 2020): class 1 YSOs are embedded in a circumstellar envelope, and have a smaller age limit ($\lesssim 0.5$ Myr), while class 2 YSOs are surrounded by an optically thick circumstellar disk but not an opaque envelope, and have a larger age limit (< 2 Myr). We elect to use a 2 Myr age limit to define YSOs for our analysis, both for consistency with existing extragalactic observational analyses (Ochsendorf et al. 2017) and to reduce the shot noise that arises from the finite number of star particles in our simulation, which is limited by our mass resolution. To construct our YSO map, we identify all stellar particles formed in the 2 Myr prior to the time of a given snapshot as YSOs, and project their masses along the z-axis (normal to the galactic plane) onto a 2D histogram to produce the YSO mass distribution map; we defer for the moment a discussion of the pixel size we use in these maps. The SFR per unit area inside each pixel can be simply calculated as

$$\Sigma_{\rm SFR,YSO} = \frac{\sum m_{\rm YSO,pix}}{\Delta A_{\rm pix}\Delta t_{\rm YSO}}, \tag{4.3}$$

where $m_{\rm YSO,pix}$ is the total mass of YSOs inside a given pixel, $\Delta A_{\rm pix}$ is the pixel area, and $\Delta t_{\rm YSO} = 2$ Myr is the age range over which we identify YSOs. We plot the map of $\Sigma_{\rm SFR,YSO}$ in the lower right panel of Figure 4.1, which illustrates the intrinsic spatial distribution of SFR in our simulated galaxy.

To construct the Hα luminosity map, we first compute the case B Hα emission coefficient from the approximation suggested by Draine (2011),

$$\alpha_{\rm eff,H\alpha} \approx 1.17 \times 10^{-13} T_4^{-0.942-0.031\,\ln(T_4)} {\rm cm^3 s^{-1}}, \tag{4.4}$$

where T_4 is the ratio between the gas temperature T and 10^4 K. Since we trace the abundances of hydrogen and helium atoms and ions in our simulation, we can easily derive the local number density of protons $n_\mathrm{p} = n_\mathrm{HII}$ and electrons $n_\mathrm{e} = n_\mathrm{HII} + n_\mathrm{HeII} + 2n_\mathrm{HeIII}$.[1] Then we can derive the total Hα luminosity from each gas particle simply as

$$L_{\mathrm{H}\alpha} = \alpha_{\mathrm{eff,H}\alpha} h\nu_\alpha n_\mathrm{e} n_\mathrm{p} V, \quad (4.5)$$

where $\nu_\alpha = 457$ THz is the frequency of the Hα emission line, and V is the effective volume of the gas particle. Since equation 4.4 is no longer a good approximation for low temperature regions, We discard $L_{\mathrm{H}\alpha}$ from gas particles with $T < 1000$ K. We also ignore $L_{\mathrm{H}\alpha}$ for gas particles with $\rho > 10\rho_\mathrm{crit}$, since we are modifying the physics at these densities with our star formation algorithm and thus the particle properties are unreliable. To convert $L_{\mathrm{H}\alpha}$ to SFR, we consider a slightly modified version of the fit provided by Kennicutt & Evans (2012), who find a relationship

$$\log \mathrm{SFR}(\mathrm{M}_\odot\,\mathrm{yr}^{-1}) = \log L_{\mathrm{H}\alpha}(\mathrm{erg\,s}^{-1}) - C_{\mathrm{H}\alpha}, \quad (4.6)$$

where $C_{\mathrm{H}\alpha} = 41.27$ is the calibration parameter. This calibration includes the effects of dust scattering and attenuation, both external and internal to H II regions (i.e., the fact that not every ionizing photon is absorbed by a hydrogen atom), which are not included in our simulation and post-analysis; it is also at least somewhat dependent on the choice of IMF and stellar evolution tracks to atmospheres. To ensure consistency, we therefore determine a different calibration factor as follows: for all snapshots past the first 3 Myr (during which time the high resolution simulation is still settling), we calculate both the total $L_{\mathrm{H}\alpha}$ and the total star formation rate traced by YSOs with ages < 2 Myr over the whole simulation domain, and set our value of $C_{\mathrm{H}\alpha}$ so that the star formation rates from Hα and YSO counts agree when averaged over these snapshots. The resulting value is $C_{\mathrm{H}\alpha} = 40.67$, a factor of ≈ 3 smaller than the Kennicutt & Evans (2012) value, which is consistent with the lack of dust attenuation in our simulations being the principle difference. We adopt this value throughout our analysis. We use this calibration to compute the Hα-derived star formation rate of every gas particle, and project the star formation rate converted from Hα luminosity $\mathrm{SFR}_{\mathrm{H}\alpha}$ along the z axis. We show a sample SFR surface density map from the 720 Myr snapshot in the lower left panel of Figure 4.1.

[1] A minor technical issue is that, due to the difference between the time steps of GIZMO and GRACKLE, the chemical abundance of gas particles is not always updated to include the effects of photoionization when GIZMO writes out a snapshot. This results in a small number of particles that have been ionized by the photoionization algorithm and whose temperatures have therefore been set to 10^4 K, but whose H II abundances have not yet been updated. To handle these cases we treat all gas particles with $T \geq 10^4$ K as fully ionized in hydrogen, consistent with our photonionzation feedback algorithm.

The last mock observation we produce is the synthetic CO emission map, which is the most commonly used tracer of molecular mass. Our approach to this map is similar to that in HWK23, so here we provide only a brief summary. While it is possible to include chemistry on the fly in simulations (e.g., Glover et al. 2010; Tritsis et al. 2022), this is computationally intensive, and also does not by itself capture non-LTE excitation effects, which are equally important for predicting observable emission. For this reason, we instead use the DESPOTIC astrochemistry and radiative transfer code (Krumholz 2014a) to post-process the output snapshots. Under the assumption of Solar elemental abundances and Solar radiation field environment, DESPOTIC uses an escape probability approximation to derive the CO $J = 1 \to 0$ emission line luminosity per hydrogen atom l_{CO} ($\nu_{\mathrm{CO}} = 115.271$ GHz) as a function of three local physical parameters: hydrogen atom number density n_{H}, column density N_{H}, and velocity gradient $\mathrm{d}v/\mathrm{d}r$. We first run DESPOTIC on a grid covering the parameter range $n_{\mathrm{H}} = 10^{-2} - 10^{6}$ cm^{-3}, $N_{\mathrm{H}} = 10^{19} - 10^{25}$ cm^{-2}, and $dv/dr = 10^{-3} - 10^{2}$ km/s/pc. The result is a table of l_{CO} versus $(n_{\mathrm{H}}, N_{\mathrm{H}}, \mathrm{d}v/\mathrm{d}r)$; we determine l_{CO} values for each gas particle by performing trilinear interpolation on this table. We take values of n_{H} and $\mathrm{d}v/\mathrm{d}r$ for each cell directly from GIZMO output, while we derive N_{H} from the N_{H} value at the gas particle position in the column density map. Then we can derive the total CO $J = 1 \to 0$ emission line luminosity as $L_{\mathrm{CO}} = X_{\mathrm{H}} m_{\mathrm{g}} l_{\mathrm{CO}} / m_{\mathrm{H}}$, where $X_{\mathrm{H}} = 0.76$ is the hydrogen mass fraction, and m_{g} is the gas particle mass. We set $L_{\mathrm{CO}} = 0$ for gas particles with ionized mass ratio $X_{\mathrm{HII}} > 10\%$; this is necessary because our DESPOTIC grid does not include the effects of photoionization. We refer the readers to HWK23 and Krumholz (2014a) for more details. To facilitate comparison to observations, we convert L_{CO} into the CO-inferred molecular hydrogen mass as $m_{\mathrm{H_2,CO}}/\mathrm{M_\odot} = 2.3 \times 10^{-29} L_{\mathrm{CO}}/(\mathrm{erg\,s^{-1}})$; this conversion factor combines the CO $J = 1 \to 0$ line-luminosity conversion factor from Solomon & Vanden Bout (2005) and the mass-to-luminosity conversion factor from Bolatto et al. (2013). The resulting face-on synthetic $\Sigma_{\mathrm{H_2,CO}}$ surface density map for the 720 Myr snapshot is plotted on the upper right panel in Figure 4.1.

4.3 Results

In this section, we first demonstrate that the spatial distribution of our synthetic Hα luminosity map is similar to what is found in real observed galaxies by producing the so-called tuning fork diagram (Section 4.3.1). Then we illustrate and quantify the differences between the SFR measurements traced by Hα and YSOs as a function of scale (Section 4.3.2).

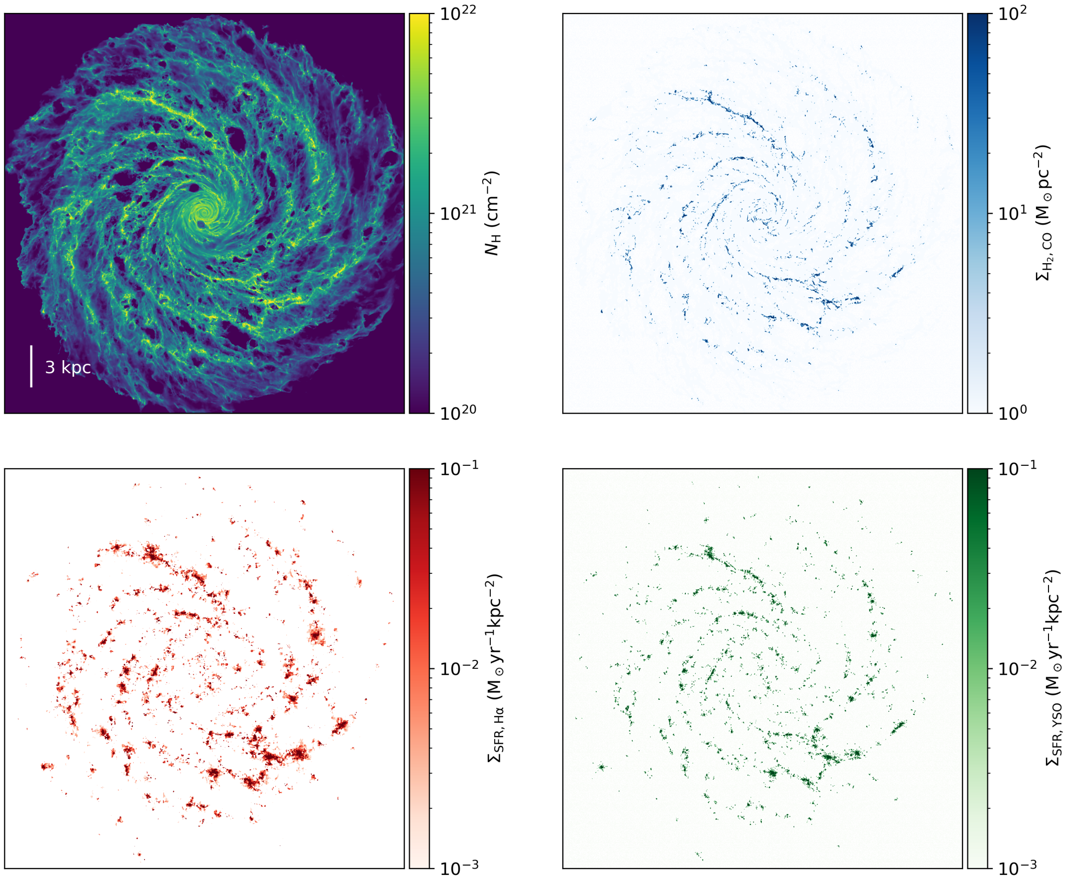

Figure 4.1: Milky-Way-like spiral galaxy simulation at 720 Myr. Upper left panel: total gas column density map; here $N_{\rm H}$ is the column density of H nuclei, regardless of their chemical state. Upper right panel: surface density map of molecular mass as traced by CO $J = 1 \rightarrow 0$ emission (see main text for details). Lower left panel: SFR surface density map traced by Hα emission. Lower right panel: SFR surface density map traced by YSOs with ages below 2 Myr. The dimensions of each map are 30×30 kpc, while the pixel size of each map is 20 pc. The ruler in the upper left panel indicates 3 kpc.

4.3.1 Tuning fork diagram

To test the reliability of our stellar feedback mechanisms and the resulting synthetic Hα maps, especially on spatial scales of molecular clouds (< 100 pc), we need to demonstrate that our simulations are capable of reproducing the spatial decorrelation between Hα emission peaks and molecular clouds that has been recently observed in a sample of nearby galaxies (Kruijssen et al. 2018; Kruijssen et al. 2019; Chevance et al. 2020; Chevance et al. 2021; Kim et al. 2022). Reproducing this decorrelation has proven to be an exquisively sensitive test of feedback implementations in galaxy simulation codes (e.g., Fujimoto et al. 2019; Semenov et al. 2021; Jeffreson et al. 2021b, 2024).

Such decorrelation can be quantified by measuring the depletion time of molecular gas, defined as the ratio between the molecular mass traced by CO emission, and SFR traced by Hα emission: $\tau_{\rm dep} = M_{\rm H_2,CO}/{\rm SFR}_{\rm H\alpha}$. One measures $\tau_{\rm dep}$ in apertures of different sizes and centered on peaks of either the CO or Hα map, then compare the results to the mean depletion time of the whole galaxy $\tau_{\rm dep,galaxy}$. Due to the spatial mismatch between CO and Hα peaks, on sub-100 pc scales $\tau_{\rm dep} > \tau_{\rm dep,galaxy}$ when measured around CO peaks, and $\tau_{\rm dep} < \tau_{\rm dep,galaxy}$ when measured around Hα peaks, but the difference diminishes as the aperture size increases, vanishing almost completely at $\sim$kpc scales.

To mimic real observations, we first modify our maps by applying the resolution and detection limits reported by Kruijssen et al. (2019) for the nearby spiral galaxy NGC 300, which are typical of other applications of this method. Their observations have a pixel size of 20 pc, a $\Sigma_{\rm H_2,CO}$ detection limit of 13 M$_\odot$ pc^{-2}, and a $\Sigma_{\rm SFR,H\alpha}$ detection limit corresponding to an Hα-inferred star formation rate $\Sigma_{\rm SFR,H\alpha} = 8.05 \times 10^{-3}$ M$_\odot$yr^{-1}kpc^{-2}. Then we follow the pipeline described by Kruijssen et al. (2018) to generate the tuning fork diagram. The first step is to plot both $\Sigma_{\rm H_2,CO}$ and $\Sigma_{\rm SFR,H\alpha}$ maps at the finest available resolution of 20 pc (Figure 4.1), then cut all pixels below the detection limits above. Applying these detection limit thresholds removes $\sim 11\%$ of the molecular mass and $\sim 13\%$ of the Hα emission, so the effects on star formation and molecular mass are comparable. We then determine a mean depletion time $\tau_{\rm dep,0}$ by summing the molecular gas mass and star formation rate over the remaining pixels and taking their ratio. Secondly, for a given scale L, we smooth both maps with a top hat filter with aperture size L, then identify local maxima from each map as emission peaks. If L is large enough for some of the apertures to overlap, we randomly select 500 sub-samples of non-overlapping apertures around identified peaks, then calculate the mean $\Sigma_{\rm H_2,CO}$ and $\Sigma_{\rm SFR,H\alpha}$ values from the whole collection of sub-samples. The depletion time of aperture size L ($\tau_{\rm dep}(L)$) is calculated as the ratio between these two mean values. Due to the stochasticity of our star formation algorithm, the birth of young massive stars is random in our simulation. To minimize this noise, we perform the analysis above for 20 snapshots between 704 Myr and 723 Myr, then plot the 16th, 50th and 84th percentiles of the ratio $\tau_{\rm dep}(L)/\tau_{\rm dep,0}$ around CO emission peaks (top branch) and Hα peaks (bottom branch) in Figure 4.2. We also show the measured values for NGC 628 (Chevance et al. 2020) for comparison; we choose this galaxy as an appropriate comparison because it has a total mass and size comparable to our simulated galaxy.

The plot shows that our simulated galaxy reproduces the observed tuning fork-like shape. At large scales ($L \leq 1$ kpc), the two branches of the fork converge because the aperture size is large enough to include many CO peaks and Hα peaks, making the depletion time equal to the galactic average value. When the aperture scale comes down, especially to $L < 100$ pc, the branches diverge as a result of decoupling between H II region and molecular gas. The overall shape is in good agreement with the results from NGC 628 (Chevance et al. 2020), and a quantitative comparison confirms this visual impression. Below in Section 4.4.2 we apply the same HEISENBERG code (Kruijssen et al. 2018) that Chevance et al. apply to NGC 628 to estimate the characteristic spacing λ between the CO emission peaks and Hα emission peaks from our simulated images, and we obtain $\lambda = 103.2^{+58.3}_{-19.7}$ pc, whereas Chevance et al. find $\lambda = 113^{+22}_{-14}$ pc for NGC 628 – identical to within the uncertainties. This confirms the reliability of our stellar feedback models, especially on cloud scale, and gives us the confidence to begin examining how star formation rate traced by Hα differs from the "true" star formation rate one can infer directly from YSOs.

To further test whether the simulated molecular clouds has similar properties to observed ones, we plot the mass distribution of molecular clouds identified from the same 20 snapshots. Each cloud here represents an enclosed CO emission contour above the detection limit, and its mass is calculated as the total mass converted from the CO emission inside the contour. For a cloud mass function with the form $dN/dM \propto M^{-\beta}$, Faesi et al. (2018) determine the power law slope from GMCs in NGC 300 to be $\beta = 1.76 \pm 0.07$. As shown in Figure 4.3, the slope of the simulated cloud mass distribution well agrees with the NGC 300 observation, confirming the credibility of our synthetic observations.

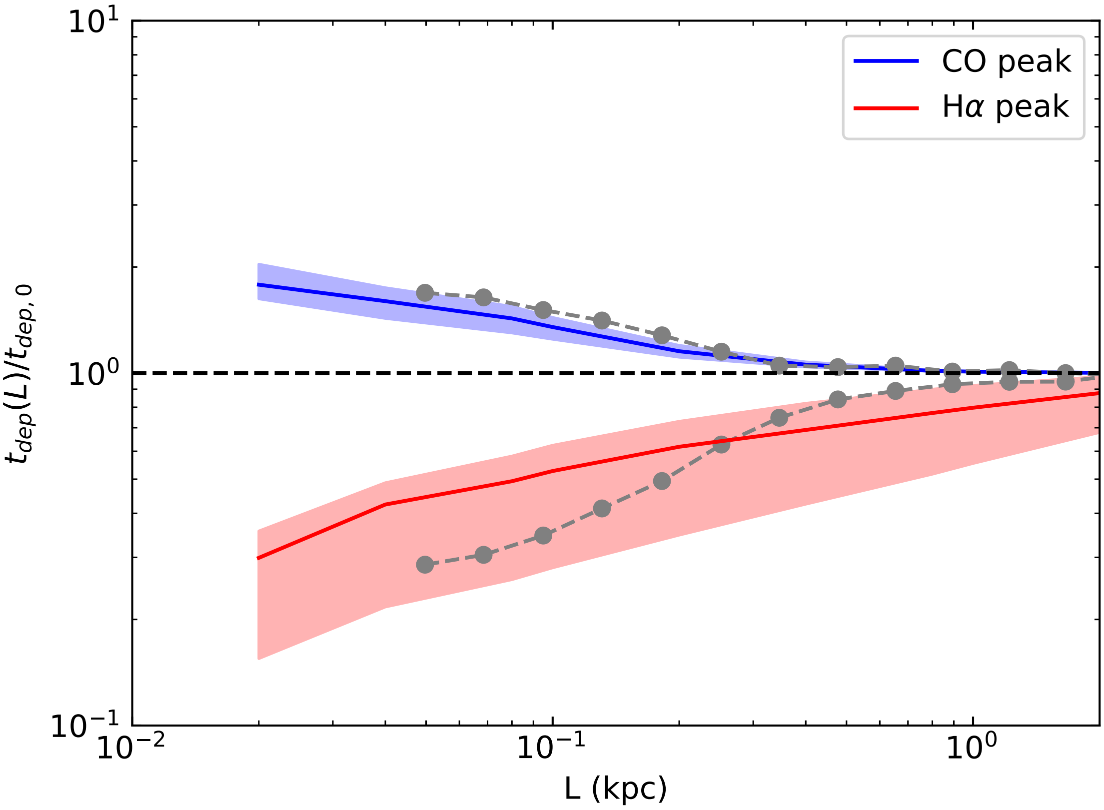

Figure 4.2: Tuning fork diagram from synthetic Hα and CO emission observations. $\tau_{\rm dep,0}$ is the mean molecular gas depletion time of the whole galaxy, while $\tau_{\rm dep}(L)$ is the depletion time calculated within an aperture of size L, centered around CO peaks (upper, blue branch) or Hα peaks (lower, red branch). Both branches are stacked over 20 snapshots between 704 Myr to 723 Myr, with the solid line indicating the median and the shaded region showing the 16th to 84th percentiles. The dotted gray lines are the observed tuning fork diagram for NGC 628 (Chevance et al. 2020).

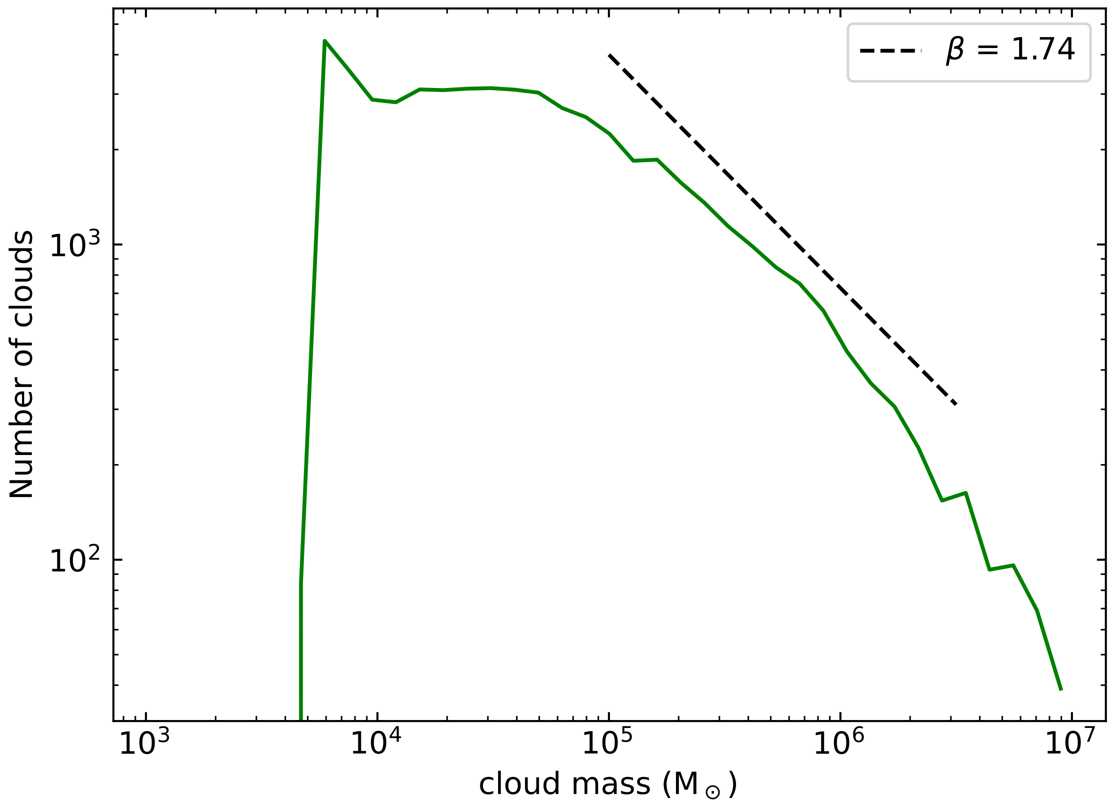

Figure 4.3: Mass distribution of CO-bright molecular clouds from synthetic observations. The dashed line gives the observed power law slope found in NGC 300 (Faesi et al. 2018).

4.3.2 Comparison of SFRs from Hα emission and direct YSO counts

To study how well Hα luminosity traces recent star formation history, we first compare their spatial distributions qualitatively. In Figure 4.4, we plot contours of $\Sigma_{\rm SFR,H\alpha}$ (red), $\Sigma_{\rm SFR,YSO}$ (black), and $\Sigma_{\rm H_2,CO}$ (blue); the Hα and CO contour levels corresponds to detection limits in the observation of NGC 300, and the $\Sigma_{\rm SFR,YSO}$ contour level is set to enclose pixels that include at least one YSO with age < 2 Myr. To make the differences easier to see, we zoom in to a 3 kpc × 3 kpc patch of the galaxy, with the galactic center at the lower right corner; the pixel size is 20 pc for consistency. From the plot, we can clearly see a spatial mismatch: many H II regions contain no YSOs (though the great majority of these do contain older stars, with ages of $2-5$ Myr), while others are much more spatially extended than the corresponding $\Sigma_{\rm SFR,YSO}$ contours. Averaged over 20 snapshots, the overlapping area between the Hα and YSO contours accounts for about only 38% of the total area of Hα contours, and about 70% of the total area of YSO contours. Such mismatch indicates that on sub-100 pc scale, Hα luminosity is an imperfect tracer of recent star formation history. Note that YSO contours are spatially well associated with CO contours in Figure 4.4 since GMCs are the birth sites of YSOs.

To quantify the difference between the Hα- and YSO-based star formation rates as a function of spatial scale, we first construct maps of both $\Sigma_{\rm SFR,H\alpha}$ and $\Sigma_{\rm SFR,YSO}$ with pixel sizes ℓ ranging from 10 pc to 3 kpc. For each pair of maps with same pixel size, we define their relative difference as

$$\delta(\ell) = \frac{\sum_i |\Sigma_{{\rm SFR,H}\alpha,i} - \Sigma_{{\rm SFR,YSO},i}|}{2\sum_i \Sigma_{{\rm SFR,YSO},i}}, \tag{4.7}$$

where $\Sigma_{{\rm SFR,YSO},i}$ and $\Sigma_{{\rm SFR,H}\alpha,i}$ are the YSO- and Hα-derived SFRs in pixel i for the map of pixel size ℓ, and the sums run over all pixels. We illustrate this procedure in Figure 4.5, where we plot the galactic $\Sigma_{\rm SFR}$ maps for Hα and YSOs (1st and 2nd columns), and the normalised absolute difference $|\Sigma_{\rm SFR,H\alpha} - \Sigma_{\rm SFR,YSO}|/2\bar{\Sigma}_{\rm SFR,YSO}$ (3rd column), where $\bar{\Sigma}_{\rm SFR,YSO}$ is the mean of $\Sigma_{\rm SFR,YSO}$ over all pixels, at pixel sizes $\ell = 0.1$, 1, and 3 kpc (top to bottom rows). The quantity $\delta(\ell)$ defined in equation 4.7 is simply the mean value of the maps in the third column. As shown in the figure, when ℓ increases, the difference between $\Sigma_{\rm SFR}$ maps drops, and thus δ becomes smaller.

Because we have normalised the total SFRs derived from Hα and YSOs to be equal when summed over the full galaxy, δ is constrained to lie in the range $0-1$, with $\delta = 0$ when the two maps are exactly the same and $\delta = 1$ when they are completely

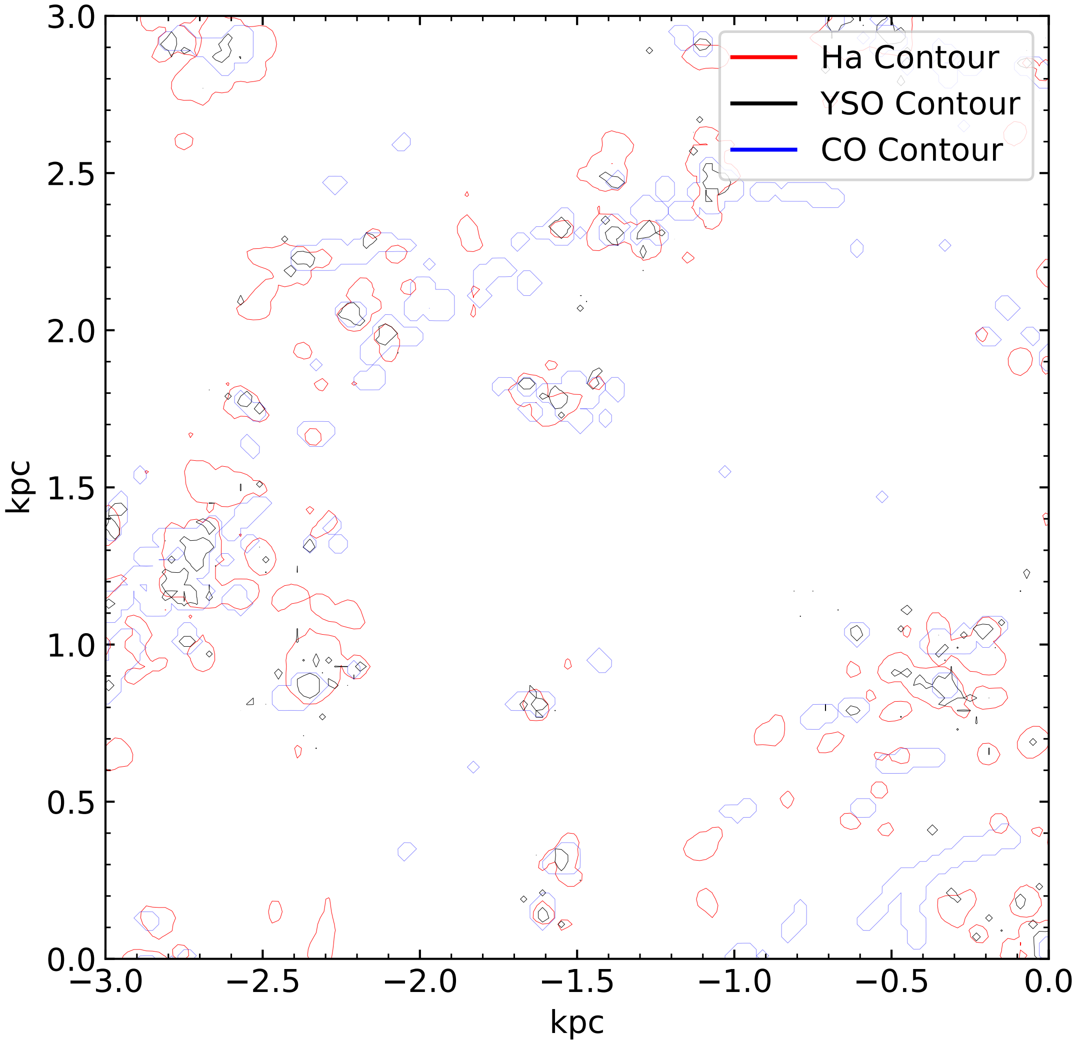

Figure 4.4: Contour plots of $\Sigma_{\mathrm{SFR,H\alpha}}$ (red), $\Sigma_{\mathrm{SFR,YSO}}$ (black), and $\Sigma_{\mathrm{H_2,CO}}$ (blue) within the inner galaxy. The contour level for $\Sigma_{\mathrm{SFR,H\alpha}}$ is 8.05×10^{-3} $\mathrm{M_\odot yr^{-1} kpc^{-2}}$, and the contour level for $\Sigma_{\mathrm{H_2,CO}}$ is 13 $\mathrm{M_\odot}$ $\mathrm{pc^{-2}}$, same as the detection limits in the observation of NGC 300; YSO contours are drawn out of pixels with at least one YSO. The galactic center is at the lower right corner of the plot, while the pixel size is 20 pc, the same as Figure 4.1.

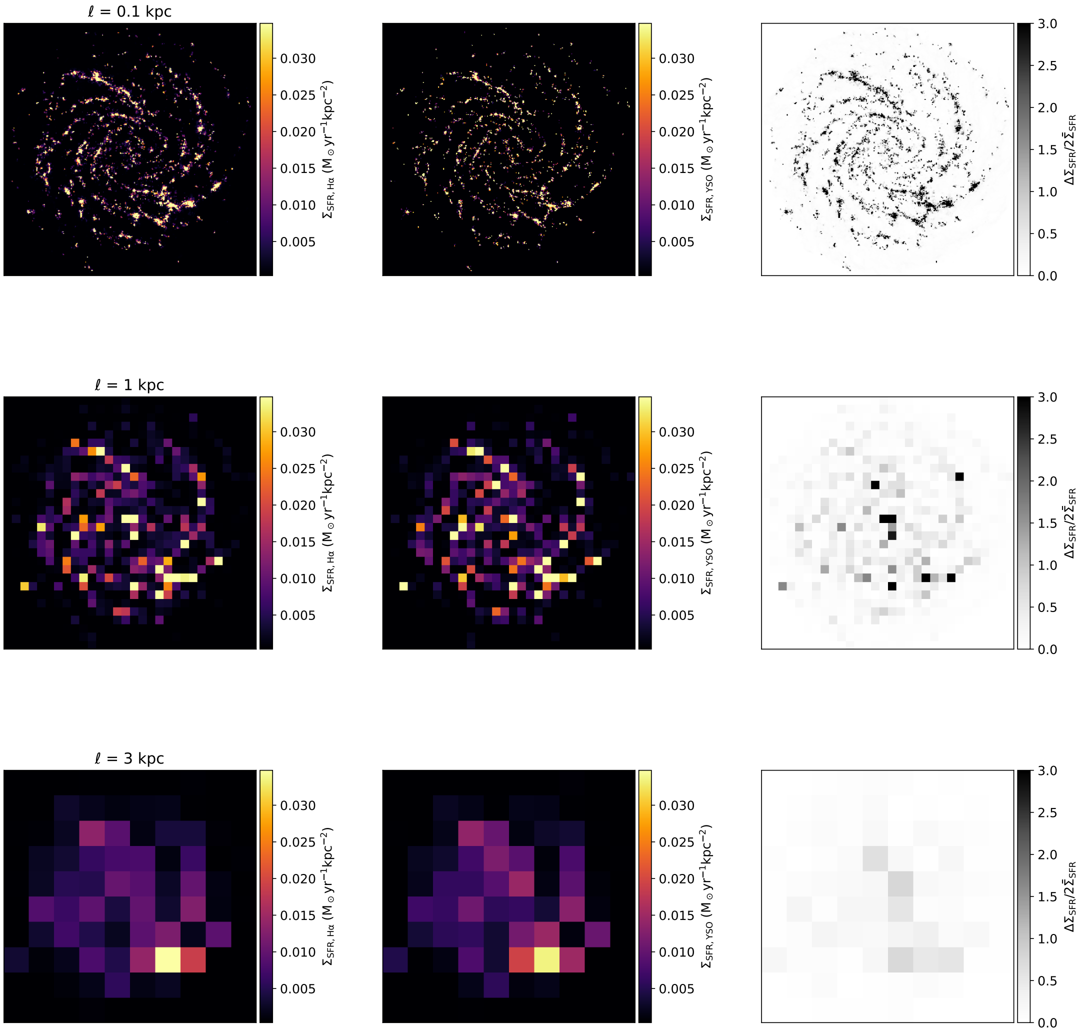

Figure 4.5: SFR surface density $\Sigma_{\rm SFR}$ maps and their differences at different resolutions. All maps are generated from face-on projections of the simulation snapshot at 720 Myr. Plots in different rows uses different pixel sizes ℓ, as indicated in the first column. The first two columns show the $\Sigma_{\rm SFR}$ maps traced by Hα emission and YSOs, respectively, while the third column shows the normalised absolute difference between the first two columns (see main text for details).

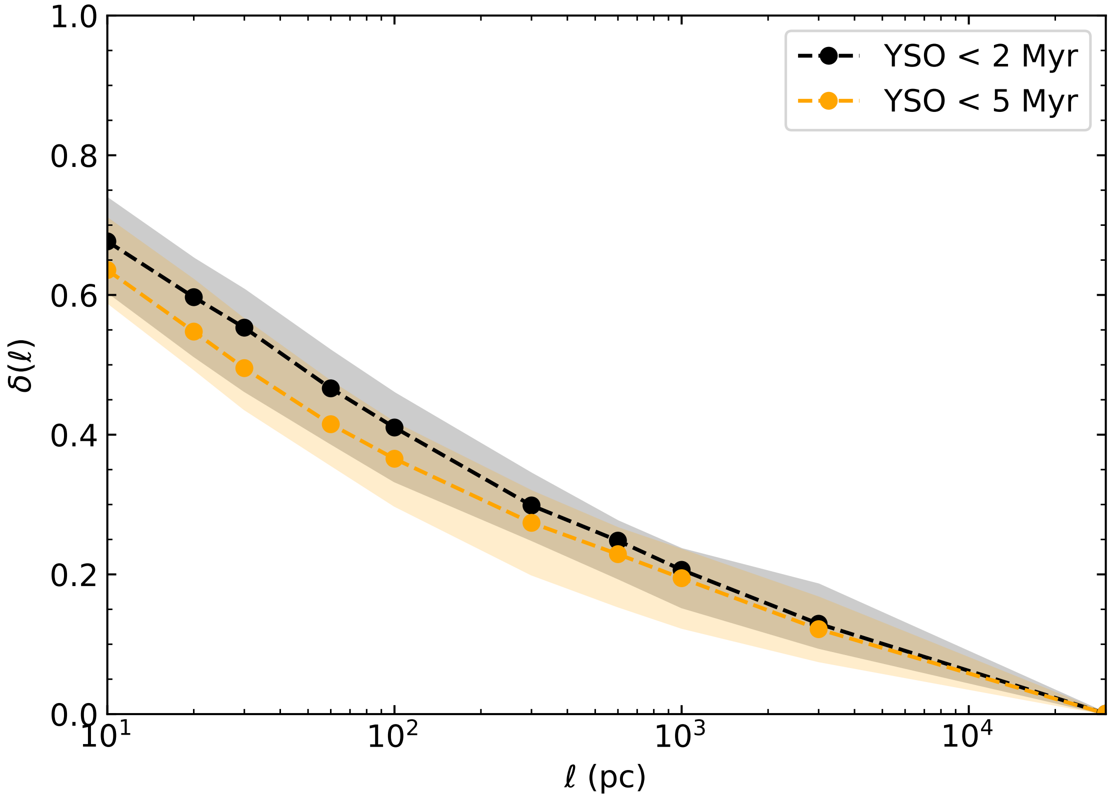

Figure 4.6: Normalised difference $\delta(\ell)$ between galactic SFR maps traced by Hα and direct YSO counts as a function of pixel size ℓ. The results are stacked from 20 snapshots from 704 Myr to 723 Myr. Different colors of the bands indicate different YSO age ranges used for SFR calculation: < 2 Myr (black) and < 5 Myr (orange). The dotted lines are the median values, while the band shows the 16th to 84th percentile range.

non-overlapping. We plot the $\delta(\ell)$ versus the pixel size ℓ in Figure 4.6. Similar to Figure 4.2, we present the results stacked from 20 snapshots between 704 Myr and 723 Myr by showing the 50th percentile as the dotted lines, and the 16th and 84th percentiles as band edges. We also show the results from YSOs with over two ranges, for reasons we discuss below in Section 4.4.1. From $\ell = 1$ kpc to $\ell = 10$ pc, we see that $\delta(\ell)$ quickly increases, and reaching values ~ 0.5 at sub-100 pc scales. This indicates Hα luminosity intrinsically fails to trace the recent star formation rate on sub-100 pc scales, and cannot be used for studying the star formation history of molecular clouds without a great deal of caution.

4.4 Discussion

In this section, we first discuss the physical mechanisms behind the breakdown of Hα as a SFR tracer on small scales (Section 4.4.1), and consider the implications of this for inferences of molecular cloud properties (Section 4.4.2). Then we develop an improved method to calibrate Hα measurements for individual molecular clouds (Section 4.4.3). Finally we propose future work with the help of most recent observations (Section 4.4.4).

4.4.1 Why Hα fails on small scales

We first seek to understand the physical mechanisms responsible for the breakdown of Hα as a SFR tracer on small scales. As a start, we can immediately discard one obvious possibility, which is stochastic sampling of stellar populations (e.g., da Silva et al. 2012, 2014; Krumholz et al. 2015; Arora et al. 2021). While this is potentially an important effect at small scales, as we shall see below, stochasticity is not consistent with the pattern shown in Figure 4.5. If the primary effect were stochasticity, we would expect to see many contours containing YSOs but little Hα, corresponding to regions containing a recently-formed population that is deficient in massive stars. While there are a few examples of such structures, Figure 4.5 shows that a far larger effect is Hα contours that are more extended than YSO ones, or without any YSOs present at all.

This leads us to focus on two alternative explanations: drift of young massive stars, and transport of of ionizing photons. With regard to the former, we note that in Galactic observations YSOs identified from IR excess are normally younger than 2 Myr old, and we have followed this convention in our definition of YSOs. However, stars with significant ionizing luminosities can have lifetimes up to ≈ 5 Myr. Once the stars are formed, they are no long subject to gas pressure and may drift out of their mother molecular cloud, and so one might hypothesise that Hα differs from YSOs because it traces an older and more dispersed stellar population. We test for this effect in Figure 4.6, where we compare the mismatch parameter $\delta(\ell)$ computed for our fiducial YSO age limit or 2 Myr (gray band) to one derived using an age limit of 5 Myr instead (orange band); the latter should include all significant sources of ionizing photons. We see that the extending age limit to 5 Myr does reduce the mismatch between Hα and YSOs, but only by $\sim 10\%$. This suggests that stellar drift is not the primary culprit. Note that runaway stars, which are stars formed in dense gas and ejected into low-density region with high velocity, can also lead to high SFR measurements in diffuse gas. This physical mechanism is not included in our simulation, while the numerical modeling by Andersson et al. (2021) finds that runaway stars can contribute to a $\Sigma_{\rm SFR} \sim 10^{-4} - 10^{-6}\ {\rm M_\odot yr^{-1} kpc^{-2}}$ in low surface density gas. Since this value is smaller than the detection limit in our synthetic Hα observations, the effect of runaway stars is generally trivial in our analysis, but can be important for individual H II regions in observations.

This leaves ionizing photon transport as the prime suspect. With regard to this phenomenon, we note that previous observations and theoretical models have found that ionizing photons can leak out of compact H II regions, and create diffuse Hα components up to even ~ 1 kpc above the galactic plane (e.g., Mathis 1986; Sembach et al. 2000; Wood et al. 2010; Belfiore et al. 2022). In the study of nearby disk galaxies by Pflamm-Altenburg & Kroupa (2008), they find that this photon leak effect becomes significant for gas surface densities $\Sigma_{\rm gas} < 10$ M$_\odot$ pc^{-2}. However, their $\Sigma_{\rm gas}$ measurements are averaged over $\sim$kpc scales, so the photon leak effect on cloud scales is still not well quantified. Our simulation, however, is perfectly suited to such a study, because when a gas parcel is newly ionized we set its temperature to exactly 10^4 K, and therefore gas parcels at this temperature perfectly outline the outer boundaries of H II regions. We can easily locate these particles in the output snapshots, allowing us to determine how far ionizing photons can travel.

Our analysis comes in three steps: first we record the coordinates of all gas particles with temperature of exactly $T = 10^4$ K; then we build a K-D tree containing the coordinates of stars with ages < 5 Myr, which are potential sources of ionizing photons; finally, for each identified gas particle, we find the closest young star using the K-D tree. For each gas particle, we record both the distance D to the closest star and the total gas column density $N_{\rm H}$ around the star; we measure $N_{\rm H}$ in a circular region around the star with a radius of 100 pc in order to smear fluctuations while retaining cloud scale information. We perform this analysis on snapshots from 704 Myr to 723 Myr, and we plot the 16th, 50th, and 84th percentiles of D versus $N_{\rm H}$ in Figure 4.7. This plot shows a clear trend that D decreases with $N_{\rm H}$, which indicates that denser regions can absorb more ionizing photons, and confine the H II regions to smaller sizes. The median H II region size drops below 100 pc for $N_{\rm H} > 2 \times 10^{21}$ cm^{-2}, suggesting that we should find better agreement between Hα and YSO-based SFRs if the YSOs are embedded in dense regions.

To test this hypothesis, we plot the galactic SFR maps from the same snapshots with a pixel size of 100 pc; then for each pixel containing at least one YSO, we calculate the ratio $\Sigma_{\rm SFR,YSO}/\Sigma_{\rm SFR,H\alpha}$ and the column density $N_{\rm H}$. We plot this ratio as a function of $N_{\rm H}$ in Figure 4.8, where we again show the median value as the solid line and the 16th to 84th percentiles as the shaded region. As the Figure shows, when YSOs reside in a low surface density region, the corresponding H II region greatly expands beyond the 100 pc pixel, leading to a substantial mismatch between the Hα and YSO-based SFRs. Conversely, when the local column density becomes high enough ($N_{\rm H} \gtrsim 3 \times 10^{21}$ cm^{-2}, or $\Sigma_{\rm gas} > 32$ M$_\odot$ pc^{-2}), Hα begins to agree very well

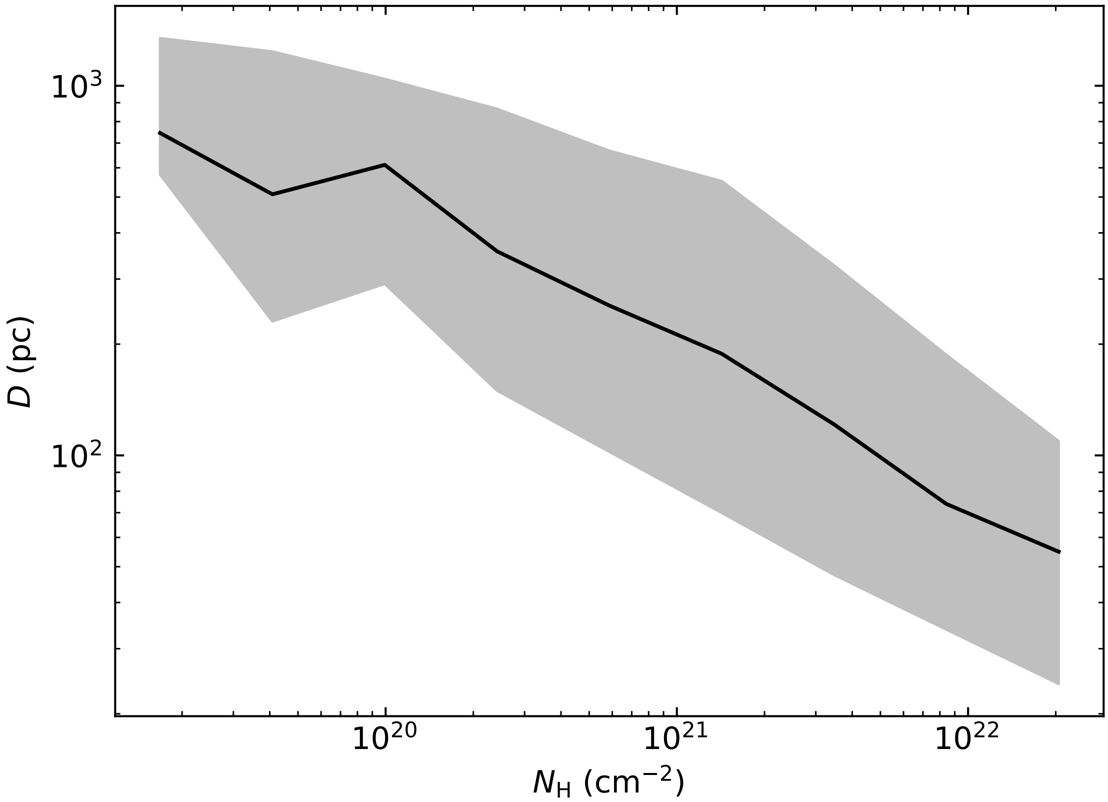

Figure 4.7: H II region size D versus the column density around stars $N_{\rm H}$. The solid line shows the median value, while the top and bottom edges of the shaded region are the 16th and 84th percentiles. D is measured as the distance between gas particles that are just photonionized and the closet star born within 5 Myr, while $N_{\rm H}$ is measured inside a beam with a diameter of 100 pc around that star. The results are stacked from galactic maps of 20 snapshots.

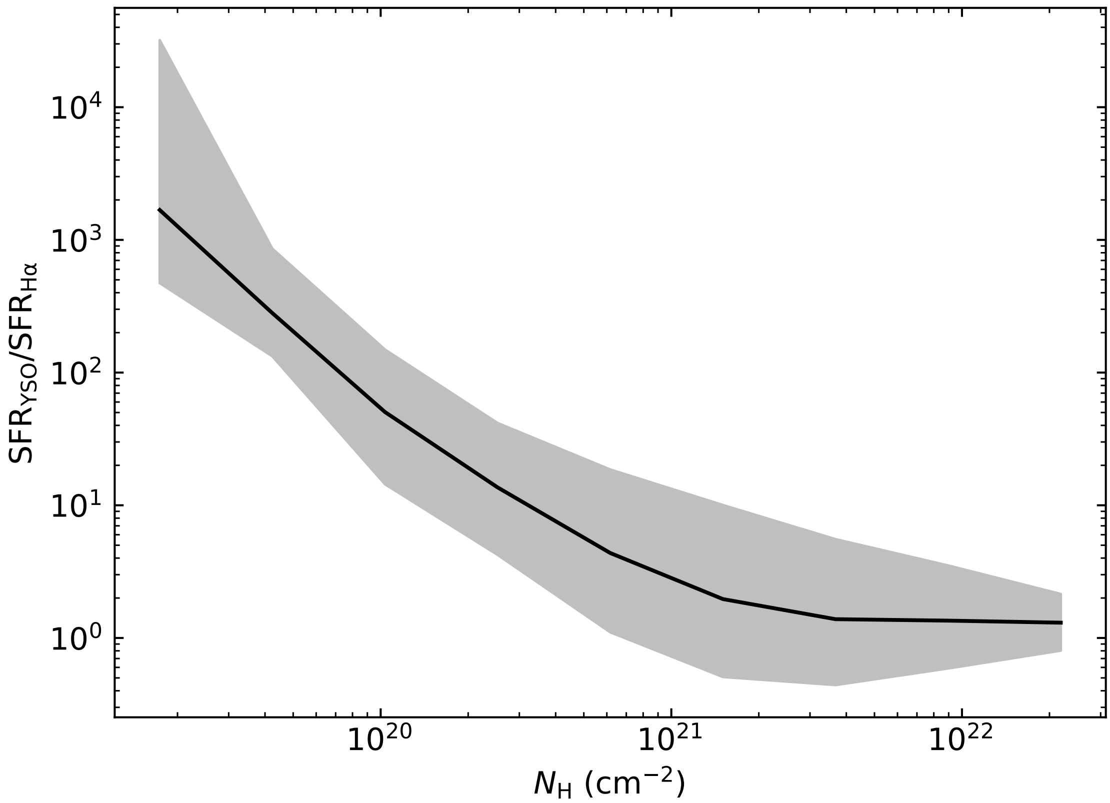

Figure 4.8: Ratios between SFRs traced by Hα luminosity and YSO versus the column density N_H, both calculated from 100-pc-large pixels with YSOs inside. The results are stacked from 20 snapshots between 704 Myr and 723 Myr. The mid solid line is the median value, while the shaded region shows the range between the 16th and 84th percentiles.

with YSOs because the H II region is well confined. We therefore conclude that Hα luminosity is only locally trustworthy for dense regions with $N_\mathrm{H} \gtrsim 10^{21}$ cm^{-2}, while the exact threshold needs calibration from future high resolution observations.

We need to note that while we have shown above that drift of young stars away from their birth sites is not the direct cause of the Hα-YSO mismatch, it may play a significant role in enhancing ionizing photon transport, together with the closely related effect that young stars drive away nearby dense gas with pre-supernovae stellar feedback. In either case, the effect is that the local column density around the stars drops with time, which enables the ionizing photons to travel further and enlarges the SFR tracers mismatch. Quantitatively, we find that the column density around a star on average drops by a factor of ≈ 10 from the moment of its birth to the age of 5 Myr. Moreover, about 71% of the YSOs < 2 Myr old reside in CO contours where $\Sigma_{\mathrm{H_2,CO}} \geq 13$ M$_\odot$ pc^{-2}, our rough threshold for H II region confinement to $\lesssim 100$ pc sizes; for stars with ages between 2 and 5 Myr, this fraction drops to $\approx 38\%$. Thus the mismatch between Hα and YSOs due to ionizing photon transport is mainly driven by older YSOs that have, either by drift or by dispersing their natal gas, escapes to low-density regions from which their ionizing photons can propagate long distances. This phenomenon has also been observed in another recent theoretical modeling effort by McClymont et al. (2024), who find that the diffuse ionized gas (DIG) is primarily ionized by older stars instead of embedded YSOs.

Besides the intrinsic complexity of H α emission, the dust extinction effect may also increase the uncertainty of local SFR measurements in real observations. Barrera-Ballesteros et al. (2020) study the relation between $\Sigma_{\rm gas}$ from CO emission and dust extinction A_V on global, radial, and kpc scales. Although they can fit a linear $\Sigma_{\rm gas} - A_V$ relation from galactic averaged values, on kpc scale they find an dust extinction scatter$\delta(A_V) \sim 0.5$ dex, which can be converted to a ~ 0.2 dex uncertainty in the term $C_{\rm H\alpha}$ in equation 4.6. This uncertainty is likely due to the complicated spatial distribution of gas, dust, and stars on small scales, thus can be more severe when studying individual GMCs below kpc scale. Therefore, for future observational studies of sub-kpc scale star formation, local dust extinction measurements should be preferred over galactic averages.

4.4.2 Implications for statistical inferences of the molecular cloud life cycle

The fact that Hα-based SFRs are significantly distorted on small scales by photon transport effects has important implications for the interpretation of the small-scale gas-SFR decorrelation, which is often used to deduce properties of the molecular cloud life cycle and star formation process. To understand these implications, we begin by quantifying how photon transport effects contribute to the tuning fork diagram on small scales. We do this by constructing tuning fork diagrams using the same analysis method described in Section 4.3.1, but this time using the SFR map derived from YSOs instead of Hα, both for YSOs with ages < 2 Myr and < 5 Myr. We show the result in Figure 4.9, together with Hα-based result we obtained in Section 4.3.1.

We find that, unlike Hα, YSOs with ages < 2 Myr are spatially well correlated with the CO emission, so the upper branch of the black plot is close to unity across different scales. The lower branch is below unity, since when the aperture is located around YSO mass peaks, the local stellar particles are grouped together more tightly than the corresponding gas, making the local depletion time smaller than the galactic average value. The comparison between Hα and YSOs with ages < 5 Myr is perhaps more informative, since in this case we are probing very close to the same time scale as Hα, and thus any differences between the Hα and 5 Myr YSO tuning forks translate directly to changes in the inferred properties of molecular clouds. We find that, when the stellar age increases, either YSOs drift away from the CO emission peaks or molecular clouds are dispersed by feedback, resulting in both the upper and lower tuning fork branches deviating from unity. However, the deviation is noticeably smaller than for Hα.

Examining published analyses based on the SFR-gas decorrelation (e.g., Kruijssen et al. 2018; Kruijssen et al. 2019; Chevance et al. 2020; Chevance et al. 2021), it is clear that a tuning fork that opens more narrowly and at small scales implies molecular clouds whose positions are correlated on smaller scales and which spend significantly longer in the "overlap" phase when both tracers of star formation and gas are present, and clouds have not been dispersed by feedback; it is likely that the inferred overall molecular cloud lifetime would increase as well.

To quantify this effect, we use the publicly-available HEISENBERG code (Kruijssen et al. 2018) to analyze all three tuning fork diagrams in Figure 4.9. As a first step in this analysis, we test whether HEISENBERG's diffuse emission filter can remove the effects of Hα emission coming from diffuse ionised gas (DIG) far from YSOs. The full algorithm implemented by this filter is described by Hygate et al. (2019), so here we only summarize for reader convenience. The first step is to first draw a tuning fork diagram and fit the average spacing between emission peaks λ from the original emission map; doing so we obtain $\lambda = 103.2^{58.3}_{-19.7}$ pc. We then filter out the diffuse component by transforming the Hα map into Fourier space, applying a high-pass filter to remove modes with wave number $\gtrsim 1/k$, and then transforming back to physical space. We then re-fit λ by applying HEISENBERG to the filtered map, and iterate the process of fitting, filtering, and re-fitting until λ changes by less than 5% between two successive iterations. Applying this procedure to our Hα map, we find that the process converges in six iterations, with the characteristic separation stablizing at $\lambda = 91^{+13}_{-11}$ pc; the mean is only 10% less than the non-filtered result, and the two are consistent within the formal uncertainties. Moreover, the fraction of diffuse Hα flux is measured to be only $\sim 8\%$. These indicate that the effect of DIG is limited in our synthetic observations, a result that can be understood as coming from two effects: first, we have already suppressed much of the DIG emission by removing Hα emission below the detection limit; second, the spatially extended Hα emission due to photon transmission effect is not distinct from compact H II regions, as they are originally generated by the same sources. Given the minimal effects of filtering, we turn off this module for the remainder of our analysis with HEISENBERG, which allows us to use the same procedure to analyze both the Hα-derived and YSO-derived

Tracer	λ (pc)	$t_{\rm gas}$ (Myr)	$t_{\rm over}$ (Myr)	$t_{\rm ref}$ (Myr)
Hα	$103.2^{+58.3}_{-19.7}$	$27.6^{+15.8}_{-4.7}$	$8.4^{+6.0}_{-2.0}$	$4.3^{+0.1}_{-0.2}$
YSO < 5 Myr	$51.1^{+19.3}_{-8.6}$	$33.2^{+31.6}_{-7.9}$	$10.6^{+12.4}_{-3.3}$	5.0
YSO < 2 Myr	$38.5^{+10.8}_{-5.9}$	$141.7^{+33.0}_{-48.4}$	$30.2^{+8.7}_{-10.5}$	2.0

Table 4.1: HEISENBERG fitting results for the tuning fork diagrams shown in Figure 4.9. The first column lists the SFR tracer used, the middle three columns are the fitted physical quantities describing mean cloud separation, duration of gas-only phase, and duration of gas-star overlap phase, and the last column provides the star-only phase duration $t_{\rm ref}$, which is used as the reference time scale in fitting.

star formation maps, eliminating a possible source of systematic difference.

We next use HEISENBERG to derive the durations of two phases in the cloud life cycle: the gas-only phase $t_{\rm gas}$ during which only the molecular gas tracer is present and the "overlap" phase $t_{\rm over}$ during which both tracers of star formation and gas are present. We do this for both the Hα map and the two YSO-derived maps. When fitting the durations of these two phases, HEISENBERG requires that we supply a reference duration of the star-only phase $t_{\rm ref}$. For Hα emission, we adopt $t_{\rm ref} = 4.3^{+0.1}_{-0.2}$ as measured from a disc galaxy simulation at Solar metallicity (Hygate et al. 2019). For the star formation maps derived from YSOs with ages < 2 Myr and < 5 Myr, we set $t_{\rm ref}$ to 2 and 5 Myr, respectively. We report the results returned by HEISENBERG in Table 4.1.

From this table it is obvious that when the SFR is traced by YSOs with ages < 5 Myr instead of Hα emission, the fitted value of λ decreases by $\sim 50\%$, and the duration of the "overlap" phase increases by $\sim 25\%$. The effect is even more dramatic if we consider YSOs with ages < 2 Myr, but the uncertainties are extremely large, and it is possible that the method itself breaks down in this case because for these young YSOs the upper branch of the tuning fork does not open at all, contradicting a basic assumption of the method. Nonetheless, this analysis makes clear that the very short overlap time inferred by previous studies is substantially biased by photon transport effects in Hα, and that molecular cloud dispersal is perhaps not quite as fast as had been supposed. It is worth noting that this result helps resolve a longstanding tension: existing measurements from CO-Hα decorrelation seem to suggest that molecular clouds have an extended quiescent phase when there are no massive stars present, followed by a very rapid dispersal phase once such stars appear, but this is hard to reconcile with the observation that starless molecular clouds in the Milky Way are exceedingly rare. Our finding suggests a resolution: the dispersal time has

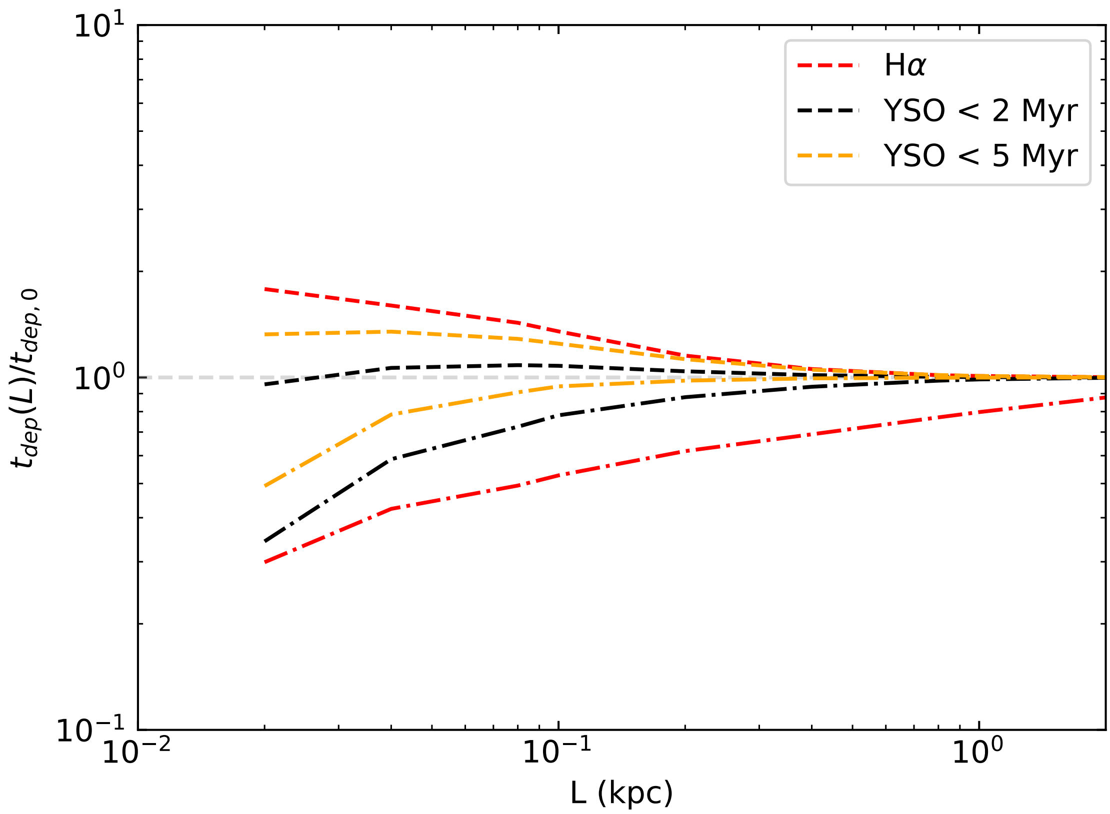

Figure 4.9: Same as Figure 4.2, but now showing tuning forks derived from SFR maps obtained from YSOs with ages < 2 Myr (black) and < 5 Myr (orange) as well as from Hα (red). The lines shown are the medians over 20 time snapshots as in Figure 4.2, but we do not show the corresponding 16th to 84th percentile bands for clarity. Different line styles indicate depletion time ratios calculated around CO emission peaks (dashed) or H α emission peaks (dot-dashed).

been significantly underestimated because much of the CO-Hα decorrelation is due not to cloud dispersal, but to ionizing photons produced by stars at ages $\approx 2-5$ Myr traveling far from their parent stars before being absorbed and giving rise to Hα emission. This picture is also consistent with the recent discovery by Calzetti et al. (2023) using *James Webb Space Telescope* (JWST) of a substantial population of star clusters with ages $\gtrsim 5$ Myr that are still highly dust-embedded.

4.4.3 SFR calibration model

In Section 4.4.1, we find that in regions where YSOs are present in regions of high gas column density, Hα luminosity does approximately trace the recent star formation rate in the 100-pc scale. However, direct identification of extragalactic YSOs is unavailable for all but the few nearest galaxies due to resolution limits, making it impossible to directly apply such criteria to study cloud star formation rate with Hα

emission. Nevertheless, calibration of the Hα tracer to YSOs is still possible because of the strong correlation between molecular clouds and star formation. In essence, if the cloud mass and area is large enough, we can safely assume the existence of embedded YSOs, and therefore assume that we are looking at a region where Hα will be reliable. In our synthetic observations, every CO contour with a mean radius larger than 100 pc has YSOs within it, so we select such CO contours and calculate the total SFR within each of them using both Hα and YSOs. Via this process we obtain a sample of 464 distinct CO contours, with a minimum total molecular gas mass of $\sim 10^6$ $\mathrm{M}_\odot$ and a minimum $\mathrm{SFR}_{\mathrm{H}\alpha}$ of $\sim 10^{-3}$ $\mathrm{M}_\odot \mathrm{yr}^{-1}$. The latter limit is also helpful, because this corresponds to an ionising photon flux of $\sim 10^{49}$ yr^{-1}, about the luminosity of a single O type star. Therefore, this is roughly also the limit below which we expect stochasticity to foil measurements of the SFR from Hα even with limited photon transport effects – an intuition confirmed by detailed SLUG simulations by da Silva et al. (2014). Thus by selecting contiguous regions of significant CO emission with radii > 100 pc, we ensure that these regions almost certainly contain YSOs, and almost certainly contain enough massive stars that stochastic IMF sampling has minimal effects.

We plot the measured $\mathrm{SFR}_{\mathrm{YSO}}$ vs. $\mathrm{SFR}_{\mathrm{H}\alpha}$ for our contours in Figure 4.10. We find that the relation between the two tracers is well-fit by a simple linear (on log scale) model

$$\log_{10} \frac{\mathrm{SFR}_{\mathrm{YSO}}}{\mathrm{M}_\odot\ \mathrm{yr}^{-1}} = k \log_{10} \frac{\mathrm{SFR}_{\mathrm{H}\alpha}}{\mathrm{M}_\odot\ \mathrm{yr}^{-1}} + b. \tag{4.8}$$

The fit coefficients are $k = 0.71$ and $b = -0.33$, and the R^2 value is 0.81, indicating a strong linear relation. This relation can be applied in observation to calibrate the star formation rate of individual clouds where a local YSO catalog is unavailable. Although this relation is limited to large molecular clouds, this is not a severe limitation for extragalactic studies, which commonly achieve spatial resolutions of only ≈ 100 pc (e.g., Chevance et al. 2020), close to our cloud radius limit. Note that we did not consider the effect of dust attenuation in our post-analysis, we assume that we observe the total Hα emission. For application to real observations one must first dust-correct the Hα luminosity (e.g., Kennicutt & Evans 2012; Tacchella et al. 2022).

4.4.4 Future work on nearby galaxies

The results in this work are derived from a simulation of a Milky Way-like galaxy. It is unclear to what extent these results will differ for galaxies of very different star formation rates and sizes, where different stellar feedback effects may dominate com-

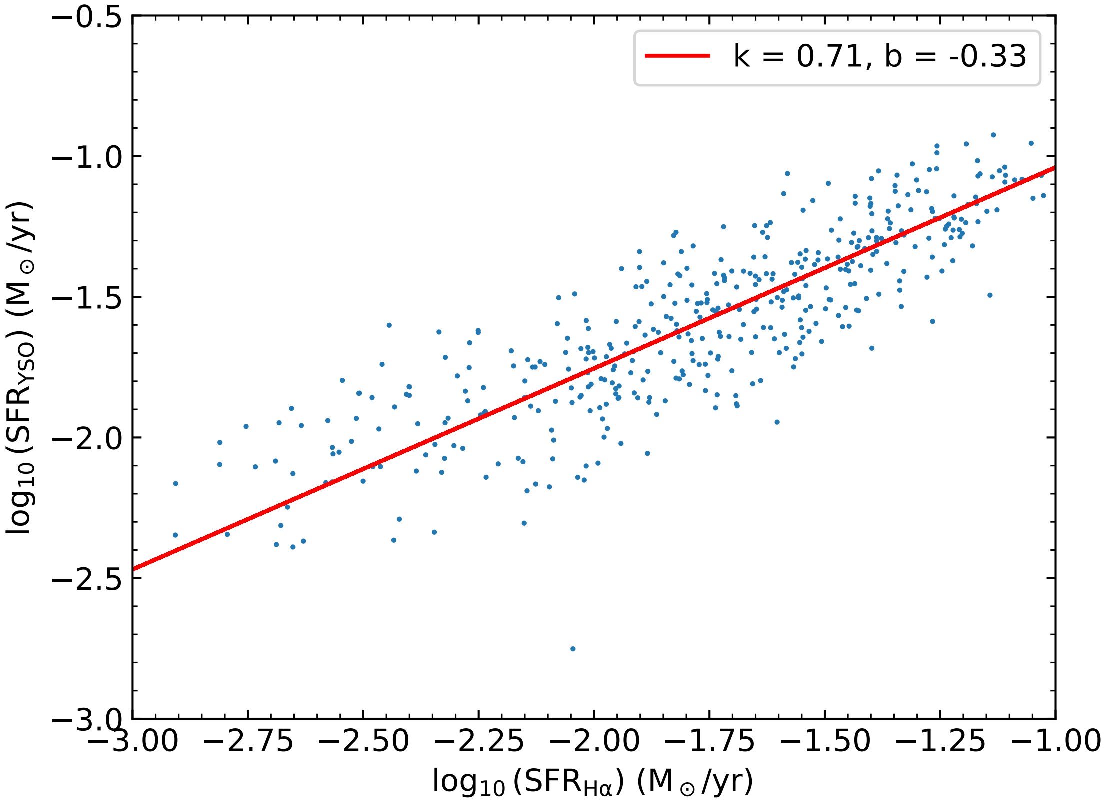

Figure 4.10: Ratios between SFRs traced by Hα luminosity and YSO versus the column density N_{H}, both calculated from 100-pc-large pixels with YSOs inside. The results are stacked from 20 snapshots between 704 Myr and 723 Myr. The mid solid line is the median value, while the shaded region shows the range between the 16th and 84th percentiles.

pared to those in Milky Way-like systems; the properties of the interstellar medium and dust may also differ between galaxies, which can also affect the transmission of ionizing photons.

One approach to mitigate this is of course to extend our simulations to different galaxy types. However, it is also essential to test our results by comparing real high resolution Hα luminosity maps with YSO distribution maps. At present the only viable options for such a test are the "Local Group" galaxies, including the Large and Small Magellanic Clouds (LMC and SMC), and the M33. Hα maps of these galaxies are already available at sub-arcsec resolution, corresponding to physical scale of ~ 0.2 pc. The limiting factor is YSOs: the current YSO catalog for the LMC, for example, is still limited to several small regions. Using *Spitzer* IR survey, previous works have (Indebetouw et al. 2008; Chen et al. 2009, 2010) identified YSOs from the LMC's molecular ridge and two H II complexes. However, the observed area in total is less than 1 kpc^2, and thus not sufficient for systematic comparison of Hα and YSOs across scales. Moreover, their YSO mass detection lower limit varies between 3 $M_\odot$ and 8 $M_\odot$, making SFR estimates strongly depend on both complex completeness calculations and assumptions about the shape of underlying IMF, especially at the low mass end. Nevertheless, high resolution observations empowered by *JWST* now have great potential to identify extragalactic YSOs. Peltonen et al. (2024) observe one spiral arm of M33, and find 793 YSOs with a lower mass limit of ~ 6 $M_\odot$. For closer galaxies like the LMC, *JWST* should be able to detect YSOs down to sub-Solar masses. If identified from the whole galaxy, these YSO catalogs will enable a repetition of our simulation analysis here on real data from a suite of nearby galaxies, which can help us better understand the effect of different galactic environments on GMC life cycles. In the future, we plan to run simulations of these galaxies suitable for direct comparisons to such observations.

4.5 Conclusion

In this work, we investigate the discrepancy between estimates of galaxy star formation rates based on Hα emission and direct measurements from counts of young stellar objects (YSOs), on spatial scales from a whole galaxy to smaller than individual molecular clouds. To this end we first perform high resolution magnetohydrodynamic (MHD) simulations of a Milky Way-like galaxy that can resolve cloud-scale structures, with realistic star formation and stellar feedback algorithms, in particular including a treatment of photoionization feedback that allows us to track the locations of ionized gas. Then we post-process the simulation outputs to derive local chemical compositions, non-LTE level populations, and emissivities of both Hα and CO $J = 1 \to 0$ emission lines. We use these to produce synthetic Hα and CO emission maps, and compare the former to maps of the true star formation rate as traced by YSOs born with ages < 2 Myr. We confirm the reliability of our stellar feedback treatment by showing that our simulations reproduce the so-called "tuning fork" diagram for observed Milky Way-like galaxies, which quantifies the degree of small-scale decorrelation between CO and Hα maps of galaxies.

We find that the Hα- and YSO-based SFR maps have good agreement on kpc scales, but exhibit significant spatial mismatch on sub-100 pc scales. We show that the primary cause for this discrepancy is the leakage of ionizing photons from H II regions, especially in low column density regions, with a subdominant contribution due to stars with ages of $\approx 2 - 5$ Myr drifting away from their birth sites. We therefore conclude that on sub-100 pc scales, Hα should be used as a star formation tracer only with extreme caution, and we show that tuning fork diagrams derived from true YSO positions rather than Hα emission differ significantly in a way that may have led prior analyses to substantially underestimate the time it takes for newborn stars to disperse their parent clouds.

However, we also show that Hα emission does become a reasonably reliable tracer of star formation in regions of high gas density, $N_{\mathrm{H}} \gtrsim 3 \times 10^{21}$ cm^{-2} when averaged over 100 pc scales, because in such regions ionizing photons are absorbed close to their emission sites and leakage has minimal effects. We propose a calibration model that exploits this result and allows reliable measurements of the SFRs of large molecular regions ($r \gtrsim 100$ pc) from Hα luminosity. Future high-resolution observations powered by *JWST* are essential to test our findings and refine this calibration model, and allow more accurate measurements of star formation rates across different environments.

Acknowledgements

We thank the anonymous referee for a helpful and constructive report that improved this paper. We acknowledge Dr. Diederik Kruijssen and Dr. Mélanie Chevance for suggestions on running the HEISENBERG code. The authors acknowledge funding from the Australian Research Council through its Future Fellowship and Laureate Fellowship funding schemes, awards FT180100375 and FL220100020, as well as its Discovery Projects scheme (award DP230102280), the Australia-Germany Joint Research Cooperation Scheme (UA-DAAD), and high-performance computing resources provided by the Australian National Computational Infrastructure (grants jh2 and ek9) and the Pawsey Supercomputing Centre (grant pawsey0810) through the National and ANU Computational Merit Allocation Schemes, and by the Leibniz Rechenzentrum and the Gauss Centre for Supercomputing (grants pr32lo, pr48pi and GCS Large-scale project 10391).

Data Availability

The data underlying this article will be shared upon reasonable request to the corresponding author.

Chapter 5

Conclusions

5.1 Summary of this thesis

The aim of this work is to understand the life cycle of GMCs and star formation process within them. With careful comparison between simulation output and synthetic observation, we find that GMC properties measured from observations can be highly biased due to projection, chemical, and excitation effects, which lead to erroneous conclusions at all phases of the GMC life cycle, including the cloud formation, star formation, and cloud dispersal.

During the formation of GMCs, previous Zeeman effect measurements suggested a transition from a sub-critical phase to super-critical phase concomitant with the transition from atomic to molecular gas. On the contrary, our analysis shows that this apparent transition is primarily an illusion created by chemical and excitation biases, and that magnetic fields alone can not prevent gravitational collapse of ISM even prior to the formation of GMCs (Chapter 3). Once GMCs are formed, measurements of their SFEs have significant systematic errors due to projection effects: we have limited information regarding the cloud scale in the LOS direction, and thus cannot accurately calculate the volume density. Using a theoretical model to reconstruct the 3D volume density, we show that the SFEs in 12 nearby GMCs are all very similar, and the small dispersion we recover provides strong constraints on theories for how the star formation rate is regulated (Chapter 2). As for the destruction of GMCs, previous extragalactic observations of the Hα-CO decorrelation have led some authors to propose that GMCs disperse rapidly, disappearing within a few Myr after the first appearance of massive stars. Our analysis in Chapter 4, however, shows that there is a significant discrepancy between the Hα emission and star formation on cloud scales due to the fact that ionizing photons travel a finite distance before being absorbed, which in turn leads to an underestimate of the time required for GMC dispersal. We provide a calibration model for Hα traced SFR measurements in massive clouds, where ionizing photons are confined locally. In summary, our work reduces observational biases through different GMC evolution stages, and enhances our understanding of the GMC life cycle.

5.2 Caveats

The theoretical model and simulations used in this thesis are carefully designed for comparisons with observations. However, they can be further improved with the recent progress of numerical methods and observations. Here I will discuss the current caveats of the work in each chapter, and how they can be addressed.

5.2.1 Testing the H21 model

The H21 model applied in Chapter 2 can predict 3D free-fall time-weighted volume densities from 2D column density observations. This model is derived from simulations of a dense molecular clump with a sub-pc spatial scale, while the molecular cloud observations I study in Chapter 2 have a size on the order of 10 pc. Although the ISM density structure appears to be self-similar in a wide range of length scales, it is still important to test whether this model is applicable to general ISM across different scales. Such tests require measurements of 3D gas density distribution, which was not available before the submission of the manuscript in Chapter 2 in 2021. Later that year, Zucker et al. (2021) published 3D dust maps of the nearby molecular clouds (distance $\leq$ 400 pc) with a spatial resolution $\sim$ 1 pc. Such results trace the 3D gas density distribution in nearby GMCs, which provide perfect testing data for the H21 model. After performing the same analysis as described in Section 2.3.1 on the gas density cubes in Zucker et al. (2021), the parameters in equation 2.2 are fitted to be $k_g = 4.4$ and $b = 1.0$, close to the fitting results from simulation analysis ($k_g = 4.6$, $b = 0.93$). These results suggest that the H21 model reveals a general structure of ISM.

However, as mentioned in Zucker et al. (2021), their technique cannot probe high-density regions, meaning that the derived 3D volume densities are likely just lower limits. On the contrary, the H21 model is very sensitive to high density regions since they have much smaller free-fall time values. Moreover, since the dust maps are derived from dust extinctions of background stars, their spatial resolutions are highly dependent on the background star distribution. To improve the credibility of the testing above, we need 3D gas density distribution measurements with less uncertainties and wider dynamic ranges. The recent work by Edenhofer et al. (2024) provides 3D dust maps that can extend out to a distance of 1.25 kpc with parsec-scale spatial resolution. Their extinction uncertainties are also much lower than

Zucker et al. (2021). I plan to test the H21 model again on their data, and further study the 3D gas distribution with a spatial range up to kpc. Note that their analysis may still underestimate the true extinction towards dense dust clouds due to the saturation effect.

5.2.2 Simulation limits

The highest mass resolution of simulations performed in Chapter 3 is ≈ 9 M$_\odot$. Under our star formation criteria, this corresponds to a highest spatial resolution of ≈ 0.4 pc, and a highest number density of $\sim 5 \times 10^5$ cm^{-3}. Therefore, these simulations are only able to resolve the internal B-field structure and mass distribution of a molecular cloud with mass $\gtrsim 1000$ M$_\odot$ and size $\gtrsim 10$ pc. Such range covers the majority of observed GMCs, which confirms the credibility of the conclusions in Chapter 3. However, molecular clouds have long been observed to have filamentary structures (see the review by Chevance et al. 2022). The Snake filament, for example, is a massive molecular filament with a mass of $\sim 1.5 \times 10^4$ M$_\odot$, a length of 22 pc, and a typical width of ~ 1 pc. In this case, the minor axis can only be resolved by one or two gas particles in our simulations; the spherical assumption adopted in the calculation of the energies in Figure 3.8 may also fail. To extend the study in Chapter 3 to long filamentary GMCs, we need to set up simulations with higher resolution. One possible approach is to find filamentary GMC candidates in the existing simulations, extract boxes around them as initial conditions, then re-simulate their formation with spatial resolution no bigger than 0.01 pc.

The effect of resolution is trivial for the study in Chapter 4: the size of H II region we study is on the scale of 100 pc, and the extragalactic observations we compare has beam sizes of at least 20 pc, both much larger than the simulation resolution (≈ 1 pc). Nevertheless, the resolution limit may still indirectly affect the evolution of GMCs in our simulation. As discussed in Section 4.4.1, young stars drifting out of their birth clouds can cause the ionizing photons leak out of the GMCs, which enlarges the corresponding H II regions. This effect depends on the relative positions of the young stars and GMCs, but the stellar drift motion may not be well resolved if the drift direction is along the minor axis of a filamentary cloud, which may only consist of one or two gas particles. To determine the resolution at which this effect converges, we can set up a suite of simulations with different resolutions to trace the evolution of the same individual GMC.

Another drawback of our theoretical modeling in the last two chapters is the simplification of physical mechanisms. The most relevant ones for Chapter 3 are the non-ideal MHD effects, including ambipolar diffusion, Hall effect, and Ohmic dissipation. Such effects normally happen in the dense molecular gas with $n_{\rm H} > 10^4$ cm^{-3} and are found to affect the evolution of sub-parsec structures inside GMCs (e.g. Ntormousi et al. 2016). These effects are not included in our simulation, but their roles should not be significant in our study of magnetic criticality transition in Chapter 3: such transition, if it exists, would happen before GMC formation, when the gas density is not high enough for non-ideal MHD effects to be important. As for the study in Chapter 4, one potential error arises from our calculation of ionizing luminosity from stars. As described in Section 4.2.1, In the simulations we derive the ionizing luminosity with classic stellar tracks and stellar atmosphere models over two decades ago, while recent work introduce additional complexity to this problem. For example, Sana et al. (2012) find that a significant fraction of massive stars are in binary systems, which can cause mass transfer and stripping of the stellar envelopes. This process can result in higher stellar surface temperature with harder ionizing spectra (Götberg et al. 2017), leading to higher ionizing flux which can extend the reach of photoionization in the ISM. Therefore, the simulations in this thesis would be more accurate by adopting recent spectral models with higher complexity (e.g. Götberg et al. 2018), which will potentially lead to greater cloud-scale mismatch between $\Sigma_{\rm SFR,H\alpha}$ and $\Sigma_{\rm SFR,YSO}$.

Due to limited computational resources, there are a number of other physical mechanisms that have been missed in my numerical modeling. Here is a brief discussion of their potential effects. (1) When modeling the photoionization effect, I directly set the nearby gas to be fully ionized instead of tracing propagation of the ionizing radiation, like in the work by Grudić et al. (2019). This simplification may affect the morphology of the H II regions, especially in diffuse ISM. (2) The radiation pressure of direct/IR/Lyα radiation is not considered in the simulations. As discussed in the review by Chevance et al. (2022), the momentum input by these radiations in total is about 10% of that by photoionization, thus including them would just slightly shorten the cloud dispersal time estimated in Chapter 4. (3) I assume a constant ISRF when running the simulations, while in reality the dense region inside GMCs will be shielded from the external radiation and cosmic rays. As a result, the chemical and thermal states of the molecular gas is not accurately calculated. (4) I did not consider non-equilibrium metal line cooling, which can be important especially in dynamically evolving environments like the shock-heated regions. It can affect the temperature structure of the GMC, and potentially impact its fragmentation process and subsequent star formation rate (Richings et al. 2014a,b).

5.3 Future work

From the work in this thesis, we have developed unique techniques that can help us to dive into specific aspects of GMCs and related structures. Here we propose three future projects to study a particular molecular structure in the Galaxy, and how different mechanisms like radiation, magnetic field, and turbulence interplay with each other in the GMC to determine its behavior.

5.3.1 The evolution of GMFs

Giant molecular filaments (GMFs) are massive, thin, near-linear structures of molecular gas that stretch along the Galactic plane (see Figure 5.1). In the last decade, more than 20 GMFs have been found with different tracers (e.g. Wang et al. 2015; Zucker et al. 2018; Ge & Wang 2022). Zucker et al. (2018) find that these large-scale filaments have a wide range of physical properties, implying different formation and evolution tracks. Some authors have argued that GMFs trace the spiral arms of the Galaxy, but this proposition is intensely disputed. Meanwhile, correlations between GMFs and star formation suggest that massive star formation begins immediately as a GMF forms, such that essentially all GMFs have embedded massive star formation. The same is not true of GMCs.

This project will focus on understanding the GMF life cycle and the relationship between GMFs and Galactic spiral structures. Previous simulation work (Duarte-Cabral & Dobbs 2017) argues that GMFs are transient structures and actually not coherent with spiral arms. Their simulations, however, suffer from several limitations that our simulations in this thesis can overcome:

- Our MHD simulations provide a Galactic scale magnetic field, which may be important to the production and maintenance of filamentary structures.
- Our simulations use a realistic, stochastic prescription for star-by-star feedback that is suitable for high-resolution Galactic simulations.
- Grand design spirals such as the Milky Way mostly do not occur in isolation, but are instead driven by external interactions – in the Milky Way's case dominated by the Magellanic Clouds – which we plan to include in the future work.

This project aims to answer the following questions: what is the typical lifetime of a GMF, and how does the Galactic environment control its evolution? What is the relationship between GMFs and spiral arms? Why are the GMFs forming stars so rapidly? Does this phenomenon challenge existing star formation theories?

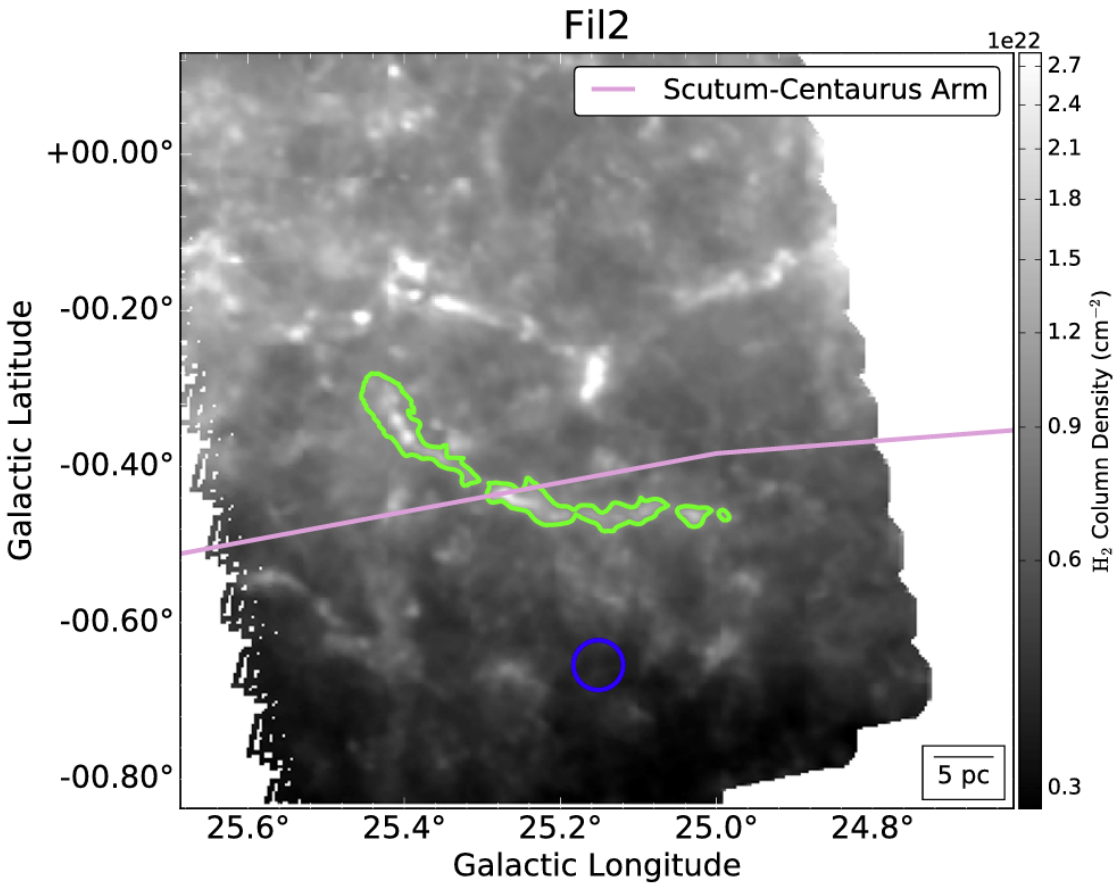

Figure 5.1: The *Herschel* column density map for a single GMF close to the Scutum-Centaurus Arm. Image Credit: Zucker et al. (2018).

Are the evolution tracks of GMFs correlated with their physical properties? The proposed methodology includes tracing GMF evolution and properties with time, and producing synthetic observations with different tracers for comparison with observations from facilities like FAST and ALMA.

5.3.2 Sub-critical DCF measurements: Are they also illusions?

Although Chapter 3 has shed doubt on the sub-critical B-field measurements from Zeeman effect observations in H I , recent magnetic field measurements (using the DCF method) of the Snake filament, a massive star-forming molecular filament, still suggest a cloud-scale magnetic field that dominates over gravity (Ngoc et al. 2023). The DCF method deduces the field strength from the degree of dispersion in dust polarization under the assumption that non-spherical dust grains suspended in the gas become preferentially aligned relative to the magnetic field due to torques exerted by starlight. At sufficiently high optical depths, however, such alignment is expected to be less efficient due to weak radiation fields, resulting in declining polarization fraction (e.g. Pattle et al. 2019). Since the polarization fraction is higher in the surface region of the GMC, the magnetic field revealed from polarization data is very likely to be biased towards this region, making the sub-critical measurements unrepresentative of the whole cloud. The plan for testing this hypothesis is to find clouds with different masses and distances to nearest stars (and thus different radiation fields) from the simulations described in Chapter 3, then produce synthetic polarization maps using both the radiative transfer code POLARIS and the grain alignment theory proposed by King et al. (2019). To make this study more comprehensive, we also need to compare between the synthetic observations with ongoing HINSA Zeeman effect measurements by FAST. The results will show if DCF measurements suffer from the same biases as Zeeman ones, and thus overestimate the dynamical importance of magnetic fields.

5.3.3 Effects of photonionized gas pressure on GMCs

Ionizing radiation from young massive stars plays a key role in the GMC life cycle because it can photoevaporate and eject the surrounding gas, and finally disperse the parent cloud. Previous simulations of isolated molecular clouds find that this radiation feedback can disperse molecular clouds with masses from 10^4 to 10^6 $M_\odot$ (Kim et al. 2018). These simulations, however, begin from isolated spherical clouds without a realistic galactic environment around them. In realistic turbulent clouds with non-uniform gas pressure from the environment, such dispersal may be less efficient. The reason is that the momentum injection will favor the direction with less gas pressure, propelling the molecular cloud like a rocket rather than spherically destroying it. The zoom-in simulations of GMCs in a galactic environment in Chapter 3 offer a perfect opportunity to explore this possibility. This project will trace the photonionization feedback within selected GMCs, study the relation between the injected radiation momentum and cloud life time, and analyze how this feedback regulates star formation on both cloud and galactic scale.

Bibliography

Ade P. A. R., et al., 2016, A&A, 586, A138

Andersson E. P., Renaud F., Agertz O., 2021, MNRAS, 502, L29

André P., et al., 2010, A&A, 518, L102

André P., Di Francesco J., Ward-Thompson D., Inutsuka S.-I., Pudritz R. E., Pineda J., 2014, Protostars and Planets VI

Armillotta L., Krumholz M. R., Di Teodoro E. M., McClure-Griffiths N. M., 2019, MNRAS, 490, 4401

Armillotta L., Krumholz M. R., Di Teodoro E. M., 2020, MNRAS, 493, 5273

Arora R., Krumholz M. R., Federrath C., 2021, MNRAS, 508, 3290

Arzoumanian D., et al., 2011, A&A, 529, L6

Barrera-Ballesteros J. K., et al., 2020, MNRAS, 492, 2651

Belfiore F., et al., 2018, MNRAS, 477, 3014

Belfiore F., et al., 2022, A&A, 659, A26

Bending T. J. R., Dobbs C. L., Bate M. R., 2020, MNRAS, 495, 1672

Bertram E., Federrath C., Banerjee R., Klessen R. S., 2012, MNRAS, 420, 3163

Bolatto A. D., Wolfire M., Leroy A. K., 2013, ARA&A, 51, 207–268

Bourke T. L., Myers P. C., Robinson G., Hyland A. R., 2001, ApJ, 554, 916

Bressan A., Marigo P., Girardi L., Salasnich B., Dal Cero C., Rubele S., Nanni A., 2012, MNRAS, 427, 127

Burkhart B., 2018, ApJ, 863, 118

Calzetti D., et al., 2023, ApJ, 946, 1

Caplar N., Tacchella S., 2019, MNRAS, 487, 3845–3869

Carney M. T., Yıldız U. A., Mottram J. C., van Dishoeck E. F., Ramchandani J., Jørgensen J. K., 2016, A&A, 586, A44

Chabrier G., 2003, PASP, 115, 763

Chabrier G., 2005, in Corbelli E., Palla F., Zinnecker H., eds, Astrophysics and Space Science Library Vol. 327, The Initial Mass Function 50 Years Later. p. 41, doi:10.1007/978-1-4020-3407-7_5

Chandrasekhar S., Fermi E., 1953, ApJ, 118, 113

Chen C. H. R., Chu Y.-H., Gruendl R. A., Gordon K. D., Heitsch F., 2009, ApJ, 695, 511

Chen C. H. R., et al., 2010, ApJ, 721, 1206

Chevance M., et al., 2020, MNRAS, 493, 2872

Chevance M., et al., 2021, MNRAS, 509, 272–288

Chevance M., et al., 2022, MNRAS, 509, 272

Chevance M., Krumholz M. R., McLeod A. F., Ostriker E. C., Rosolowsky E. W., Sternberg A., 2023, in Protostars and Planets VII. p. 1 (`arXiv:2203.09570`), doi:10.48550/arXiv.2203.09570

Ching T. C., Li D., Heiles C., Li Z. Y., Qian L., Yue Y. L., Tang J., Jiao S. H., 2022, Nature, 601, 49

Crocker R. M., Krumholz M. R., Thompson T. A., Clutterbuck J., 2018, MNRAS, 478, 81

Crutcher R. M., 2012, ARA&A, 50, 29

Crutcher R. M., Troland T. H., Goodman A. A., Heiles C., Kazes I., Myers P. C., 1993, ApJ, 407, 175

Crutcher R. M., Troland T. H., Lazareff B., Paubert G., Kazès I., 1999, ApJ, 514, L121

Cunningham A. J., Krumholz M. R., McKee C. F., Klein R. I., 2018, MNRAS, 476, 771–792

Dame T. M., et al., 1987, ApJ, 322, 706

Dame T. M., Hartmann D., Thaddeus P., 2001, ApJ, 547, 792

Davis Leverett J., Greenstein J. L., 1951, ApJ, 114, 206

Dobashi K., Uehara H., Kandori R., Sakurai T., Kaiden M., Umemoto T., Sato F., 2005, Publications of the Astronomical Society of Japan, 57, S1

Dobbs C. L., et al., 2014, in Beuther H., Klessen R. S., Dullemond C. P., Henning T., eds, Protostars and Planets VI. pp 3–26 (`arXiv:1312.3223`), doi:10.2458/azu˙uapress˙9780816531240-ch001

Draine B. T., 1978, ApJS, 36, 595

Draine B. T., 2011, Physics of the Interstellar and Intergalactic Medium. Princeton University Press

Duarte-Cabral A., Dobbs C. L., 2017, MNRAS, 470, 4261

Dunham M. M., et al., 2014, Protostars and Planets VI

Dunham M. M., et al., 2015, ApJS, 220, 11

Edenhofer G., Zucker C., Frank P., Saydjari A. K., Speagle J. S., Finkbeiner D., Enßlin T. A., 2024, A&A, 685, A82

Ellison S. L., Sánchez S. F., Ibarra-Medel H., Antonio B., Mendel J. T., Barrera-Ballesteros J., 2017, MNRAS, 474, 2039–2054

Elmegreen B. G., Parravano A., 1994, ApJ, 435, L121

Elmegreen B. G., Scalo J., 2004, ARA&A, 42, 211

Evans N. J., et al., 2009, ApJS, 181, 321–350

Evans N. J., Heiderman A., Vutisalchavakul N., 2014, ApJ, 782, 114

Faesi C. M., Lada C. J., Forbrich J., 2018, ApJ, 857, 19

Falgarone E., Troland T. H., Crutcher R. M., Paubert G., 2008, A&A, 487, 247

Fall S. M., Krumholz M. R., Matzner C. D., 2010, ApJ, 710, L142

Faucher-Giguère C.-A., Quataert E., Hopkins P. F., 2013, MNRAS, 433, 1970–1990

Federrath C., 2013, MNRAS, 436, 3167–3172

Federrath C., Banerjee S., 2015, MNRAS, 448, 3297–3313

Federrath C., Klessen R. S., 2012, ApJ, 761, 156

Ferland G. J., Korista K. T., Verner D. A., Ferguson J. W., Kingdon J. B., Verner E. M., 1998, PASP, 110, 761

Field G. B., Goldsmith D. W., Habing H. J., 1969, ApJ, 155, L149

Flores Velázquez J. A., et al., 2020, MNRAS, 501, 4812–4824

Froebrich D., Rowles J., 2010, MNRAS, 406, 1350

Fujimoto Y., Krumholz M. R., Tachibana S., 2018, MNRAS, 480, 4025

Fujimoto Y., Chevance M., Haydon D. T., Krumholz M. R., Kruijssen J. M. D., 2019, MNRAS, 487, 1717

Fukushima H., Yajima H., Sugimura K., Hosokawa T., Omukai K., Matsumoto T., 2020, MNRAS, 497, 3830

Ge Y., Wang K., 2022, ApJS, 259, 36

Girardi L., Bressan A., Bertelli G., Chiosi C., 2000, A&AS, 141, 371

Girichidis P., Seifried D., Naab T., Peters T., Walch S., Wünsch R., Glover S. C. O., Klessen R. S., 2018, MNRAS, 480, 3511

Glover S. C. O., Federrath C., Mac Low M., Klessen R. S., 2010, MNRAS, 404, 2

Gong M., Ostriker E. C., Wolfire M. G., 2017, ApJ, 843, 38

Goodman A. A., Pineda J. E., Schnee S. L., 2009, ApJ, 692, 91–103

Götberg Y., de Mink S. E., Groh J. H., 2017, A&A, 608, A11

Götberg Y., de Mink S. E., Groh J. H., Kupfer T., Crowther P. A., Zapartas E., Renzo M., 2018, A&A, 615, A78

Gregg B., et al., 2024, ApJ, 971, 115

Grisdale K., Agertz O., Renaud F., Romeo A. B., Devriendt J., Slyz A., 2019, MNRAS, 486, 5482

Grudić M. Y., Hopkins P. F., Lee E. J., Murray N., Faucher-Giguère C.-A., Johnson L. C., 2019, MNRAS, 488, 1501

Grudić M. Y., Guszejnov D., Hopkins P. F., Offner S. S. R., Faucher-Giguère C.-A., 2021, MNRAS, 506, 2199

Gutermuth R. A., et al., 2008, ApJ, 674, 336

Gutermuth R. A., Megeath S. T., Myers P. C., Allen L. E., Pipher J. L., Fazio G. G., 2009, ApJS, 184, 18–83

Haydon D. T., Kruijssen J. M. D., Chevance M., Hygate A. P. S., Krumholz M. R., Schruba A., Longmore S. N., 2020, MNRAS, 498, 235

Heiles C., Troland T. H., 2004, ApJS, 151, 271

Hennebelle P., Chabrier G., 2011, ApJ, 743, L29

Hennebelle P., Grudić M. Y., 2024, arXiv e-prints, p. arXiv:2404.07301

Heyer M., Krawczyk C., Duval J., Jackson J. M., 2009, ApJ, 699, 1092

Heyer M., Gutermuth R., Urquhart J. S., Csengeri T., Wienen M., Leurini S., Menten K., Wyrowski F., 2016, A&A, 588, A29

Hopkins P. F., 2015, MNRAS, 450, 53–110

Hopkins P. F., 2016, MNRAS, 462, 576

Hopkins P. F., Raives M. J., 2016, MNRAS, 455, 51

Hopkins P. F., et al., 2018a, MNRAS, 477, 1578

Hopkins P. F., et al., 2018b, MNRAS, 480, 800

Hu Z., Krumholz M. R., Federrath C., Pokhrel R., Gutermuth R. A., 2021a, MNRAS, 502, 5997–6009

Hu C.-Y., Sternberg A., van Dishoeck E. F., 2021b, ApJ, 920, 44

Hu Z., Krumholz M. R., Pokhrel R., Gutermuth R. A., 2022, MNRAS

Hu Z., Wibking B. D., Krumholz M. R., 2023, MNRAS, 521, 5604–5615

Hull C. L. H., et al., 2017, ApJ, 842, L9

Hygate A. P. S., Kruijssen J. M. D., Chevance M., Schruba A., Haydon D. T., Longmore S. N., 2019, MNRAS, 488, 2800

Ibáñez-Mejía J. C., Mac Low M.-M., Klessen R. S., 2021, arXiv e-prints, p. arXiv:2108.04967

Indebetouw R., et al., 2008, AJ, 136, 1442

Jeans J. H., 1902, Philosophical Transactions of the Royal Society of London Series A, 199, 1

Jeffreson S. M. R., Keller B. W., Winter A. J., Chevance M., Kruijssen J. M. D., Krumholz M. R., Fujimoto Y., 2021a, MNRAS, 505, 1678

Jeffreson S. M. R., Krumholz M. R., Fujimoto Y., Armillotta L., Keller B. W., Chevance M., Kruijssen J. M. D., 2021b, MNRAS, 505, 3470

Jeffreson S. M. R., Semenov V. A., Krumholz M. R., 2024, MNRAS, 527, 7093

Jin Y., Kewley L. J., Sutherland R. S., 2022, ApJ, 934, L8

Jog C. J., Solomon P. M., 1984, ApJ, 276, 114

Kado-Fong E., Kim J.-G., Ostriker E. C., Kim C.-G., 2020, ApJ, 897, 143

Kainulainen J., Beuther H., Henning T., Plume R., 2009, A&A, 508, L35–L38

Kainulainen J., Hacar A., Alves J., Beuther H., Bouy H., Tafalla M., 2016, A&A, 586, A27

Kalberla P. M. W., Kerp J., 2009, ARA&A, 47, 27

Kennicutt R. C. J., 1983, ApJ, 272, 54

Kennicutt R. C., Evans N. J., 2012, ARA&A, 50, 531–608

Kim C.-G., Kim W.-T., Ostriker E. C., 2011, ApJ, 743, 25

Kim J.-G., Kim W.-T., Ostriker E. C., 2018, ApJ, 859, 68

Kim J.-G., Ostriker E. C., Filippova N., 2021, ApJ, 911, 128

Kim J., et al., 2022, MNRAS, 516, 3006

King P. K., Chen C.-Y., Fissel L. M., Li Z.-Y., 2019, MNRAS, 490, 2760

Kirkpatrick J. D., et al., 2024, ApJS, 271, 55

Klessen R. S., Glover S. C. O., 2014, Physical Processes in the Interstellar Medium (`arXiv:1412.5182`)

Klessen R. S., Glover S. C. O., 2016, Saas-Fee Advanced Course, 43, 85

Kruijssen J. M. D., Longmore S. N., 2014, MNRAS, 439, 3239

Kruijssen J. M. D., Schruba A., Hygate A. P. S., Hu C.-Y., Haydon D. T., Longmore S. N., 2018, MNRAS, 479, 1866

Kruijssen J. M. D., et al., 2019, Nature, 569, 519–522

Krumholz M. R., 2014a, MNRAS, 437, 1662

Krumholz M. R., 2014b, Physics Reports, 539, 49–134

Krumholz M. R., McKee C. F., 2005, ApJ, 630, 250–268

Krumholz M. R., McKee C. F., 2020, MNRAS, 494, 624–641

Krumholz M. R., Tan J. C., 2007, ApJ, 654, 304–315

Krumholz M. R., Leroy A. K., McKee C. F., 2011, ApJ, 731, 25

Krumholz M. R., Dekel A., McKee C. F., 2012, ApJ, 745, 69

Krumholz M. R., Fumagalli M., da Silva R. L., Rendahl T., Parra J., 2015, MNRAS, 452, 1447

Krumholz M. R., McKee C. F., Bland-Hawthorn J., 2019, ARA&A, 57, 227

Kryukova E., Megeath S. T., Gutermuth R. A., Pipher J., Allen T. S., Allen L. E., Myers P. C., Muzerolle J., 2012, AJ, 144, 31

Kryukova E., et al., 2014, AJ, 148, 11

Kudritzki R.-P., Puls J., 2000, ARA&A, 38, 613

Kulsrud R. M., Zweibel E. G., 2008, Reports on Progress in Physics, 71, 046901

Lada C. J., Lombardi M., Roman-Zuniga C., Forbrich J., Alves J. F., 2013, ApJ, 778, 133

Lancaster L., Ostriker E. C., Kim J.-G., Kim C.-G., 2021, ApJ, 914, 89

Larson R. B., 1981, MNRAS, 194, 809

Lawrence A., et al., 2007, MNRAS, 379, 1599–1617

Lazarian A., 2007, J. Quant. Spec. Radiat. Transf., 106, 225

Lee E. J., Miville-Deschênes M.-A., Murray N. W., 2016, ApJ, 833, 229

Leitherer C., et al., 1999, ApJS, 123, 3

Li Z.-Y., Nakamura F., 2006, ApJ, 640, L187

Li H. B., Goodman A., Sridharan T. K., Houde M., Li Z. Y., Novak G., Tang K. S., 2014, in Beuther H., Klessen R. S., Dullemond C. P., Henning T., eds, Protostars and Planets VI. p. 101, doi:10.2458/azu_uapress_9780816531240-ch005

Liu J., Zhang Q., Qiu K., 2022, Frontiers in Astronomy and Space Sciences, 9, 943556

Lombardi M., Alves J., Lada C. J., 2010, A&A, 519, L7

Lombardi M., Bouy H., Alves J., Lada C. J., 2014, A&A, 566, A45

Lopez L. A., Krumholz M. R., Bolatto A. D., Prochaska J. X., Ramirez-Ruiz E., 2011, ApJ, 731, 91

Lopez L. A., Krumholz M. R., Bolatto A. D., Prochaska J. X., Ramirez-Ruiz E., Castro D., 2014, ApJ, 795, 121

Lucas P. W., et al., 2008, MNRAS, 391, 136–163

Mathis J. S., 1986, ApJ, 301, 423

Matzner C. D., Jumper P. H., 2015, ApJ, 815, 68

McClymont W., et al., 2024, MNRAS, 532, 2016

McKee C. F., Ostriker J. P., 1977, ApJ, 218, 148

McKellar A., 1940, PASP, 52, 187

Menon S. H., Federrath C., Krumholz M. R., Kuiper R., Wibking B. D., Jung M., 2022a, MNRAS, 512, 401

Menon S. H., Federrath C., Krumholz M. R., 2022b, MNRAS, 517, 1313

Meynet G., Maeder A., Schaller G., Schaerer D., Charbonnel C., 1994, A&AS, 103, 97

Mouschovias T. C., Spitzer L. J., 1976, ApJ, 210, 326

Murray N., Chang P., 2015, ApJ, 804, 44

Ngoc N. B., et al., 2023, ApJ, 953, 66

Nieva M.-F., Przybilla N., 2012, A&A, 539, A143

Ntormousi E., Hennebelle P., André P., Masson J., 2016, A&A, 589, A24

Ochsendorf B. B., Meixner M., Roman-Duval J., Rahman M., Evans N. J., 2017, ApJ, 841, 109

Ostriker E. C., Shetty R., 2011, ApJ, 731, 41

Padoan P., Haugbølle T., Nordlund Å., 2012, ApJ, 759, L27

Pattle K., et al., 2019, ApJ, 880, 27

Pattle K., Fissel L., Tahani M., Liu T., Ntormousi E., 2023, in Inutsuka S., Aikawa Y., Muto T., Tomida K., Tamura M., eds, Astronomical Society of the Pacific Conference Series Vol. 534, Protostars and Planets VII. p. 193 (`arXiv:2203.11179`), doi:10.48550/arXiv.2203.11179

Peltonen J., et al., 2024, MNRAS, 527, 10668

Peters T., et al., 2017, MNRAS, 466, 3293

Pflamm-Altenburg J., Kroupa P., 2008, Nature, 455, 641

Pokhrel R., et al., 2016, MNRAS, 461, 22

Pokhrel R., et al., 2020, ApJ, 896, 60

Pokhrel R., et al., 2021, ApJ, 912, L19

Priestley F. D., Yin C., Wurster J., 2022, MNRAS, 515, 5689

Ramambason L., et al., 2022, A&A, 667, A35

Richings A. J., Schaye J., Oppenheimer B. D., 2014a, MNRAS, 440, 3349

Richings A. J., Schaye J., Oppenheimer B. D., 2014b, MNRAS, 442, 2780

Safranek-Shrader C., Krumholz M. R., Kim C.-G., Ostriker E. C., Klein R. I., Li S., McKee C. F., Stone J. M., 2017, MNRAS, 465, 885

Saintonge A., Catinella B., 2022, ARA&A, 60, 319

Salim D. M., Federrath C., Kewley L. J., 2015, ApJ, 806, L36

Salpeter E. E., 1955, ApJ, 121, 161

Sana H., et al., 2012, Science, 337, 444

Sánchez S. F., et al., 2012, A&A, 538, A8

Schaller G., Schaerer D., Meynet G., Maeder A., 1992, A&AS, 96, 269

Schneider S., Elmegreen B. G., 1979, ApJS, 41, 87

Schneider N., et al., 2011, A&A, 529, A1

Schneider N., et al., 2015, A&A, 575, A79

Scoville N. Z., Yun M. S., Clemens D. P., Sanders D. B., Waller W. H., 1987, ApJS, 63, 821

Sembach K. R., Howk J. C., Ryans R. S. I., Keenan F. P., 2000, ApJ, 528, 310–324

Semenov V. A., Kravtsov A. V., Gnedin N. Y., 2021, ApJ, 918, 13

Shivaei I., Reddy N. A., Steidel C. C., Shapley A. E., 2015, ApJ, 804, 149

Shu F. H., 1977, ApJ, 214, 488

Shu F. H., Adams F. C., Lizano S., 1987, ARA&A, 25, 23

Skrutskie M. F., et al., 2006, AJ, 131, 1163

Smith B., Sigurdsson S., Abel T., 2008, MNRAS, 385, 1443

Smith B. D., et al., 2017, MNRAS, 466, 2217

Soler J. D., Hennebelle P., Martin P. G., Miville-Deschênes M.-A., Netterfield C. B., Fissel L. M., 2013, ApJ, 774, 128

Solomon P., Vanden Bout P., 2005, ARA&A, 43, 677–725

Solomon P. M., Rivolo A. R., Barrett J., Yahil A., 1987, ApJ, 319, 730

Sternberg A., Dalgarno A., 1995, ApJS, 99, 565

Sukhbold T., Ertl T., Woosley S. E., Brown J. M., Janka H. T., 2016, ApJ, 821, 38

Swings P., Rosenfeld L., 1937, ApJ, 86, 483

Tacchella S., et al., 2022, MNRAS, 513, 2904–2929

Tacconi L. J., Genzel R., Sternberg A., 2020, ARA&A, 58, 157

Teyssier R., Commerçon B., 2019, Frontiers in Astronomy and Space Sciences, 6, 51

Thompson T. A., Fabian A. C., Quataert E., Murray N., 2015, MNRAS, 449, 147

Thompson K. L., Troland T. H., Heiles C., 2019, ApJ, 884, 49

Toomre A., 1964, ApJ, 139, 1217

Tritsis A., Federrath C., Willacy K., Tassis K., 2022, MNRAS, 510, 4420

Troland T. H., Crutcher R. M., 2008, ApJ, 680, 457

Troland T. H., Goss W. M., Brogan C. L., Crutcher R. M., Roberts D. A., 2016, ApJ, 825, 2

Utomo D., et al., 2018, ApJ, 861, L18

Vink J. S., de Koter A., Lamers H. J. G. L. M., 2001, A&A, 369, 574

Vishniac E. T., Lazarian A., 1999, ApJ, 511, 193

Wang K., Testi L., Ginsburg A., Walmsley C. M., Molinari S., Schisano E., 2015, MNRAS, 450, 4043

Ward-Thompson D., et al., 2017, ApJ, 842, 66

Weisz D. R., et al., 2012, ApJ, 744, 44

Wibking B. D., Krumholz M. R., 2023, MNRAS, 521, 5972

Wibking B. D., Thompson T. A., Krumholz M. R., 2018, MNRAS, 477, 4665

Wilson R. W., Jefferts K. B., Penzias A. A., 1970, ApJ, 161, L43

Wilson B. A., Dame T. M., Masheder M. R. W., Thaddeus P., 2005, A&A, 430, 523

Wood K., Hill A. S., Joung M. R., Mac Low M.-M., Benjamin R. A., Haffner L. M., Reynolds R. J., Madsen G. J., 2010, ApJ, 721, 1397–1403

Zavagno A., et al., 2020, A&A, 638, A7

Zucker C., Battersby C., Goodman A., 2018, ApJ, 864, 153

Zucker C., et al., 2021, ApJ, 919, 35

Zuckerman B., Evans N. J., 1974, ApJ, 192, L149

da Silva R. L., Fumagalli M., Krumholz M., 2012, ApJ, 745, 145

da Silva R. L., Fumagalli M., Krumholz M. R., 2014, MNRAS, 444, 3275